

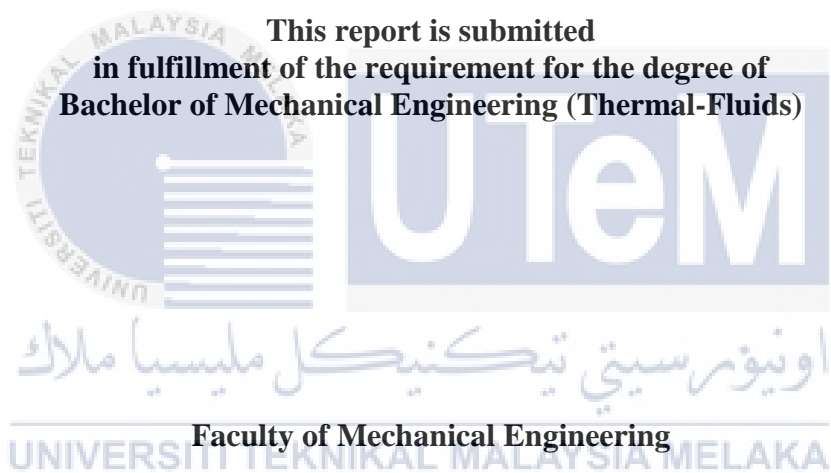
PERFORMANCE IMPROVEMENT OF SPLIT SAVONIUS ROTOR BY CFD



UNIVERSITI TEKNIKAL MALAYSIA MELAKA

**PERFORMANCE IMPROVEMENT OF SPLIT SAVONIUS ROTOR
BY CFD**

NUR HAYATI BINTI HASSAN



UNIVERSITI TEKNIKAL MALAYSIA MELAKA

MAY 2017

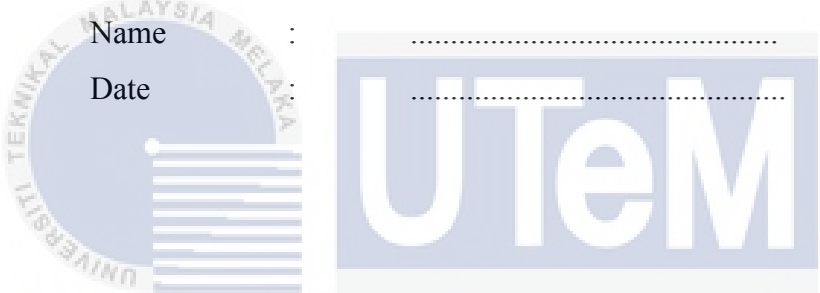
DECLARATION

I declare that this project report entitled Performance Improvement of Split Savonius Rotor by CFD is the result of my own work except as cited in references.

Signature :

Name :

Date :



UNIVERSITI TEKNIKAL MALAYSIA MELAKA

اونيورسيتي تيكنيكل مليسيا ملاك

UNIVERSITI TEKNIKAL MALAYSIA MELAKA

APPROVAL

I hereby declare that I have read this project report and in my opinion this report is sufficient in terms of scope and quality for the award of Bachelor of Mechanical Engineering (Thermal-Fluids)

Signature :

Name of Supervisor :

Date :



DEDICATION

To my beloved husband, Mohd Anis bin Abd Rahman.



ABSTRACT

Split Savonius wind turbine is a type of vertical axis wind turbine. Conventional Split Savonius wind turbine consists of two blades, advancing and returning. Advancing blade produces drag force from main flow while returning blade develops return force from opposite direction through a gap called overlap. Two types of torque are generated due to rotational motion of these blades against working fluid, positive and negative torque. Main objective of present study is to conduct a two dimensional numerical analysis between conventional Split Savonius rotor and new configurations in term of net positive torque and coefficient of performance (COP). Three new configurations are designed based on conventional Split Savonius rotor by keeping end plate diameter, overlap and aspect ratio constant. A validation study is performed by comparing torque obtained by numerical approach with torque obtained by experimental approach. Validated methodology is adopted to simulate new configurations. An improvement in COP ranging from 0.78% to 1.33% for different inlet velocities is achieved for new configuration Design 1. Other designs show negative improvement.

UNIVERSITI TEKNIKAL MALAYSIA MELAKA

ABSTRAK

Turbin angin Split Savonius adalah sejenis turbin angin vertikal. Turbin angin Split Savonius yang asas terdiri daripada dua jenis bilah iaitu bilah mara dan bilah kembali. Bilah mara menghasilkan daya seret dari aliran utama manakala bilah kembali menghasilkan daya kembali dari arah bertentangan melalui jurang yang dikenali sebagai pertindihan. Dua jenis daya kilas dijana daripada pergerakan putaran antara bilah-bilah ini dan bendalir yang digunakan iaitu daya kilas positif dan negatif. Objektif utama kajian ini adalah untuk mengendalikan analisa numerik dua dimensi antara pemutar asas Split Savonius dan konfigurasi baru dari segi daya kilas positif bersih dan pekali prestasi. Tiga jenis konfigurasi baru direka berdasarkan pemutar asas Split Savonius dengan mengekalkan diameter plat, pertindihan dan nisbah aspek malar. Kajian pensahihan dilaksanakan dengan membandingkan nilai daya kilas yang diperolehi daripada kaedah numerik dengan nilai daya kilas yang diperolehi daripada kaedah eksperimentasi. Metodologi yang sah tersebut digunakan bagi mensimulasi konfigurasi baru. Peningkatan pekali prestasi antara nilai 0.78% sehingga 1.33% telah dicapai bagi halaju masuk yang berbeza-beza untuk konfigurasi 1. Konfigurasi-konfigurasi lain tidak menunjukkan sebarang peningkatan.

ACKNOWLEDGEMENT

Alhamdulillah. I would like to express my greatest appreciation towards my supervisor, Dr. Cheng See Yuan who I would not be able to complete this study without. Thank you for accepting me as your PSM's student and giving me the opportunity to learn so much from you. Thank you for constantly advising and guiding me throughout this study with patience.

I would like to thank other FKM lecturers for sharing their knowledge in respective area of study. I would also like to thank UTeM's CAE assistant engineer, Mr. Rizal for allowing me to use the facility and ensuring it is in the best condition.

I would like to thank my course mates for their contribution in this study. Last but not least I would like to express my gratitude towards my family for their endless support and encouragement.

اوتيم سیتی تکنیکل ملیسیا ملاک
UNIVERSITI TEKNIKAL MALAYSIA MELAKA

CONTENT

CHAPTER	CONTENT	PAGE
	DECLARATION	ii
	APPROVAL	iii
	DEDICATION	iv
	ABSTRACT	v
	ABSTRAK	vi
	ACKNOWLEDGEMENT	vii
	LIST OF FIGURES.....	x
	LIST OF TABLES.....	xiii
	LIST OF ABBREVIATIONS.....	xiv
	LIST OF SYMBOLS.....	xv
	INTRODUCTION	1
	1.1 BACKGROUND	1
	1.2 PROBLEM STATEMENT.....	3
	1.3 OBJECTIVE	4
	1.4 SCOPE OF PROJECT	4
	LITERATURE REVIEW	5
	2.1 ENERGY IN THE WIND	5
	2.2 WIND TURBINE	6
	2.3 OPTIMIZATION OF SAVONIUS WIND TURBINE	7
	2.3.1 BLADE DESIGN	7
	2.3.2 NUMBER OF BLADES.....	10
	2.3.3 END PLATE DESIGN	11
	2.3.4 NUMBER OF STAGES	12
	2.3.5 OVERLAP RATIO.....	12
	2.3.6 ASPECT RATIO	13
	2.4 COMPUTATIONAL FLUID DYNAMICS.....	13

METHODOLOGY	15
3.1 INTRODUCTION	15
3.2 GEOMETRY	17
3.3 MATHEMATICAL MODELLING	21
3.3.1 GOVERNING EQUATION	22
3.3.2 TURBULENCE MODELLING	23
3.3.3 MESHING	25
3.3.4 SETUP AND SOLUTION	33
3.3.5 SOLUTION CONVERGENCE	34
RESULTS AND DISCUSSION	49
4.1 VALIDATION STUDY	49
4.2 COMPARATIVE STUDY	50
SUMMARY	75
REFERENCES	76



LIST OF FIGURES

Figure 1.1 Darrieus Wind Turbine. (Source: McAdam, 2016)	2
Figure 1.2 Conventional Savonius Wind Turbine. (Source: REUK.co.uk, Wenlong Tian, 2015)	2
Figure 1.3 Split Savonius Wind Turbine. (Source: Frederikus Wenehenubuna, Andy Saputraa, Hadi Sutanto, 2014)	3
Figure 2.1 Streamlines, primary and opposing torques. (Source: John Patrick Abraham, 2012)	7
Figure 2.2 40 Degree Twisted Blade. (Source: Abdul Qadir Versiani, 2015)	9
Figure 2.3 3D view of helical Savonius turbine. (Source: A. Reza Hassanzadeh, 2013)	9
Figure 2.4 Rotor configurations. (Source: J., 2007)	10
Figure 2.5 Applied boundary conditions. (Source: Sukanta Roy, 2013)	14
Figure 3.1 Methodology flow chart	16
Figure 3.2 Schematic of two-bladed conventional Split Savonius rotor. (Source: U.K Saha, 2008)	17
Figure 3.3 CAD drawing of computational domain for Conventional Split Savonius wind turbine	18
Figure 3.4 Schematic of Design 1	19
Figure 3.5 Schematic of Design 2	20
Figure 3.6 Schematic of Design 3	21
Figure 3.7 Triangular Meshing for Conventional Savonius	25
Figure 3.8 Transition between Stationary and Rotating Domains for Conventional Rotor	26
Figure 3.9 Prism Mesh Layers around Blade in Rotating Domain for Conventional Rotor	26
Figure 3.10 Triangular Meshing for Design 1	27
Figure 3.11 Transition between Stationary and Rotating Domains for Design 1	27
Figure 3.12 Prism Mesh Layers around Blade in Rotating Domain for Design 1	28

Figure 3.13 Triangular Meshing for Design 2	28
Figure 3.14 Transition between Stationary and Rotating Domains for Design 2	29
Figure 3.15 Prism Mesh Layers around Blade in Rotating Domain for Design 2	29
Figure 3.16 Triangular Meshing for Design 3	30
Figure 3.17 Transition between Stationary and Rotating Domains for Design 3	30
Figure 3.18 Prism Mesh Layers around Blade in Rotating Domain for Design 3	31
Figure 3.19 Mesh Metrics Spectrum. (Source: Ozen Engineering, 2014)	32
Figure 3.20 Monitors for Conventional rotor at $V = 6.0$ m/s (a) scaled residual (b) moment coefficient (c) drag coefficient (d) lift coefficient	37
Figure 3.21 Monitors for Conventional rotor at $V = 8.23$ m/s (a) scaled residual (b) moment coefficient (c) drag coefficient (d) lift coefficient	38
Figure 3.22 Monitors for Conventional rotor at $V = 10.17$ m/s (a) scaled residual (b) moment coefficient (c) drag coefficient (d) lift coefficient	39
Figure 3.23 Monitors for Design 1 rotor at $V = 6.0$ m/s (a) scaled residual (b) moment coefficient (c) drag coefficient (d) lift coefficient	40
Figure 3.24 Monitors for Design 1 rotor at $V = 8.23$ m/s (a) scaled residual (b) moment coefficient (c) drag coefficient (d) lift coefficient	41
Figure 3.25 Monitors for Design 1 rotor at $V = 10.17$ m/s (a) scaled residual (b) moment coefficient (c) drag coefficient (d) lift coefficient	42
Figure 3.26 Monitors for Design 2 rotor at $V = 6.0$ m/s (a) scaled residual (b) moment coefficient (c) drag coefficient (d) lift coefficient	43
Figure 3.27 Monitors for Design 2 rotor at $V = 8.23$ m/s (a) scaled residual (b) moment coefficient (c) drag coefficient (d) lift coefficient	44
Figure 3.28 Monitors for Design 2 rotor at $V = 10.17$ m/s (a) scaled residual (b) moment coefficient (c) drag coefficient (d) lift coefficient	45
Figure 3.29 Monitors for Design 3 rotor at $V = 6.0$ m/s (a) scaled residual (b) moment coefficient (c) drag coefficient (d) lift coefficient	46
Figure 3.30 Monitors for Design 3 rotor at $V = 8.23$ m/s (a) scaled residual (b) moment coefficient (c) drag coefficient (d) lift coefficient	47
Figure 3.31 Monitors for Design 3 rotor at $V = 10.17$ m/s (a) scaled residual (b) moment coefficient (c) drag coefficient (d) lift coefficient	48
Figure 4.1 Coefficient of moment against inlet velocity for conventional rotor, design 1, design 2 and design 3	51

Figure 4.2 Torque per height against inlet velocity for conventional rotor, design 1, design 2 and design 3	52
Figure 4.3 Coefficient of performance against inlet velocity for conventional rotor, design 1, design 2 and design 3	52
Figure 4.4 Variation of torque of conventional rotor with time value for $V = 6.0$ m/s	54
Figure 4.5 Variation of torque of conventional rotor with time value for $V = 8.23$ m/s	55
Figure 4.6 Variation of torque of conventional rotor with time value for $V = 10.17$ m/s	56
Figure 4.7 Variation of torque of Design 1 rotor with time value for $V = 6.0$ m/s	57
Figure 4.8 Variation of torque of Design 1 rotor with time value for $V = 8.23$ m/s	58
Figure 4.9 Variation of torque of Design 1 rotor with time value for $V = 10.17$ m/s	59
Figure 4.10 Variation of torque of Design 2 rotor with time value for $V = 6.0$ m/s	60
Figure 4.11 Variation of torque of Design 2 rotor with time value for $V = 8.23$ m/s	61
Figure 4.12 Variation of torque of Design 2 rotor with time value for $V = 10.17$ m/s	62
Figure 4.13 Variation of torque of Design 3 rotor with time value for $V = 6.0$ m/s	63
Figure 4.14 Variation of torque of Design 3 rotor with time value for $V = 8.23$ m/s	64
Figure 4.15 Variation of torque of Design 3 rotor with time value for $V = 10.17$ m/s	65
Figure 4.16 Velocity Distribution for $V = 6.0$ m/s (a) Conventional (b) Design 1 (c) Design 2 (d) Design 3	67
Figure 4.17 Velocity Distribution for $V = 8.23$ m/s (a) Conventional (b) Design 1 (c) Design 2 (d) Design 3	68
Figure 4.18 Velocity Distribution for $V = 10.17$ m/s (a) Conventional (b) Design 1 (c) Design 2 (d) Design 3	69
Figure 4.19 Pressure Distribution for $V = 6.0$ m/s (a) Conventional (b) Design 1 (c) Design 2 (d) Design 3	70
Figure 4.20 Pressure Distribution for $V = 8.23$ m/s (a) Conventional (b) Design 1 (c) Design 2 (d) Design 3	71
Figure 4.21 Pressure Distribution for $V = 10.17$ m/s (a) Conventional (b) Design 1 (c) Design 2 (d) Design 3	72

LIST OF TABLES

Table 1 Conventional Split Savonius Dimensions (Source: U.K Saha, 2008)	18
Table 2 Design 1 Dimensions	19
Table 3 Design 2 Dimensions	20
Table 4 Design 3 Dimensions	21
Table 5 Variation of Reynolds Number and Turbulence Intensity. (Source: U.K Saha, 2008)	23
Table 6 Estimated values of turbulent kinetic energy and turbulent dissipation rate. (Source: U.K Saha, 2008)	24
Table 7 Details of specific dissipation rate and turbulent viscosity ratio. (Source: U.K Saha, 2008)	24
Table 8 Total Number of Elements and Nodes	31
Table 9 Mesh quality metrics	31
Table 10 Percentage difference between torque CFD and torque U.K Saha et al.	50

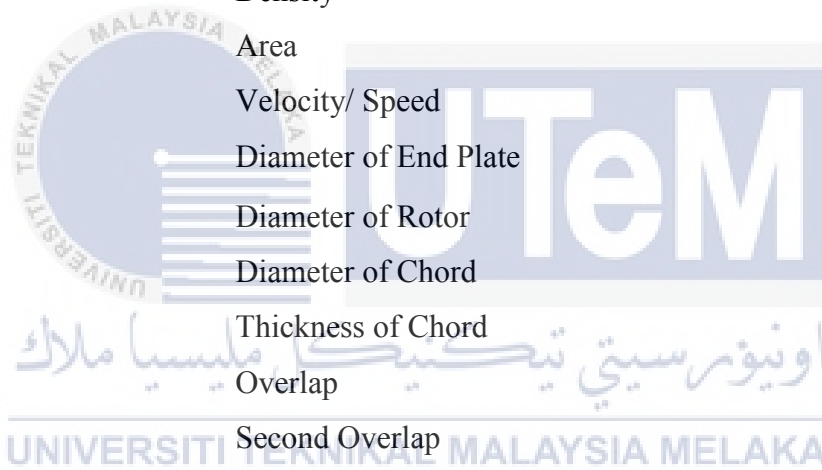
UNIVERSITI TEKNIKAL MALAYSIA MELAKA

LIST OF ABBREVIATIONS

BC	Before Century
HAWT	Horizontal Axis Wind Turbine
VAWT	Vertical Axis Wind Turbine
CFD	Computational Fluid Dynamics
CAD	Computer Aided Drawing
2D	Two Dimensional
3D	Three Dimensional
RANS	Reynolds Average Navier Stokes
LES	Large Eddy Simulation
DNS	Direct Numerical Simulation
PDE	Partial Differential Equation
ASM	Algebraic Stress Model
RSM	Reynolds Stress Model
TBS	Tandem Blade Savonius
TSR	Tip Speed Ratio
RPM	Rotational Per Minute

LIST OF SYMBOLS

COP	Power Coefficient/ Coefficient of Performance
P_s	Shaft Power/ Mechanical Power
P	Power Available in The Wind
T	Torque
Ω	Angular Velocity/ Rotational Velocity
ρ	Density
A	Area
V	Velocity/ Speed
D_f	Diameter of End Plate
D	Diameter of Rotor
D_c	Diameter of Chord
T_c	Thickness of Chord
e	Overlap
e'	Second Overlap
N	Frequency of Rotation (rpm)
λ	Tip Speed Ratio



CHAPTER 1

INTRODUCTION

1.1 BACKGROUND

The Sun radiates 1.74×10^{17} W energy to the Earth per hour and approximately 2% of this energy is converted into wind energy (Energy and Environment, 2016). Wind has been used as a source of energy as early as 5000 BC when wind energy is used to propel boats along Nile River (Wind Energy Foundation, 2016). By the end of 2015, 432.9GW wind power capacity has been installed globally led by Germany and United States of America (Global Wind Energy Council, 2016). This improvement has been possible with the use of wind turbine technology. Wind turbine is used to generate electricity by converting kinetic energy of the wind into mechanical energy which is used to turn the rotor and power up the generator, thus, generating electricity.

There are two types of wind turbine; horizontal axis wind turbine (HAWT) and vertical axis wind turbine (VAWT). These wind turbines can operate on either lift force, drag force or the combination of both. HAWT dominates the wind industry due to its efficiency compared to VAWT (Vertical Axis Wind Turbines vs Horizontal Axis Wind Turbines, 2009). HAWT is capable of achieving efficiency up to 50% whilst VAWT is only able to achieve efficiency approximately 15% (John Patrick Abraham, 2012). However, there are two types of VAWT which have the potential of being developed; Savonius wind turbine and Darrieus wind turbine (Figure 1.1) (Barnard, 2014). Conventional Savonius wind turbine (Figure 1.2) operates on drag force whereas Split Savonius wind turbine (Figure 1.3) operates on the combination of lift and drag forces (Fluid Mechanics: Fundamentals and Applications, 2010). Savonius wind turbine has low

efficiency due to lack of body force and surface force (Bagus Wahyudi, Sudjito Soeparmanb, H W M Hoeijmakersc, 2014). However, Savonius wind turbine is built due to its uncomplicated and low cost construction (Bagus Wahyudi, Sudjito Soeparmanb, H W M Hoeijmakersc, 2014) (Abdul Qadir Versiani, 2015). It is a slow rotating machine with higher torque compared to Darrieus wind turbine. Savonius rotor is not affected by the direction of wind thus suitable for non-uniform wind areas (Bagus Wahyudi, Sudjito Soeparmanb, H W M Hoeijmakersc, 2014) (Abdul Qadir Versiani, 2015). It is normally used for small water pumping applications.

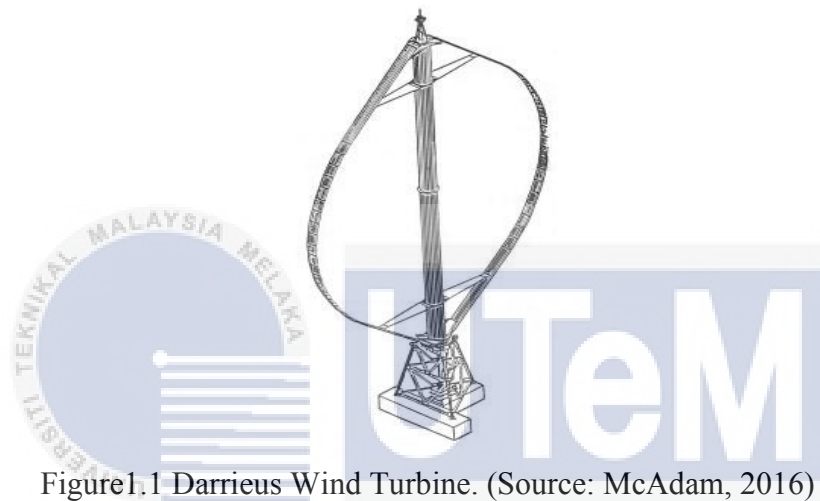


Figure 1.1 Darrieus Wind Turbine. (Source: McAdam, 2016)

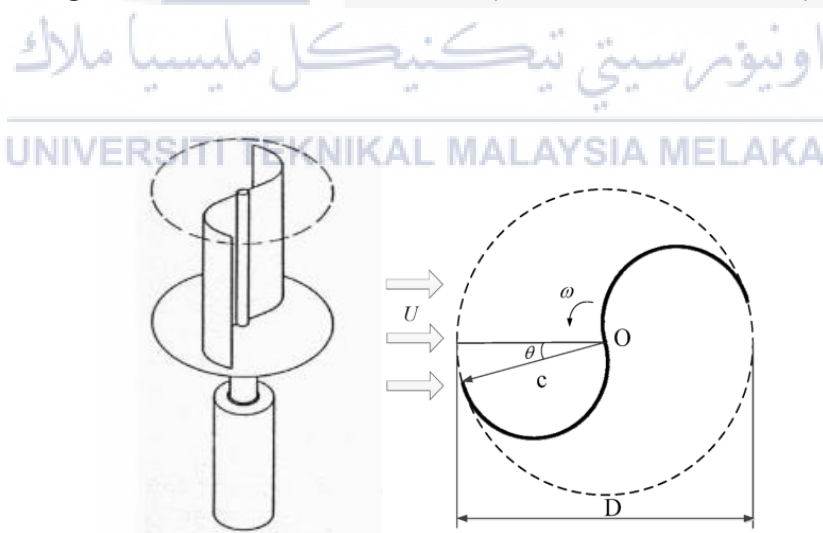


Figure 1.2 Conventional Savonius Wind Turbine. (Source: REUK.co.uk, Wenlong Tian, 2015)

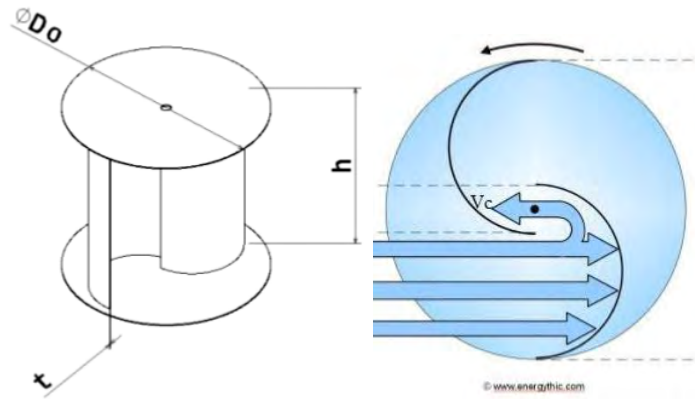


Figure 1.3 Split Savonius Wind Turbine. (Source: Frederikus Wenehenubuna, Andy Saputraa, Hadi Sutanto, 2014)

Basic Split Savonius wind turbine consists of two blades; advance blade and return blade. Advance blade produces drag force from main flow whereas return blade develops return force from opposite direction through a gap between blades called overlap. Overlap serves as an entry of outflow from advance blade to return blade. Overlap is the main difference between Conventional Savonius wind turbine and Split Savonius wind turbine (Bagus Wahyudi, Sudjito Soeparmanb, H W M Hoeijmakersc, 2014). There are few modification done to improve Split Savonius rotor in previous researches such as number of blades, blades twist angle, number of stages, overlap ratio, aspect ratio and end plates presence.

UNIVERSITI TEKNIKAL MALAYSIA MELAKA

1.2 PROBLEM STATEMENT

Savonius wind turbine is a type of vertical axis wind turbine. Vertical axis wind turbine is known for its low efficiency compared to horizontal axis wind turbine. However, Savonius wind turbine possesses few advantages over horizontal axis wind turbine. Savonius wind turbine is used in non-uniform wind areas due to its independency towards direction of wind flow. It has low angular velocity compared to horizontal axis wind turbine but it is capable of generating higher torque. Therefore, in this study, rotor modification will be made to conventional Split Savonius rotor to increase its torque.

1.3 OBJECTIVE

The research objective is:

1. To conduct a two dimensional comparative study between conventional Split Savonius rotor and new configured Split Savonius rotors by performing CFD analysis.

1.4 SCOPE OF PROJECT

The scopes of research are:

1. Wind velocities used are 6.0, 8.23, and 10.17 m/s.
2. Modification is made to conventional Split Savonius rotor by changing the rotor shape to obtain higher torque.
3. Three new rotor configurations are drawn by using commercial software, ANSYS DesignModeler.
4. CFD simulation is performed by using commercial CFD software, ANSYS Fluent to study moment coefficient at the blades.
5. Torque and coefficient of performance are calculated by using these values.

CHAPTER 2

LITERATURE REVIEW

2.1 ENERGY IN THE WIND

According to Albert Betz in 1919, any wind turbine regardless the design, is only capable of converting not more than 59.3% of wind kinetic energy into mechanical energy. Betz limit is also known as the theoretical maximum power efficiency of wind turbines. Power efficiency of wind turbine can be measured by using power coefficient equation, *COP*. *COP* is the ratio between mechanical power and power available in the wind.

$$COP = \frac{P_s}{P} \quad (2.1)$$

Where P_s , is the mechanical power and P is the power available in the wind. Mechanical power of wind turbine can be calculated by using equation (2.2).

$$P_s = T\omega \quad (2.2)$$

Where T is the mechanical torque (Nm) and ω is the angular speed (rad/s). In the present study, brake torque is considered as mechanical torque for above equation. Angular speed can be calculated from equation (2.3).

$$\omega = \frac{2\pi N}{60} \quad (2.3)$$

Where N is the frequency of rotation for the rotor, (rpm).

Power available in the wind can be calculated by using equation (2.4).

$$P = \frac{1}{2}\rho AV^3 \quad (2.4)$$

Where ρ is the air density (kg/m^3), A is the projected area of the rotor (m^2) and V is the wind speed (m/s).

2.2 WIND TURBINE

Bagus wahyudi et al. in his study states that Savonius wind turbine is a pure drag type wind turbine which highly influenced by density, blade sweep area and fluid velocity (Bagus Wahyudi, Sudjito Soeparmanb, H W M Hoeijmakersc, 2014). However, according to Abdullah Al-Faruk et al., it is observed that at low angle of attack, lift force contributes to the overall torque generation which then concluded Savonius wind turbine is a combination of drag and lift forces type of wind turbine (Abdullah Al-Faruk, 2016). As mentioned earlier VAWT has lower efficiency compared to HAWT. Regardless its low efficiency, VAWT is used due to several advantages. VAWT is smaller than HAWT thus requires smaller footprint compared to HAWT. Due to this advantage, some of VAWT application involves other building in which VAWT is mounted to such as cellular communication tower (John Patrick Abraham, 2012). VAWT does not need control system to search for wind direction as it is able to rotate regardless the flow direction. VAWT is able to start rotate at lower wind speed compared to HAWT thus it is suitable to be used for power generation at lower wind speed area. VAWT rotates slower than HAWT resulting in higher mechanical power compared to HAWT.

Figure 2.1 shows the airflow around Savonius rotor. In this figure, rotor is rotated clockwise. Air flow patterns are indicated by streamlines shown. As the inlet is located at bottom side of the figure, the flow is directed upward. Two torques generated by the flow; primary and opposing. Primary torque caused rotation in the direction of wind flow whilst opposing torque caused rotation to slow down. Therefore, in order to improve the rotor, primary torque must be higher than opposing torque.

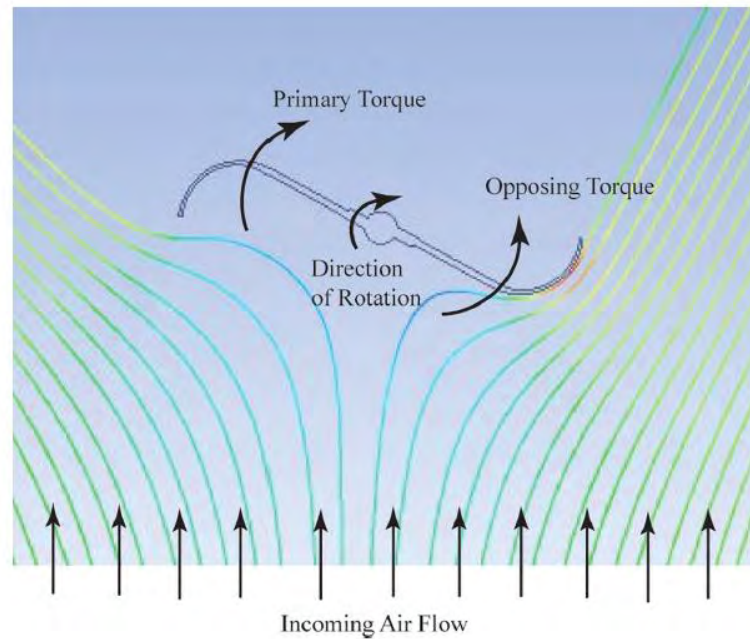
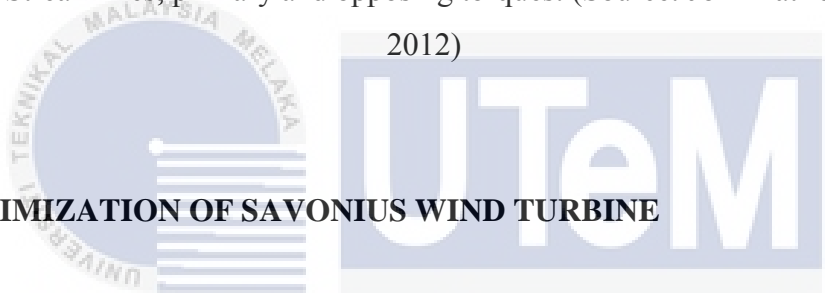


Figure 2.1 Streamlines, primary and opposing torques. (Source: John Patrick Abraham, 2012)



2.3 OPTIMIZATION OF SAVONIUS WIND TURBINE

Number of researches has been conducted to increase the efficiency of Savonius wind turbine. Mohammed Hadi Ali states that performance of Savonius wind turbine is related to these three principles; speed of blade tip is directly proportional to speed of the wind, maximum torque is proportional to the speed of wind squared and maximum power is proportional to the speed of wind cubed (Ali, 2013). Optimization of Savonius wind turbine is measured by using *COP* equation. Thus, researchers normally compared their new configurations with conventional torque which is then used to calculate *COP*.

2.3.1 BLADE DESIGN

Bagus Wahyudi et al. in his study designed a new configuration of blades by adding tandem blades and deflectors to the rotor (Bagus Wahyudi, Sudjito Soeparmanb, H W M Hoeijmakersc, 2014). Tandem blades are used to increase the projected area of the rotor which will improve the surface force thus, increase the force acting on return blade

and improve balancing of the couple forces. Previously, three models with different tandem blades configuration were simulated by CFD; Overlap TBS, Symmetrically TBS and Convergent TBS (B Wahyudi, 2013). By using maximum pressure gap between upstream and downstream equation, it is determined that Convergent TBS is capable of generating more power compared to the others. Water is used as working fluid in this study to increase the fluid momentum force acting on the blade. Response surface method and CFD show the variation in velocity and pressure near blades region. Pressure gap occurs across the rotor from upstream to downstream area indicate that power extracted by the rotor is causing it to rotate. Static pressure on convex side of both blades is lower than those on concave side due to high water velocity flowing over the convex side which produce torque to rotate the blades. Drag force acting on the return blade is increased due to compartment gap narrowing in tandem blades adjacent to the axis which increase pressure dynamics on the concave blades. It is observed that with the use of both deflector and tandem blade, velocity ratio on narrow gap and torque produced by drag force on return blade are improved compared to the configuration with tandem blades alone. Deflector caused positive static moment at any tip diameter for both angle deflector designs; radial and tangential whilst configuration without deflector shows the presence of negative values in some range.

Abdul Qadir Versiani et al. claimed in his study that twisted blade has lower negative projected area compared to conventional blade (Abdul Qadir Versiani, 2015). Twisted design caused the air flow to be swept inward and outward, creating a couple which ensure smooth rotation with higher rotational velocity and torque. An increase in velocity drop is shown from the inlet to the outlet via static and rotational analysis whilst static pressure contour shows that static pressure decreases from upstream to downstream area of the rotor which produces drag force and torque for the rotor. It is proven in his study that the optimum twisted angle is 40° as shown in Figure 2.2 where maximum velocity drop across the blade is achieved. It shows that most kinetic energy of the wind is successfully converted into mechanical energy. A study on twisted Savonius rotor is also performed by A. Reza Hassanzadeh et al. to study the comparison between conventional and Helical Savonius Marine Current Turbine (A. Reza Hassanzadeh, 2013). This study is using water as working fluid. Helical is chosen because twisted rotor has better self-start ability. It rotates smoothly but with high RPM at low flow velocity. Twisted rotor also has higher average power output and operates steadily. CFD is used to simulate helical rotor as

shown in Figure 2.3. The turbine has two end plates and has no central shaft. The findings show that velocity increases at the back of advanced rotor and highest velocity occurred at the edge of helical blade. However, it is shown that relative velocity vector of conventional rotor is higher than optimized rotor. Overall, helical efficiency is proven to be higher than conventional efficiency. The result is due to absence of negative torque around helical turbine.

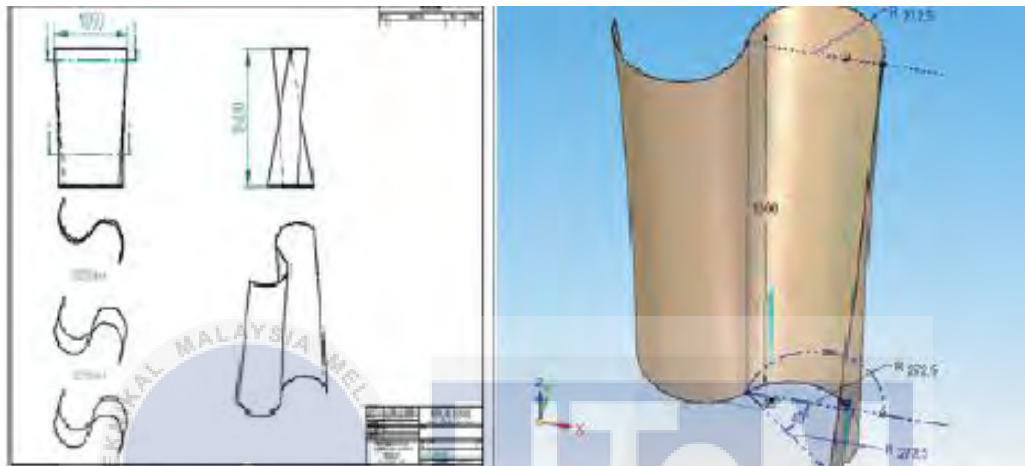


Figure 2.2 40 Degree Twisted Blade. (Source: Abdul Qadir Versiani, 2015)



Figure 2.3 3D view of helical Savonius turbine. (Source: A. Reza Hassanzadeh, 2013)

In another study, six different rotor configurations are tested by using artificial neural networks to study the power factor of each configuration (J., 2007). The findings show that all configurations obtained effective result in specific range of tip speed ratio but configuration II has the most effective rotor in different tip speed ratio. Configurations VI

and III also have a reasonable efficiency. The only difference between configurations I and V is the overlap ratio. The test proves that increasing in overlap ratio causes sudden increase in power factor and intense decrease in drag force.

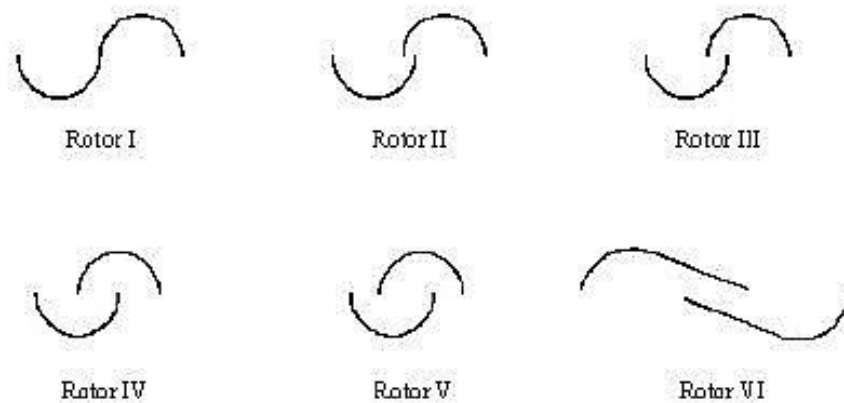


Figure 2.4 Rotor configurations. (Source: J., 2007)

2.3.2 NUMBER OF BLADES

Frederikus Wenehenubun et al. in his study constructed three configurations of wind turbine; two-bladed rotor, three-bladed rotor and four-bladed rotor, to study the effect of number of blades to tip speed ratio, torque and power coefficient (Frederikus Wenehenubuna, Andy Saputraa, Hadi Sutanto, 2014). Tip speed ratio (TSR) is the ratio between speeds of tip blade to the wind speed. TSR is affected by the rotational speed of rotor. High TSR shows that the wind turbine has high rotational speed. TSR can be calculated by using equation (2.5).

$$\lambda = \frac{\omega d}{V} \quad (2.5)$$

Where V is the wind speed, ω is the angular velocity of rotor and d is the blade diameter.

By using wind tunnel, it is observed that three-bladed Savonius rotor has the highest TSR whilst four-bladed rotor has higher torque compared to two and three bladed rotors. It shows that four-bladed rotor has higher drag force at any position when it is

rotating. Number of blades has an impact on solidity and increase in solidity produces higher torque value. The number of *COP* for two-bladed rotor increases corresponding to the increase in TSR but produces less power compared to the other. Four-bladed rotor produces highest *COP* among all but it is unstable compared to three-bladed rotor. *COP* of four-bladed rotor starting to decrease after wind speed of 6 m/s. It is concluded that four-bladed rotor has good *COP* at lower TSR whilst three-bladed rotor has great *COP* at higher TSR. In other research, it is documented that *COP* for two-bladed rotor is higher compared to three and four bladed rotor (N.H. Mahmoud a, A.A. El-Haroun, E. Wahba a, M.H. Nasef, 2010) contrary to the previous study. Two-bladed rotor has higher drag force which produces higher torque compared to the other. In this study, other parameters are also tested such as number of stages, overlap ratio and aspect ratio to study the interdependence of *COP* to these parameters. Two-bladed rotor obtained highest *COP* for all optimization. The results obtained are validated from previous work of similar optimization. Mohammed Hadi Ali in his research study the performance of two and three bladed rotor at low speed shows that two-bladed rotor has higher efficiency compared to three-bladed rotor (Ali, 2013). He claimed that drag surface increases as number of blades increases thus, creates higher reverse torque which decreases net torque acting on the rotor. Experiment is carried out by using subsonic wind tunnel.

2.3.3 END PLATE DESIGN

Altan et al. in his paper, study the usage of end plate on top and bottom of Savonius rotor. He states that end plates are useful to prevent air leakage from the concave side. It is concluded in the study that the arrangement increases performance of Savonius rotor (B. D. Altan, 2008). Following that research, N.H. Mahmoud et al. states that rotor with end plates generates higher mechanical power compared to rotor without end plates. End plates increases amount of air strikes the Savonius rotor (N.H. Mahmoud a, A.A. El-Haroun, E. Wahba a, M.H. Nasef, 2010).

2.3.4 NUMBER OF STAGES

A study is carried by N.H. Mahmoud et al. to study the performance of Savonius rotor with additional stages. Single stage and double stages are compared. It is shown that double stages rotor has higher static torque compared to single stage (N.H. Mahmoud a, A.A. El-Haroun, E. Wahba a, M.H. Nasef, 2010). A study is conducted by U.K Saha et al. to observe the effect of number of stages; single, two and three, to the Savonius performance (U.K Saha, 2008). Wind tunnel is used to test the parameter. The findings show that *COP* increases when number of stages increased from single stage to two stages. However, *COP* decreases when number of stages is increased from two stages to three stages. It is stated in the study that the result is due to an increase in inertia of the rotor. Thus, it is concluded that the optimum number of stages is two. Results from both studies show similarity.

2.3.5 OVERLAP RATIO

N.H. Mahmoud et al. also studied the effect of variation overlap ratio to Savonius rotor performance (N.H. Mahmoud a, A.A. El-Haroun, E. Wahba a, M.H. Nasef, 2010). It is observed that rotor without overlap generates higher mechanical power compared to rotor with overlap. In a 2D CFD study, overlap ratios are varied to observe the effect of overlap ratio to static torque (Sukanta Roy, 2013). Static torque is a function of overlap ratio. By using realizable k- ϵ model, overlap ratio of 0, 0.10, 0.15, 0.20, 0.25 and 0.30 are simulated. The study shows that static torque performance increases with the increase of overlap ratio from 0 to 0.15. Initially at 0 overlap ratio, a large variation of static torque value is detected at various angular positions. Overlap absence also causes negative static torque coefficient at 105° to 150° and at 285° to 330° . The increase in static torque corresponds to the increase in overlap is due to increase in pressure on concave side of the return blade. However, as the overlap increases beyond optimum value of 0.20, the effective pressure on advance blade concave side decreases.

2.3.6 ASPECT RATIO

Aspect ratio is the ratio between rotor height and rotor diameter. A study shows that power coefficient increases correspond to aspect ratio (N.H. Mahmoud a, A.A. El-Haroun, E. Wahba a, M.H. Nasef, 2010).

2.4 COMPUTATIONAL FLUID DYNAMICS

Turbulence model is a computational procedure to close the system of mean flow equations. It allows the calculation of mean flow without first solving the full time-dependent flow field. There are many types of turbulence models to complete the closure process; Reynolds Average Navier Stokes Equation (RANS), Large Eddy Simulation (LES) and Direct Numerical Simulation (DNS). In RANS simulation, all large and small scales of turbulence are modelled so that mesh refinement such in DNS is unnecessary. RANS consists of few models; zero equation model, one equation model, two equations models, seven equations models and algebraic stress models. The number of equation indicates the number of additional partial differential equations (PDE) solved by the model. Zero equation model or known as Prandtl mixing length model offers solution to close the system without creating extra differential equations. One equation model or known as Spalart-Almaras model provides solution to close the system by solving the turbulent kinetic energy. There are many types of two equations models; k- ϵ models (standard, RNG, realizable), k- ω model and ASM. Seven equations models (second order closure) also known as Reynolds Stress Models (RSM). Another option is the algebraic Reynolds stress models. LES offers more efficient turbulent flow calculation with more refined meshes than required by RANS. In LES simulation, large eddies are calculated whilst small eddies are modelled. There are two main steps involved in the analysis; filtering and sub grid scale modelling. DNS requires highest mesh refinement compared to RANS and LES. It also needs higher order accurate numerical schemes. However, DNS is capable of resolving all turbulence length scales.

A study has been conducted to study the most suitable turbulence model for 2D Savonius rotor (Sukanta Roy, 2013). A 2D CAD is designed by using Gambit modelling software. It consists of inner circle representing turbine model and outer rectangle

representing surrounding area. Unstructured triangular mesh is used for meshing and good quality meshing is ensured throughout both domains; outer and inner. Additional mesh elements are constructed at high pressure gradient around the blades by using prism mesh layers to capture very sharp velocity gradient. The transition is obvious between two mesh sections; very fine meshing around high pressure gradient area and coarser meshing in outer domain. The meshing setup used resulting in 100 000 cell elements. Boundary conditions are given to the model as such; velocity inlet, pressure outlet, interfaces on both domains around the circle and stationary blade walls. Detailed boundary conditions are as visualized in Figure 2.5. Convergence criterion used to solve Navier Stokes equation is 10^{-3} . Time step size used is 0.001 s. 20 iterations are run per time step for each angular position, velocity and turbulent model. 20000 time steps are needed to obtain number of complete rotations. Model is assumed 2D, unsteady pressure based and requires 2nd order implicit formulation. SIMPLE pressure velocity coupling with 2nd order upwind discretization is used. Model is a k- ϵ turbulence models with enhanced wall function. Simulations are carried for standard k- ϵ , RNG k- ϵ and realizable k- ϵ . Results show better flow prediction is obtained by using RNG k- ϵ and realizable k- ϵ which later narrowed to the most suitable model which is realizable k- ϵ .

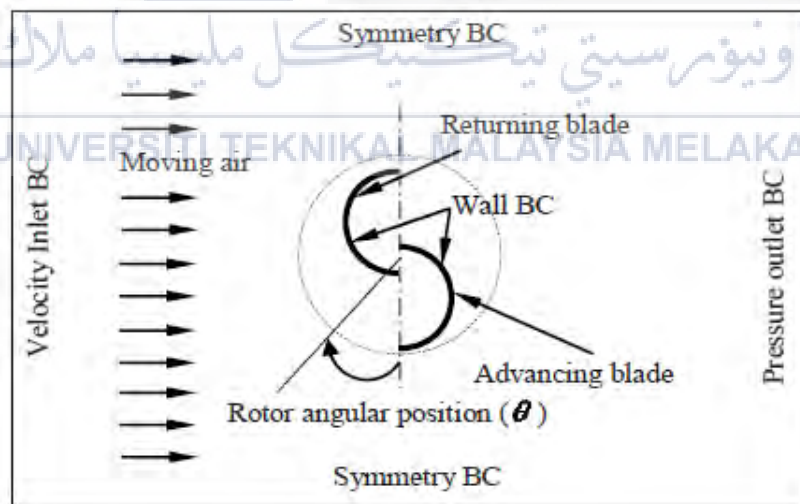


Figure 2.5 Applied boundary conditions. (Source: Sukanta Roy, 2013)

CHAPTER 3

METHODOLOGY

3.1 INTRODUCTION

This chapter describes methodology used in the study to achieve objective stated earlier. General flow chart of this project is as shown in Figure 3.1. Literature review is conducted to study previous optimization made to Savonius rotor. Limitations from previous studies are also identified. Methods and dimensions are adopted from previous study to ensure validated result. ANSYS Fluent is used for CFD analysis.

اونيورسيتي تيكنيكل مليسيا ملاك

UNIVERSITI TEKNIKAL MALAYSIA MELAKA

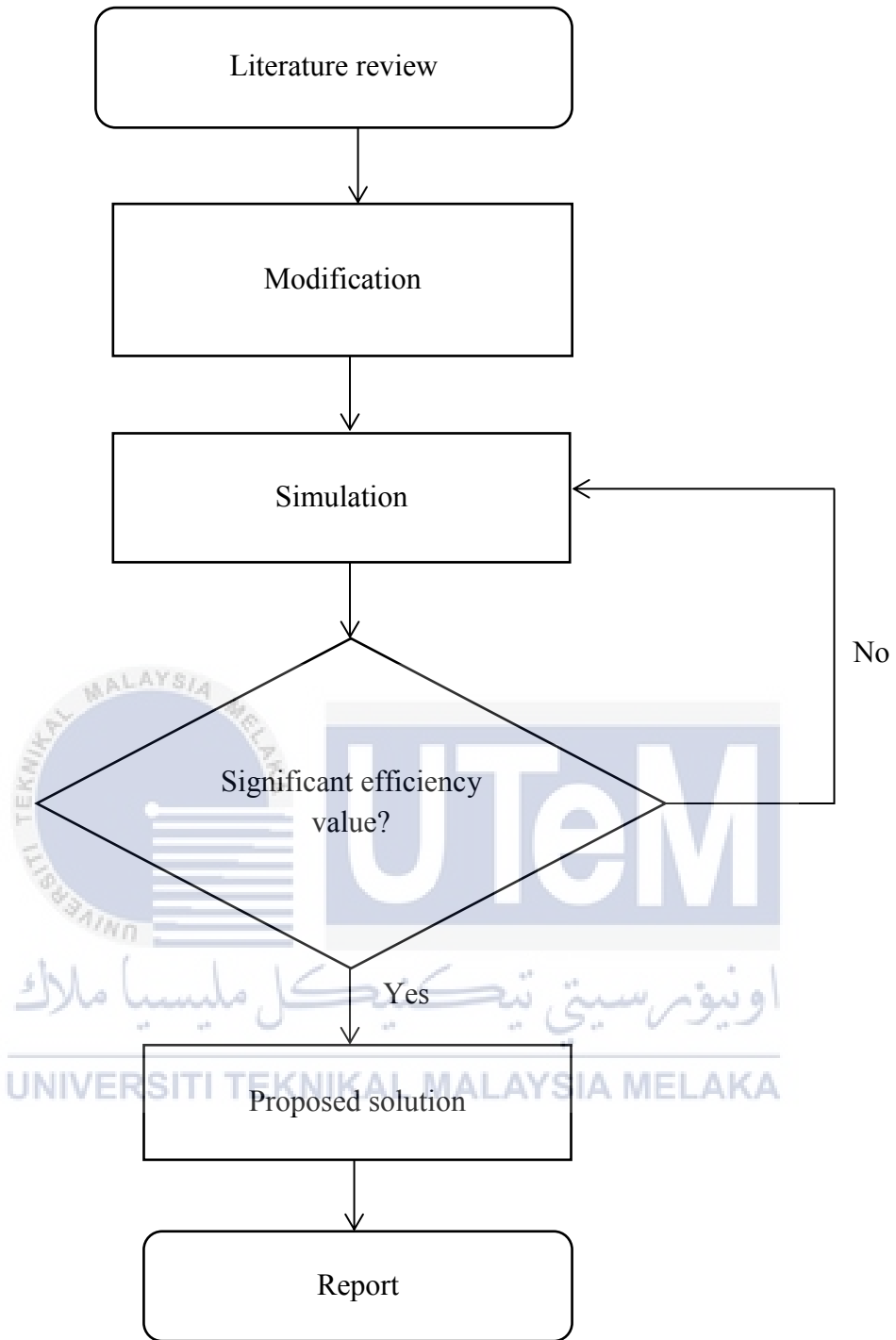


Figure 3.1 Methodology flow chart

3.2 GEOMETRY

In present study, a comparison is made to investigate the power coefficient between conventional Split Savonius rotor and modified Split Savonius rotor. The conventional configuration is based on Split Savonius wind turbine designed by Saha et al. (U.K Saha, 2008). Wind turbine used is a single stage, two-bladed semi-circular rotor with dimensions as in Table 1. Three new configurations are made according to the conventional rotor as shown in Figure 3.4, 3.5 and 3.6 with dimensions as in Table 2, 3 and 4 respectively. CAD drawings of all Split Savonius rotors are created by using DesignModeler in ANSYS. Each drawing consists of two domains; stationary and rotating domains as shown in Figure 3.3 where rectangular shape represents stationary domain while circular shape represents rotating domain. Rotating domains is created by using AddFrozen feature in DesignModeler to separate the flow and analysis from stationary domain. Inlet dimension is 0.375m and rotor axis is located 0.205m away from the inlet according to experimental approach by Saha et al.

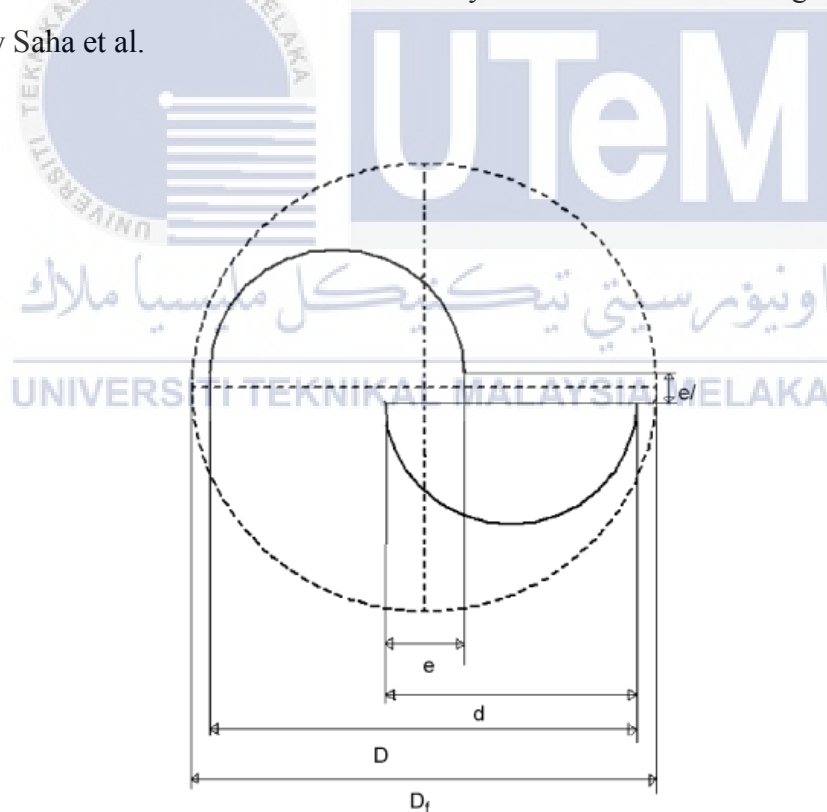


Figure 3.2 Schematic of two-bladed conventional Split Savonius rotor. (Source: U.K Saha, 2008)

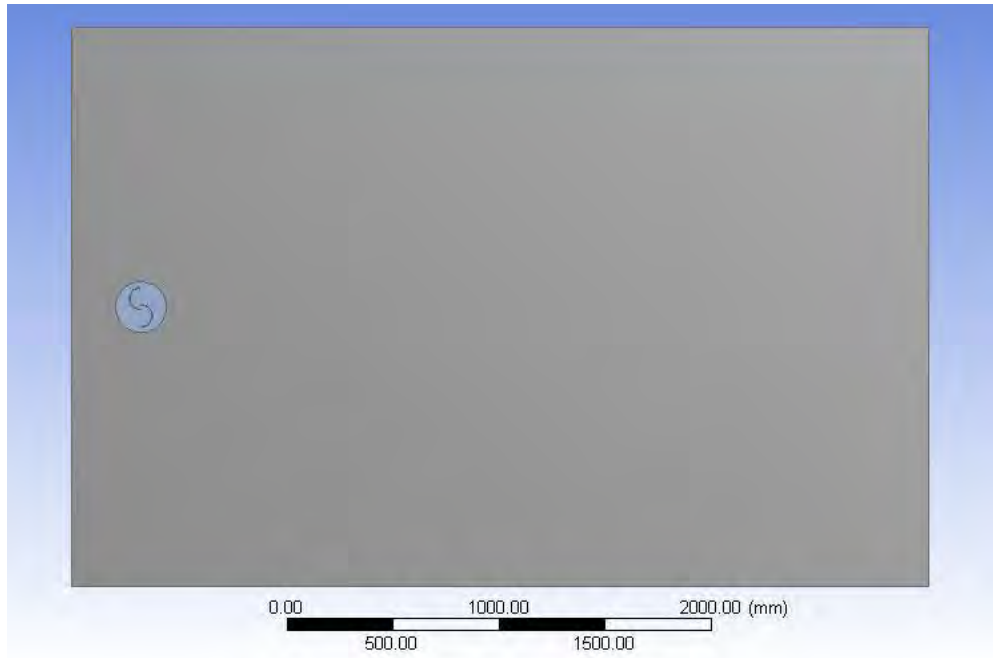


Figure 3.3 CAD drawing of computational domain for Conventional Split Savonius rotor

Table 1 Conventional Split Savonius Dimensions (Source: U.K Saha, 2008)

No.	Geometry	Dimension (m)
1.	Diameter of end plate, D_f	0.23971
2.	Diameter of rotor, D	0.19075
3.	Diameter of chord, d	0.109
4.	Thickness of chord, t	0.003
5.	Overlap, e	0.02725
6.	Second overlap, e'	0.0

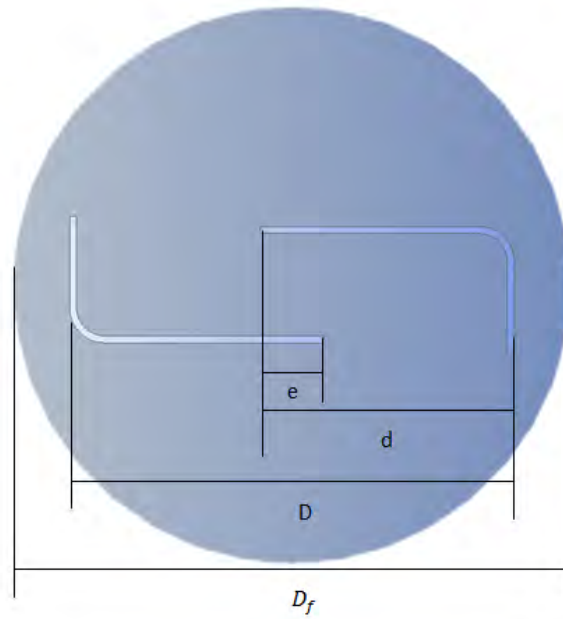


Figure 3.4 Schematic of Design 1

Table 2 Design 1 Dimensions

No.	Geometry	Dimension (m)
1.	Diameter of end plate, D_f	0.23971
2.	Diameter of rotor, D	0.19075
3.	Diameter of chord, d	0.109
4.	Thickness of chord, t	0.003
5.	Overlap, e	0.02725

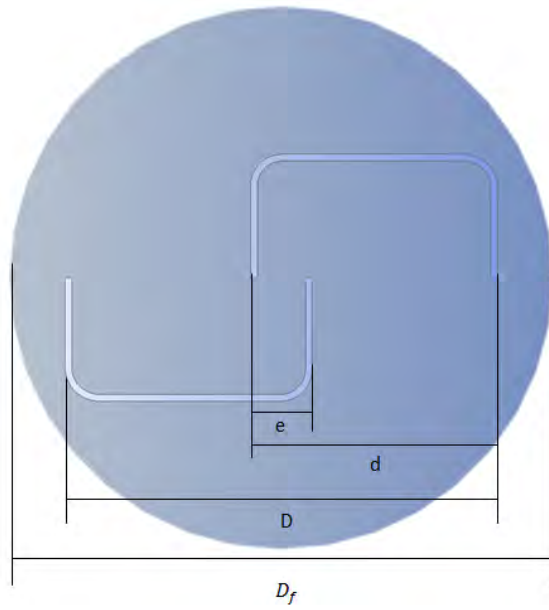


Figure 3.5 Schematic of Design 2

Table 3 Design 2 Dimensions

No.	Geometry	Dimension (m)
1.	Diameter of end plate, D_f	0.23971
2.	Diameter of rotor, D	0.19075
3.	Diameter of chord, d	0.109
4.	Thickness of chord, t	0.003
5.	Overlap, e	0.02725

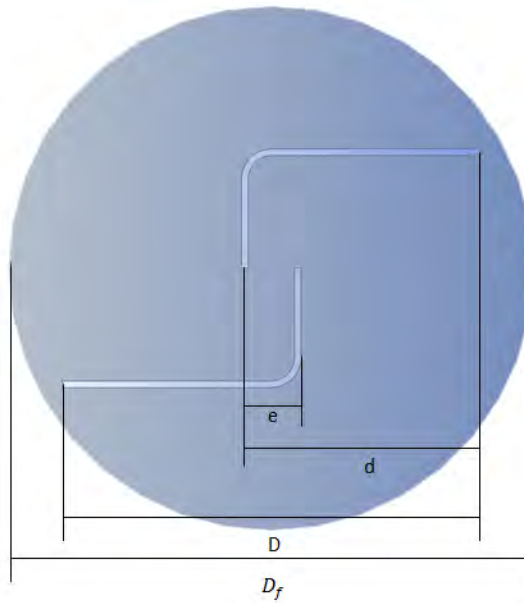


Figure 3.6 Schematic of Design 3

Table 4 Design 3 Dimensions

No.	Geometry	Dimension (m)
1.	Diameter of end plate, D_f	0.23971
2.	Diameter of rotor, D	0.19075
3.	Diameter of chord, d	0.109
4.	Thickness of chord, t	0.003
5.	Overlap, e	0.02725

3.3 MATHEMATICAL MODELLING

In present research, a validation study is conducted to verify the methods used to analyse modified configuration. Computer Aided Design (CAD) model is prepared for conventional configuration based on Saha et al. (U.K Saha, 2008) and new configurations. All drawings are prepared in two dimensional (2D) for transient simulation by CFD. The CAD models consist of two domains interfaced with each other; stationary domain which represent the surrounding area and rotating domain which represents the flow region close to the rotor.

3.3.1 GOVERNING EQUATION

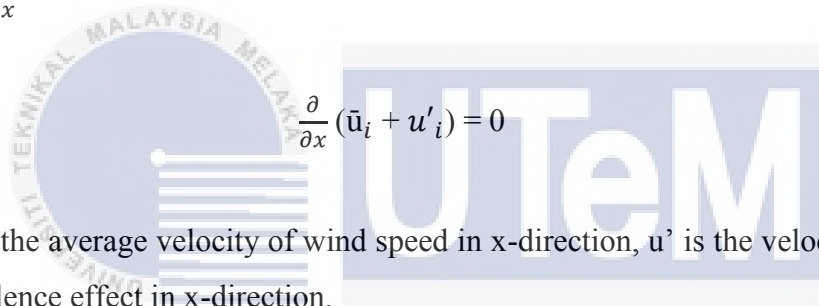
Commercial CFD software, ANSYS Fluent is used to perform the numerical simulation. Mathematical model of the present study consists of continuity equation, momentum equation and turbulence equation. The equations are as follow.

Continuity equation for incompressible flow (Sonu Sharma, 2016):

$$\frac{\partial u}{\partial x} + \frac{\partial v}{\partial y} + \frac{\partial w}{\partial z} = 0 \quad (3.1)$$

$$\frac{\partial v}{\partial y} = 0; \frac{\partial w}{\partial z} = 0 \quad (3.2)$$

Expanding $\frac{\partial u}{\partial x}$


$$\frac{\partial}{\partial x} (\bar{u}_i + u'_i) = 0 \quad (3.3)$$

Where \bar{u}_i is the average velocity of wind speed in x-direction, u' is the velocity fluctuation due to turbulence effect in x-direction.

Momentum equation (Sonu Sharma, 2016):

$$\frac{\partial \bar{u}_i}{\partial t} + \bar{u}_j \frac{\partial \bar{u}_i}{\partial x_j} = - \frac{1}{\rho} \frac{\partial \bar{p}}{\partial x_i} + \frac{\mu}{\rho} \frac{\partial^2 \bar{u}_i}{\partial x_i \partial x_j} - \frac{\partial}{\partial x_j} \overline{u'_i u'_j} \quad (3.4)$$

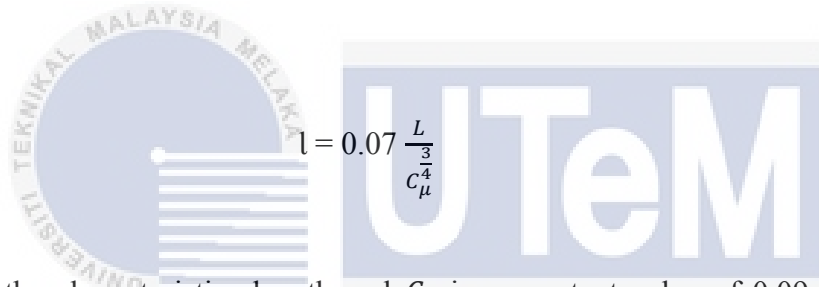
Where t is time, \bar{p} is the average pressure, ρ is the air density and μ is the dynamic viscosity of air.

3.3.2 TURBULENCE MODELLING

In present study, shear stress transport (SST) model is used. This model uses k- ω model for near wall region and k- ϵ model for far field calculations (Sonu Sharma, 2016). Torque calculation for rotor is more accurate if the turbulent fluctuation can be captured properly near the blades region. Reynolds number is calculated by using hydraulic diameter as characteristic length, L. Turbulence intensity and turbulent length scale are estimated by using equation (3.5) and (3.6) respectively (Sonu Sharma, 2016).

$$I = \frac{u'}{u_{avg}} = 0.16 (Re)^{\frac{-1}{8}} \quad (3.5)$$

Where u' is the root mean square of the velocity fluctuation and u_{avg} is the mean flow velocity.



$$l = 0.07 \frac{L}{C_{\mu}^{\frac{4}{3}}} \quad (3.6)$$

Where L is the characteristics length and C_{μ} is a constant value of 0.09. Table 5 gives variation of Reynolds number and turbulence intensity correspond to the inlet velocity.

Table 5 Variation of Reynolds Number and Turbulence Intensity. (Source: U.K Saha, 2008)

Inlet Velocity, V (m/s)	Reynolds Number, Re	Turbulence Intensity, I
6	147 486	0.0361
8.23	202 302	0.0347
10.17	249 989	0.338

Turbulent kinetic energy, k and turbulent dissipation rate, ϵ are estimated by using values of I from Table 5 and value of l.

$$k = 1.5 (u_{avg}l)^2 \quad (3.7)$$

$$\varepsilon = \frac{k^{\frac{3}{2}}}{l} \quad (3.8)$$

Specific dissipation rate, ω and turbulent viscosity ratio, β are obtained by using equations (3.9) and (3.10) respectively (Sonu Sharma, 2016).

$$\omega = \frac{k^{\frac{1}{2}}}{C_{\mu} l} \quad (3.9)$$

$$\beta = \frac{\rho C_{\mu} k^2}{\mu \varepsilon} \quad (3.10)$$

Table 6 Estimated values of turbulent kinetic energy and turbulent dissipation rate.

(Source: U.K Saha, 2008)

Inlet Velocity, V (m/s)	Reynolds Number, Re	Turbulent kinetic energy, k	Turbulent dissipation rate, ε
6	147 486	0.0705	0.1173
8.23	202 302	0.1226	0.2688
10.17	249 989	0.1776	0.4686

Table 7 Details of specific dissipation rate and turbulent viscosity ratio. (Source: U.K Saha,

2008)

Inlet Velocity, V (m/s)	Reynolds Number, Re	Specific dissipation rate, ω	Viscosity ratio, β
6	147 486	18.4728	250.3120
8.23	202 302	24.3571	330.0458
10.17	249 989	29.3127	397.1963

3.3.3 MESHING

Performance of Savonius rotor is measured based on *COP* value. Torque on rotor surface is used in order to calculate *COP*. Rotor is treated as wall with no slip condition. In order to obtain accurate value of torque, prism mesh layers with first layer thickness of 0.0001m is formed around each blade. Local sizing is applied at rotating face, rotating edge and blade edges to ensure smooth transition from very fine meshing in boundary layers to fine meshing in stationary domain as shown in Figures 3.7 to 3.9. Stationary domain consists of velocity inlet, pressure outlet, no slip wall, interface and working fluid, which is air at 25°C. Rotating domain consists of interface, blades (treated as no slip conditioned wall) and working fluid which is the same as the other domain. Triangular meshing is used in present study to allow easier meshing of complex shape. Physics and solver preference used are CFD and Fluent respectively. Global sizing is set on proximity and curvature to fill in curve around rotating domain and blades. Relevance center is set to fine and smoothing is set to high. Span angle center is set to fine with curvature normal angle of 5°. Growth rate is set to 1.10 to ensure smooth transition between large elements to smaller elements. The same settings are applied to all new configurations meshing as shown in Figures 3.10 to 3.18. Total nodes and elements obtained with this setting are as listed in Table 8. Mesh quality metrics obtained for current meshing is shown in Table 9.

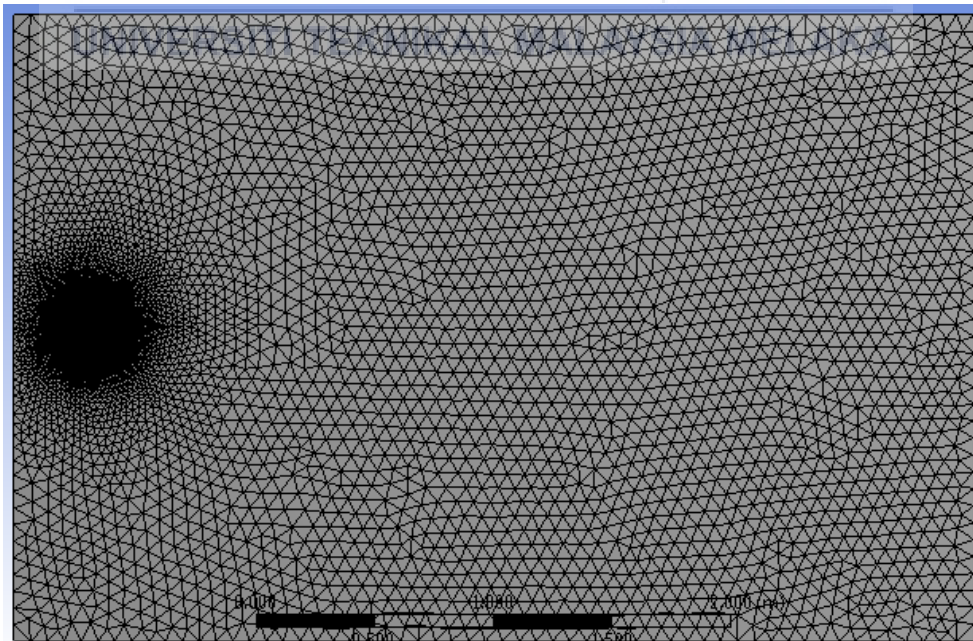


Figure 3.7 Triangular Meshing for Conventional Savonius

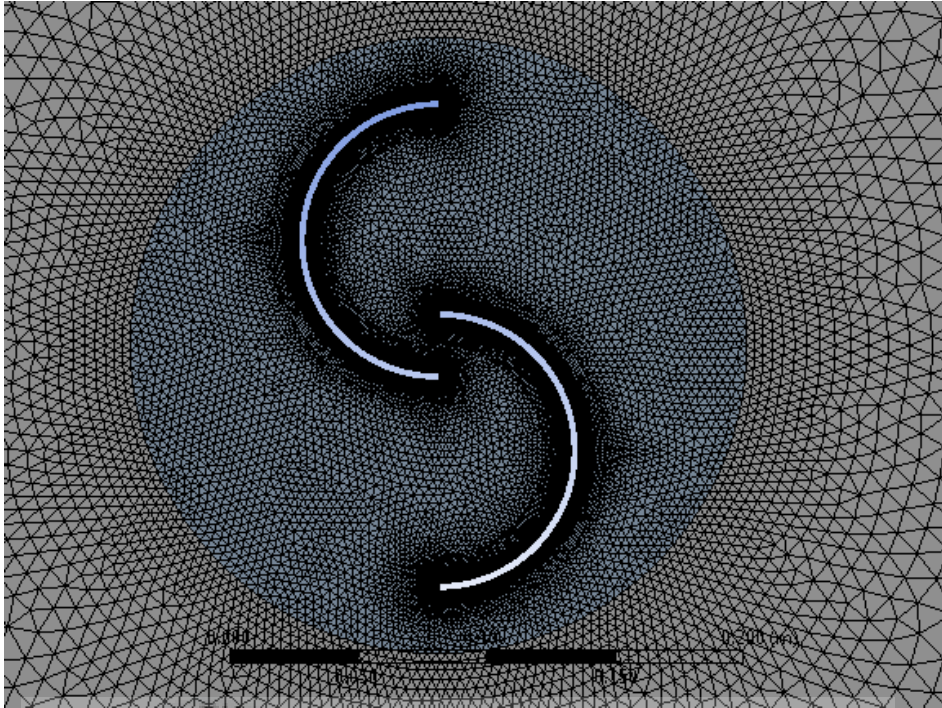


Figure 3.8 Transition between Stationary and Rotating Domains for Conventional Rotor

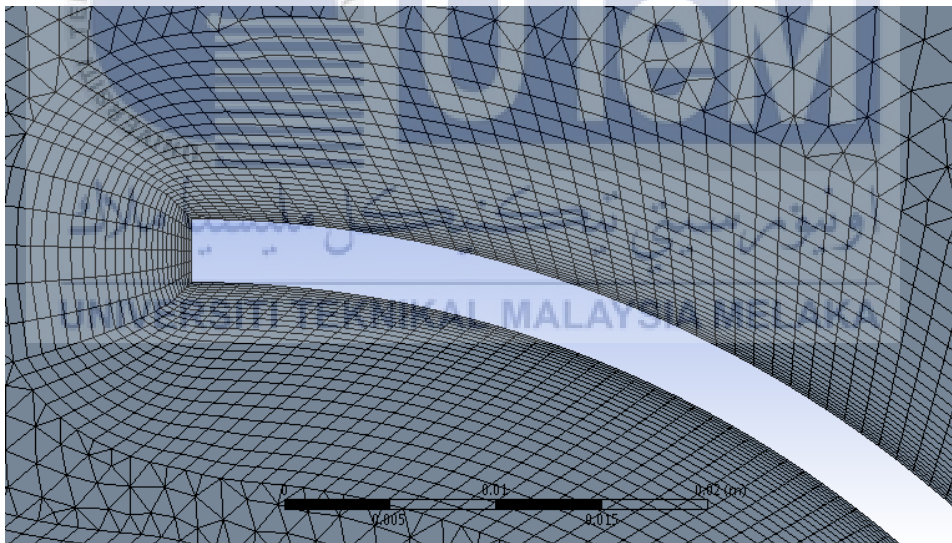


Figure 3.9 Prism Mesh Layers around Blade in Rotating Domain for Conventional Rotor

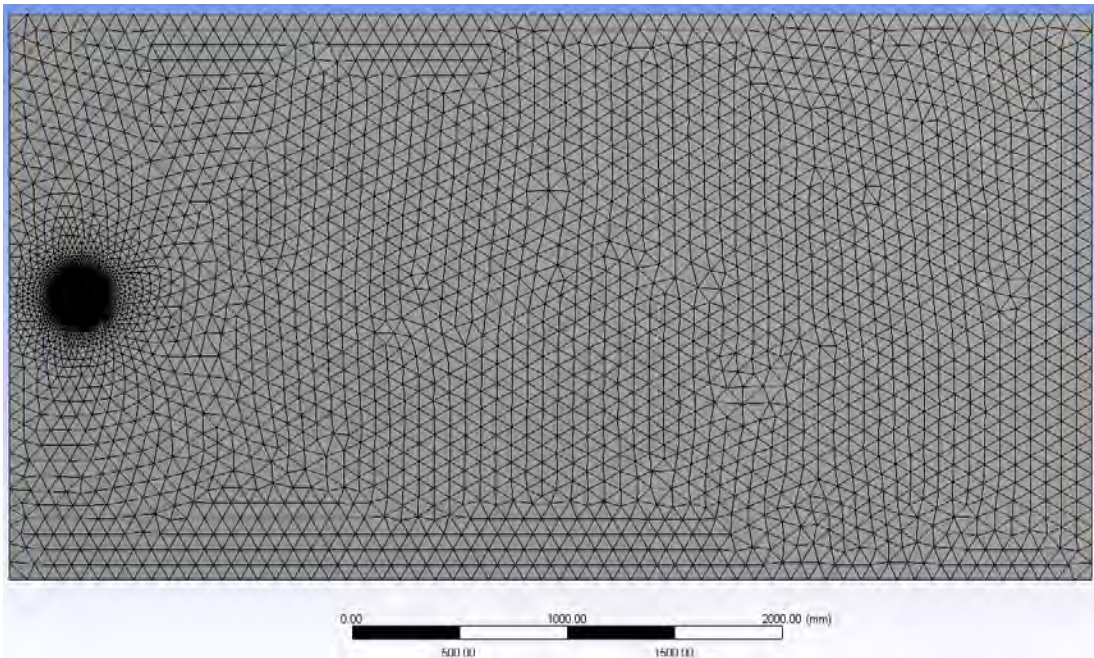


Figure 3.10 Triangular Meshing for Design 1

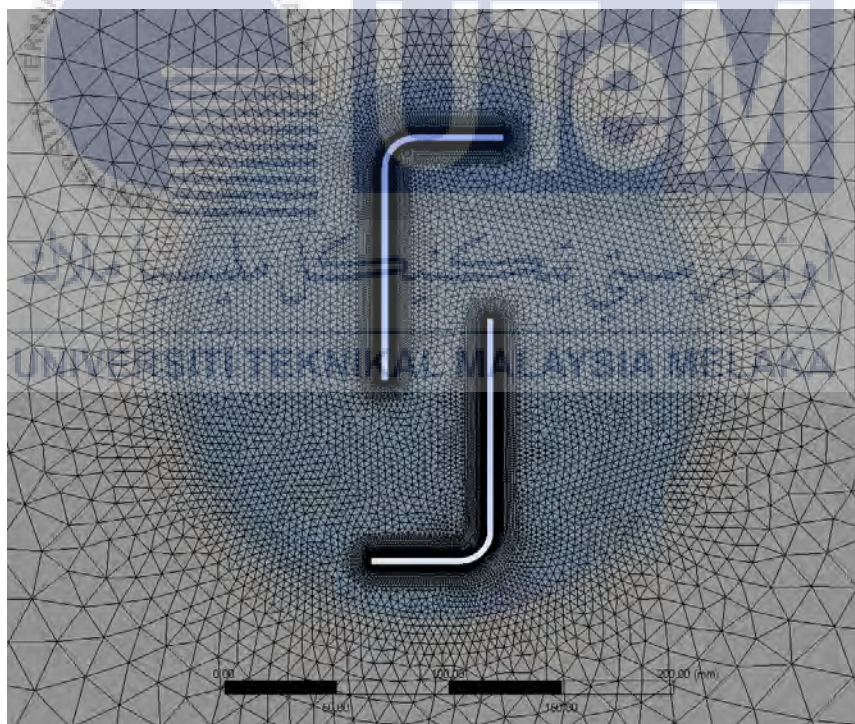


Figure 3.11 Transition between Stationary and Rotating Domains for Design 1

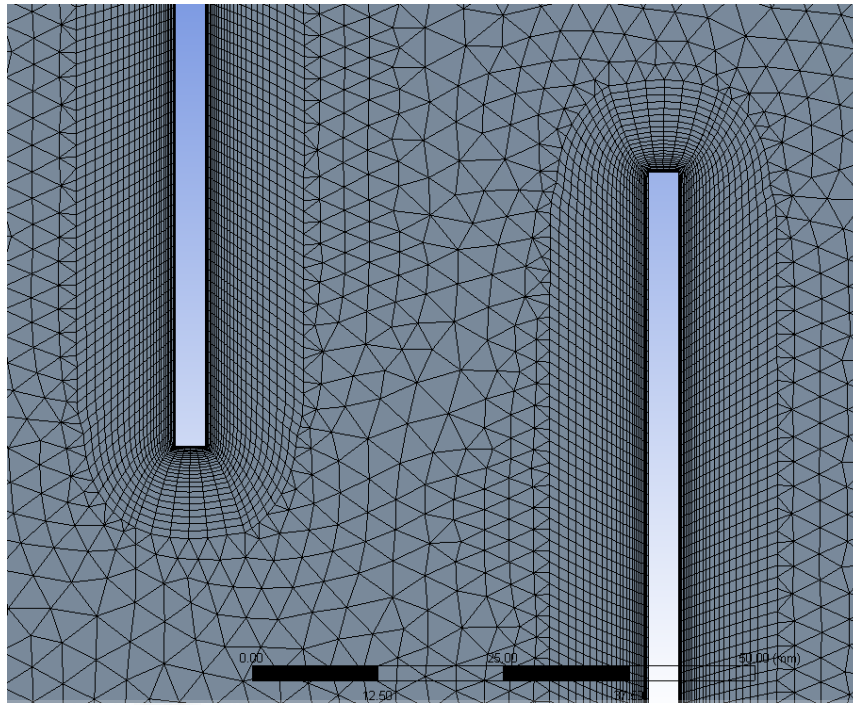


Figure 3.12 Prism Mesh Layers around Blade in Rotating Domain for Design 1

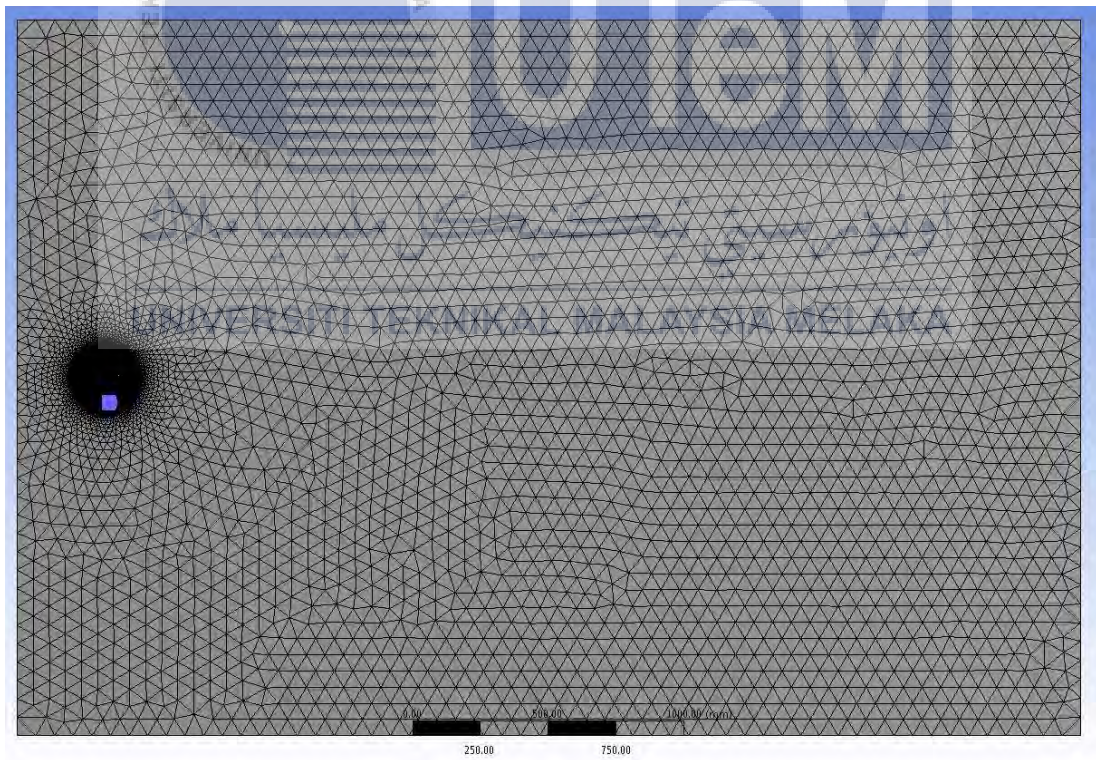


Figure 3.13 Triangular Meshing for Design 2

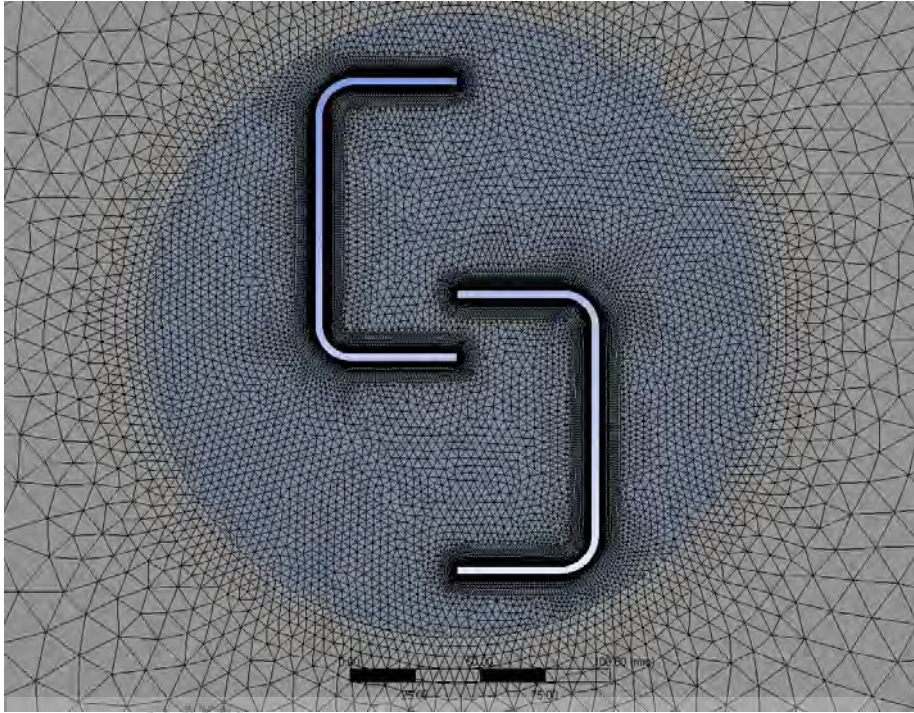


Figure 3.14 Transition between Stationary and Rotating Domains for Design 2

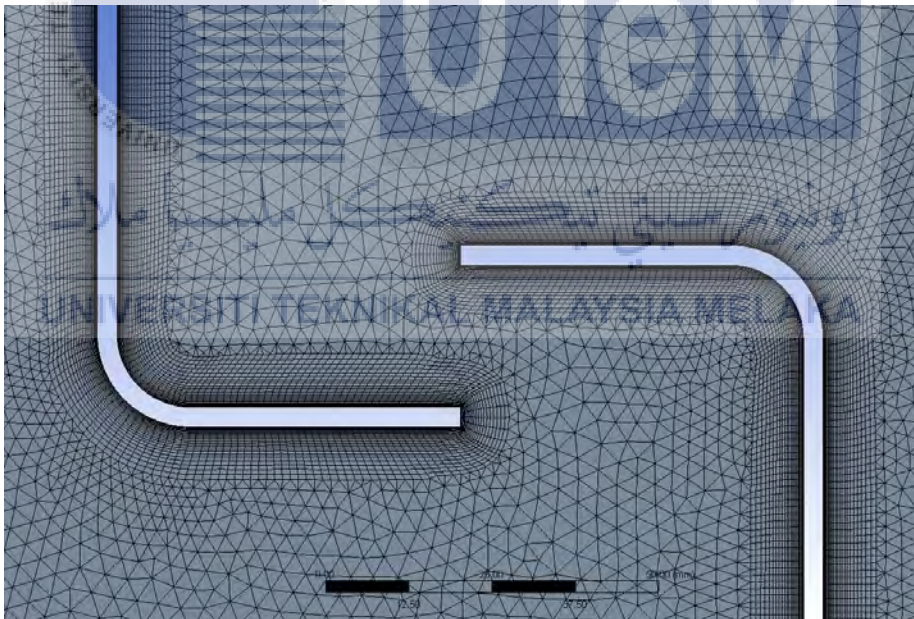


Figure 3.15 Prism Mesh Layers around Blade in Rotating Domain for Design 2

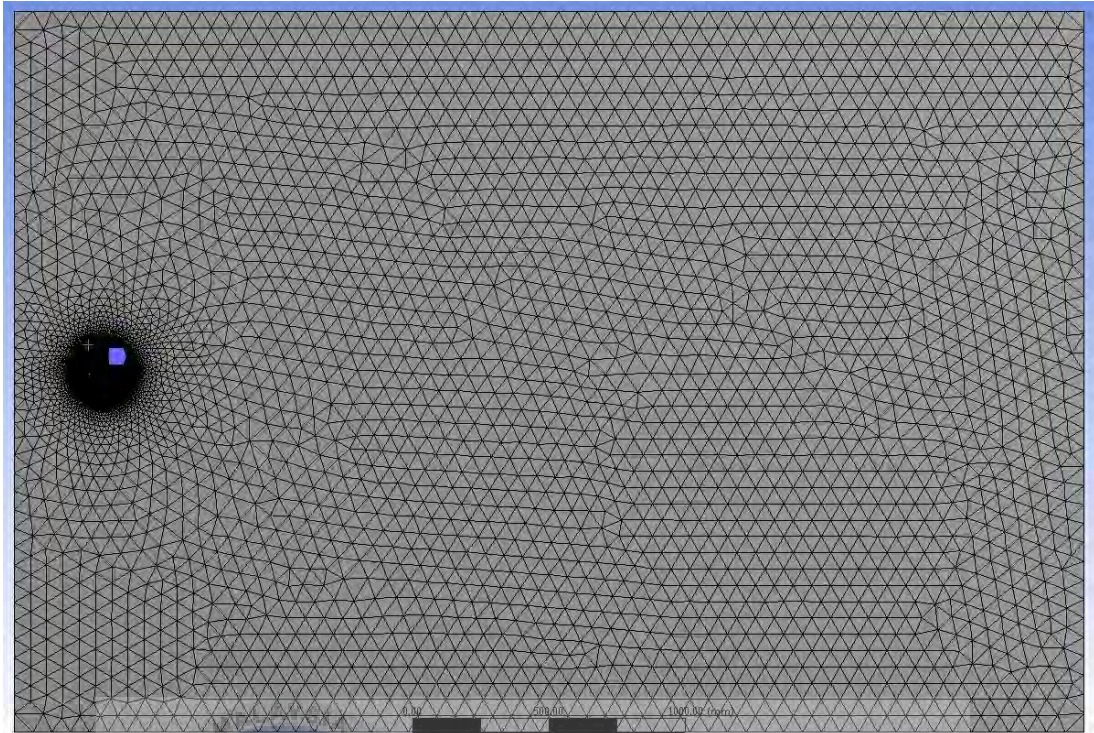


Figure 3.16 Triangular Meshing for Design 3

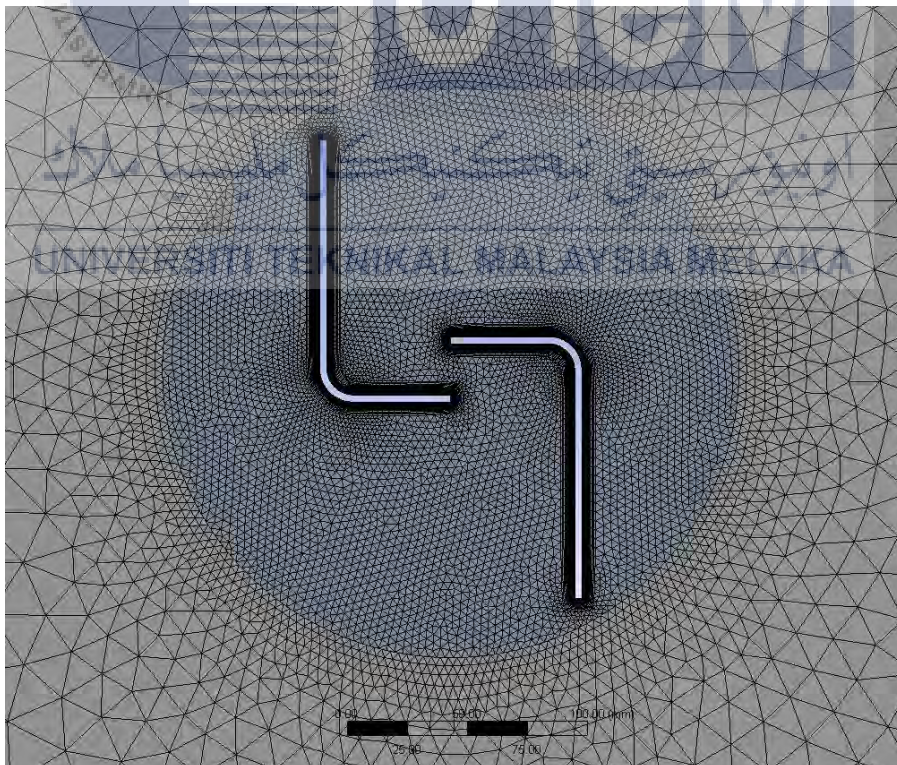


Figure 3.17 Transition between Stationary and Rotating Domains for Design 3

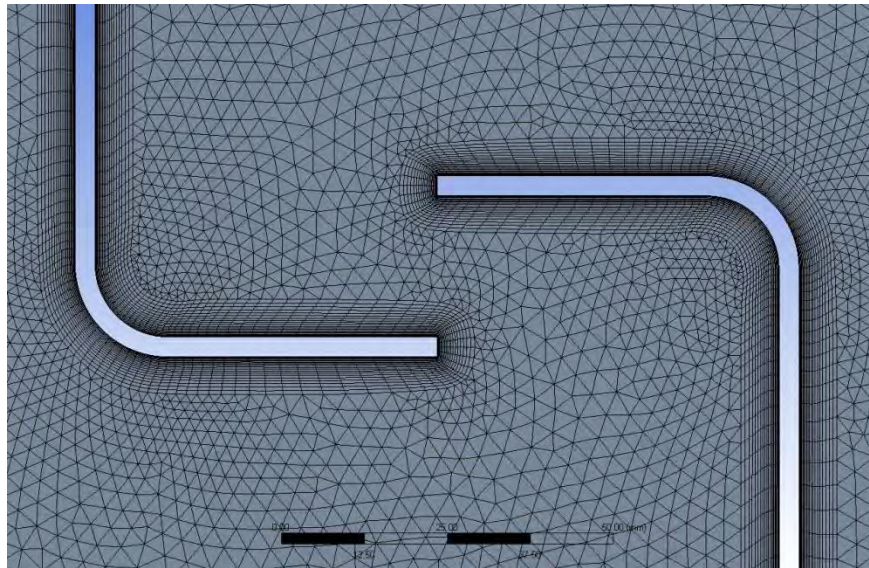


Figure 3.18 Prism Mesh Layers around Blade in Rotating Domain for Design 3

Table 8 Total Number of Elements and Nodes

Rotor	No. of Elements	No. of Nodes
Conventional	41327	30120
New 1	33330	25372
New 2	37700	29173
New 3	25295	16677

Table 9 Mesh quality metrics

Rotor	Orthogonal quality (minimum)	Quality	Skewness (maximum)	Quality
Conventional	0.49545	Good	0.67382	Good
New 1	0.53063	Good	0.78080	Good
New 2	0.43359	Good	0.71156	Good
New 3	0.59145	Good	0.62169	Good

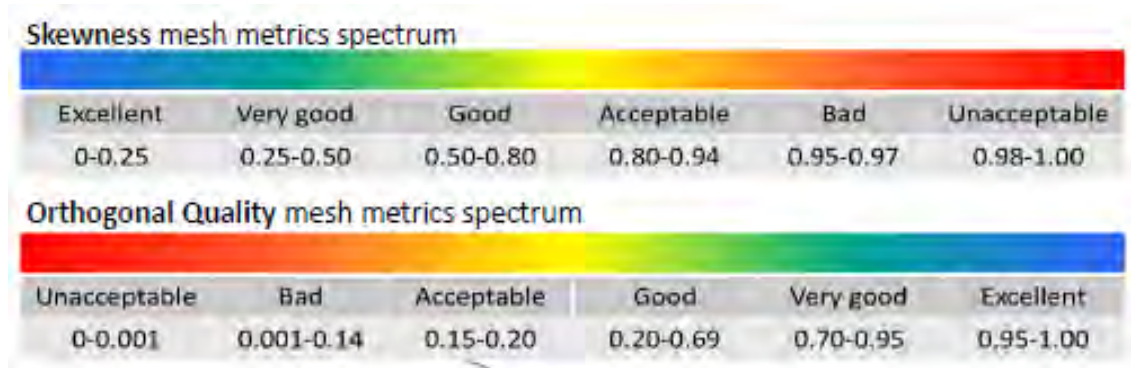


Figure 3.19 Mesh Metrics Spectrum. (Source: Ozen Engineering, 2014)



3.3.4 SETUP AND SOLUTION

ANSYS Fluent is used to perform CFD simulation in current study. 2D transient analysis approach is chosen for simulation instead of 3D because modification applied on blades will only change its 2D geometry. Thus, there is no necessity for 3D simulation as current study will only observe 2D flow around the blades. Boundary condition and initial condition are according to Sonu Sharma et al. Validation study is performed to ensure methods used are reliable thus generating valid results. Validation study is performed by simulating conventional Split Savonius rotor and comparing torque generated to experimental result by Saha et al. Once the methods are validated, the same setting and steps are used to simulate new Savonius configuration. *COP* is calculated to study the efficiency of each rotors.

In ANSYS Fluent, transient analysis is selected with SST turbulence model. Inputs for transition SST model are as calculated in previous study according to wind velocity tested. Working fluid used in current study is air at 25°C where its density, ρ is taken as 1.184 kg m^{-3} , dynamic viscosity, μ is taken as $1.849 \times 10^{-5} \text{ kg m}^{-1} \text{ s}^{-1}$ and ratio of specific heat is taken as 1.4. Mesh motion is activated for rotating domain as sliding mesh will be performed in this study. Rotor is treated as no slip wall with rotational motion relative to rotating domain while other walls are treated as no slip stationary wall. Turbulent intensity and turbulent viscosity ratio for velocity inlet and pressure outlet are according to values calculated in Table 5 and 7. Time step size has been calculated in previous study by using equations (3.11) (3.12) (3.13). Thus, the value is adopted. Value of $m = 2^\circ$ is chosen for higher accuracy.

$$\text{Total number of degrees by which domain is rotated per time step, } n = \frac{N \times 360}{60} \quad (3.11)$$

$$\text{Length of each time step in seconds, } t = \frac{m}{n} \quad (3.12)$$

$$\text{Total time in seconds, } T = \frac{\text{Number of rotations} \times 360 \times t}{m} \quad (3.13)$$

First order solution methods are used for first 50 time steps and changed to second order for the rest time steps. Time step size used is 0.0006s. Total number of time steps simulated is 3000.

3.3.5 SOLUTION CONVERGENCE

Convergence study in Fluent is performed to ensure solution achieved uniformity. Solution is considered converged if all discrete conservation equations in each cell obeyed specified tolerance or if the solution no longer changes with subsequent iterations. In addition, overall mass, momentum, energy, and scalar balances must also be achieved. Convergence can be monitored by using residual history or other quantitative convergence. There are four types of convergence criterion in residual monitor which are absolute, relative, relative or absolute, and none. By using absolute criterion, residual of an equation at each iteration is compared with user-specified value. Equation is considered converged for a time step if the residual is less than user-specified value. By using relative criterion, residual of an equation at each iteration of a time step is compared with residual at the beginning of the time step. Equation is considered converged for a time step if the ratio between the two residuals is less than user-specified value. By using relative of absolute criterion, equation is considered converged for a time step if either criterion is met.

In current study, SST turbulence model is used to perform pressure-based, transient simulation by using CFD commercial software, ANSYS Fluent. SST model solves $k-\omega$ transport equation coupled with two other transport equations, one for intermittency and the other for transition onset criteria in terms of momentum thickness Reynolds number. In this study, solution convergence is monitored through scaled residual of 7 equations which are continuity, x-velocity, y-velocity, k, omega, intermittency, and momentum thickness Reynolds number equations. Absolute convergence criterion is used with user-specified value of 0.001 for all equations. Other than that, convergence of physical quantities such as drag coefficient, lift coefficient, and moment coefficient are also monitored to support the scaled residual findings. Figure 3.20 to Figure 3.31 show convergence monitors for all rotors at three inlet velocities; 6.0 m/s, 8.23 m/s, and 10.17 m/s.

Figure 3.20(a) to Figure 3.22(a) show that scaled residuals for continuity and omega equations of conventional rotor are above user-specified criterion which are 0.1 and 0.01 respectively while other equations achieved convergence with scaled residuals of 0.001 or below. Physical quantities such as moment coefficient and lift coefficient are considered converged based on the uniformity against flow time. Drag coefficient plotted against flow time has slight difference throughout iterations up to 0.2 between flow time 0.3s to 1.8s for all inlet velocities. Therefore, it can be concluded that equations for conventional rotors for all three different inlet velocities achieved solution convergence at each iteration for a time step.

Figure 3.23(a) to Figure 3.25(a) show that scaled residuals for continuity equation of Design 1 rotor is above user-specified criterion which is around 0.1 for all three inlet velocities while other equations achieved convergence with scaled residuals around 0.001 or below. Moment coefficient and lift coefficient for Design 1 rotor at three different inlet velocities are considered converged based on uniformity against flow time while drag coefficient plotted against flow time has difference throughout iterations up to 0.5 between flow time 0.3s to 1.8s for all inlet velocities. Thus, it also can be concluded that equations for Design 1 rotor for all inlet velocities achieved solution convergence at each iteration for a time step.

Figure 3.26(a) to Figure 3.28(a) show that scaled residuals for Design 2 rotor have similar pattern to scaled residuals for Design 1 rotor. However, scaled residuals for k and omega equations at $V = 10.17$ m/s exceed user-specified, 0.001 by 0.0055. Other equations converged with scaled residuals around 0.001 or below. Moment coefficient for all inlet velocities is converged based on uniformity against flow time. Lift coefficient against flow time for Design 2 at $V = 6.0$ m/s has slight difference throughout iterations up to 0.25 between flow time 0.3s to 1.8s. Lift coefficient for other inlet velocities are converged. Drag coefficient plotted against flow time for all three inlet velocities show unequal values from flow time 0.3s to 1.8s but the pattern are repeated which shows uniformity. The biggest difference between drag coefficient values throughout flow time is obtained at $V = 10.17$ which is round 0.75. It can be concluded that equations for Design 2 rotor for all inlet velocities achieved solution convergence at each iteration for a time step.

Figure 3.29(a) to Figure 3.31(a) show scaled residuals for Design 3 rotor at three different inlet velocities. It is shown that scaled residual for continuity equation is above user-specified criterion which is around 0.1 while scaled residuals for other equations are around 0.001 or below for all inlet velocities. Moment coefficient plotted against flow time for all inlet velocities show unequal values obtained throughout iterations. However, uniformity is achieved due to repeated pattern of the lines. The same scenario occurred for drag coefficient plotted against flow time for all inlet velocities especially from flow time 0.8s to 1.8s. Lift coefficient monitor for all inlet velocities shows that uniformity is not achieved with difference ranging from 0.75 to 1.5. Equations for Design 3 rotor for all inlet velocities are assumed converged at each iteration for a time step based on supported data by scaled residuals, moment coefficient, and drag coefficient.



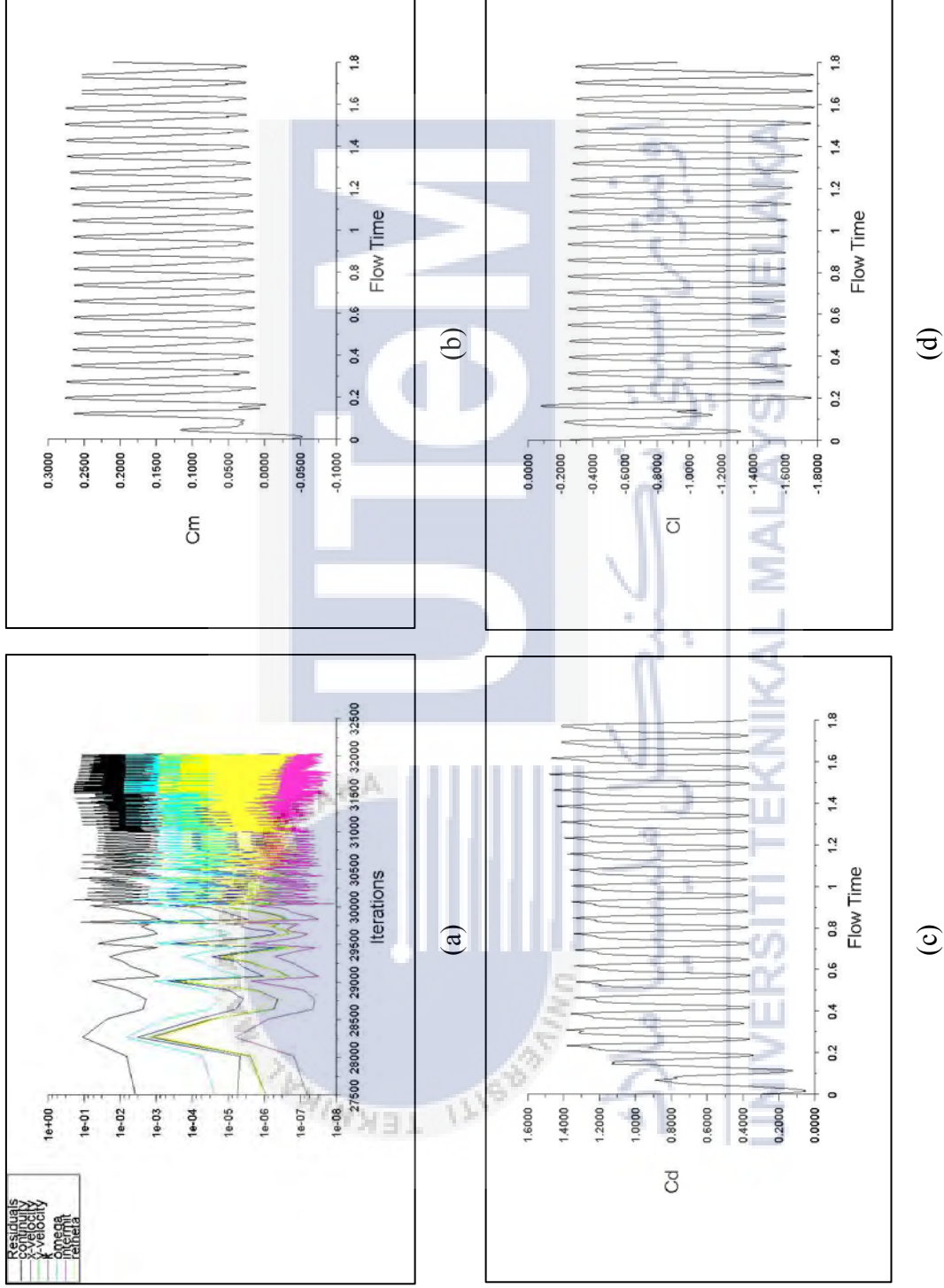


Figure 3.20 Monitors for Conventional rotor at $V = 6.0$ m/s (a) scaled residual (b) moment coefficient (c) drag coefficient (d) lift coefficient

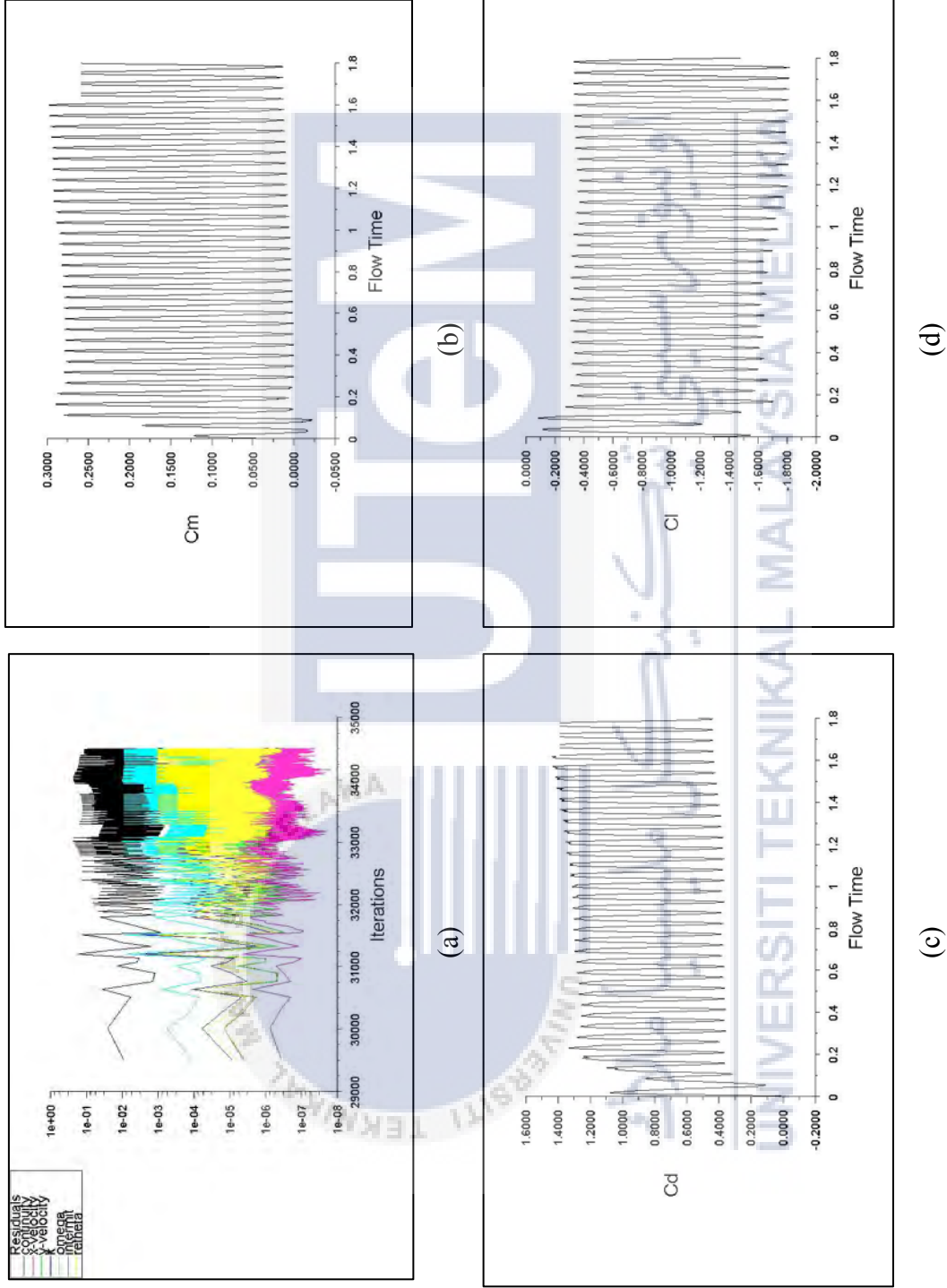


Figure 3.21 Monitors for Conventional rotor at $V = 8.23$ m/s (a) scaled residual (b) moment coefficient (c) drag coefficient (d) lift coefficient

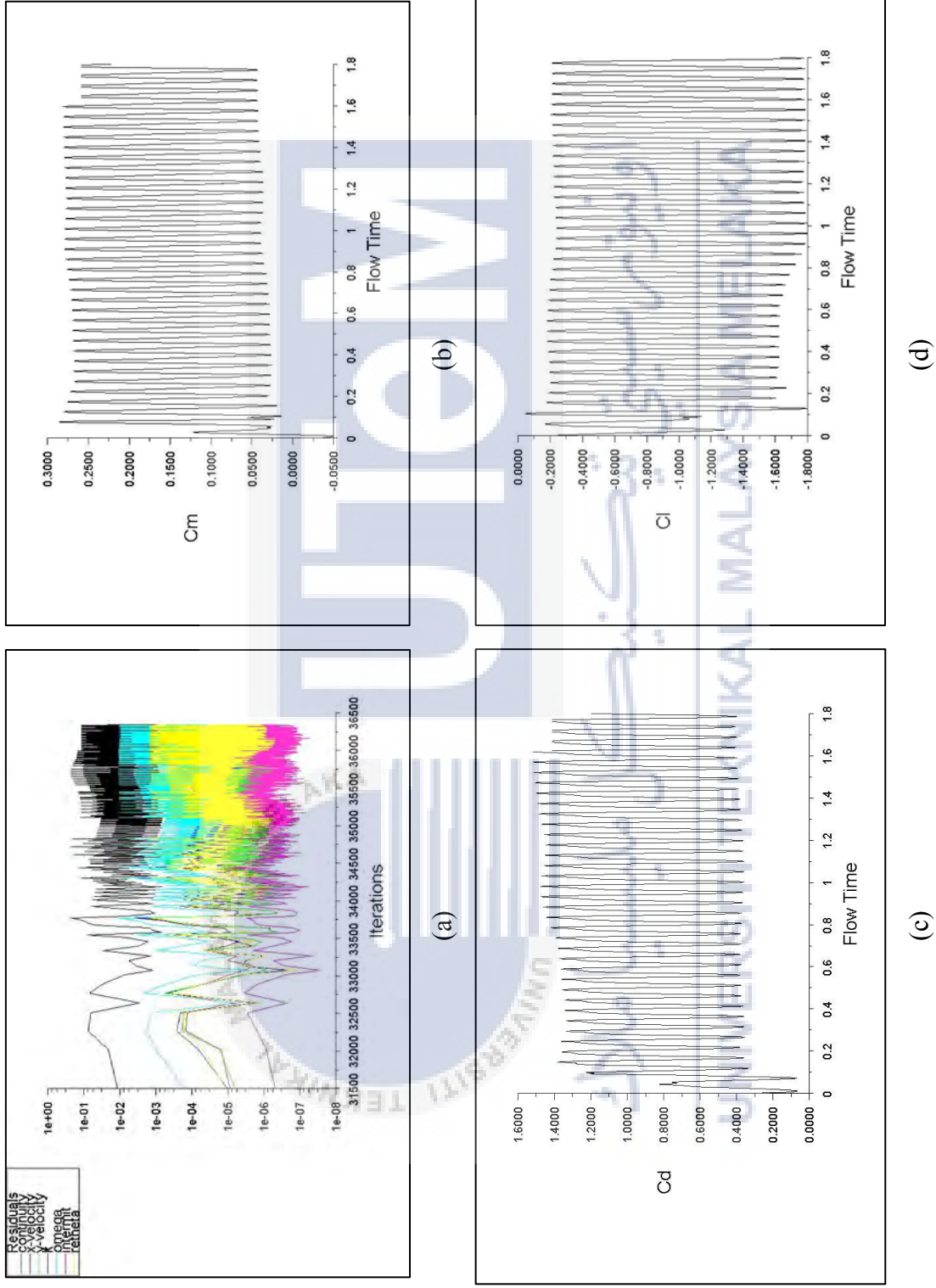


Figure 3.22 Monitors for Conventional rotor at $V = 10.17$ m/s (a) scaled residual (b) moment coefficient (c) drag coefficient (d) lift coefficient

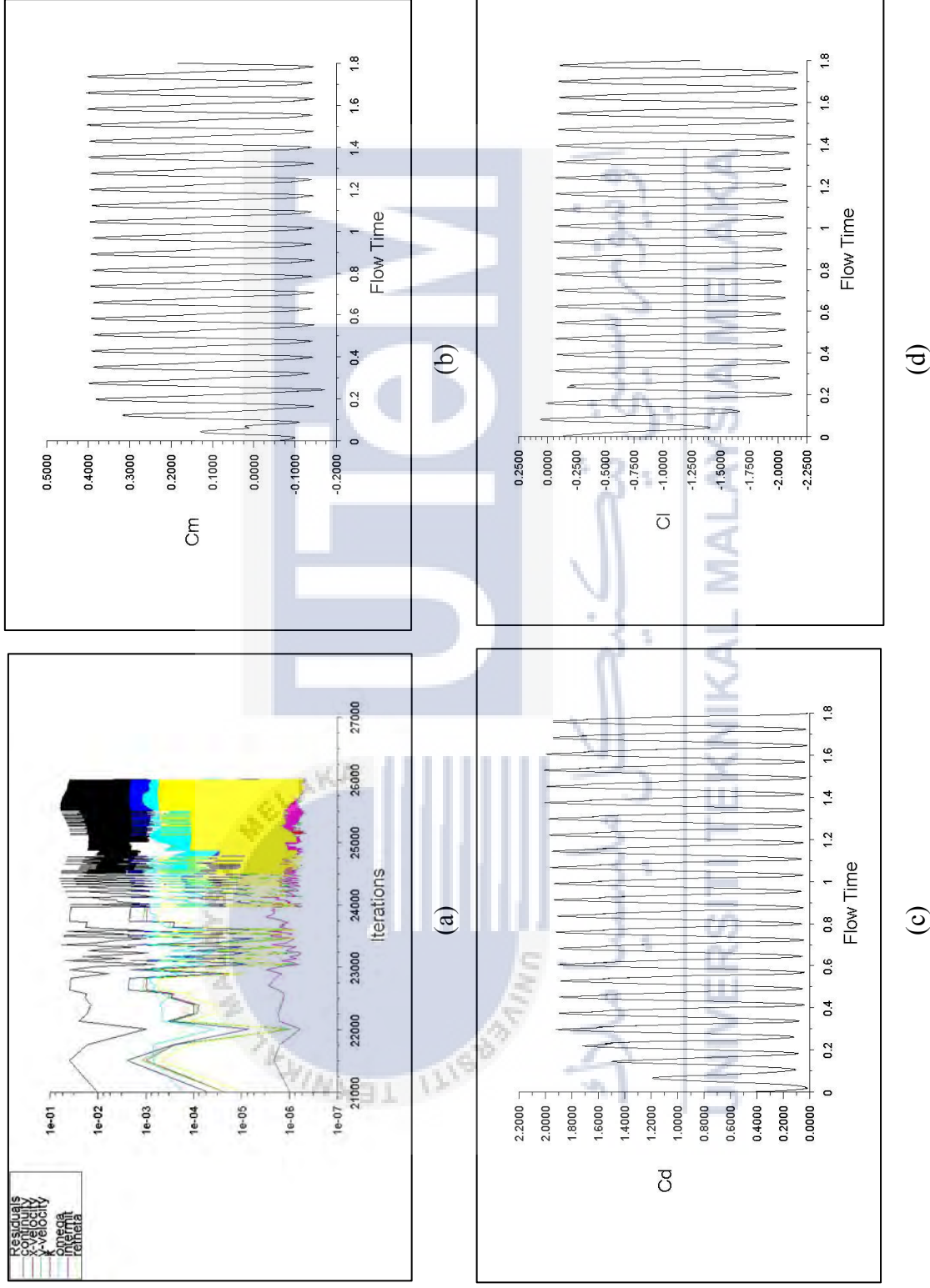


Figure 3.23 Monitors for Design I rotor at $V = 6.0$ m/s (a) scaled residual (b) moment coefficient (c) drag coefficient (d) lift coefficient

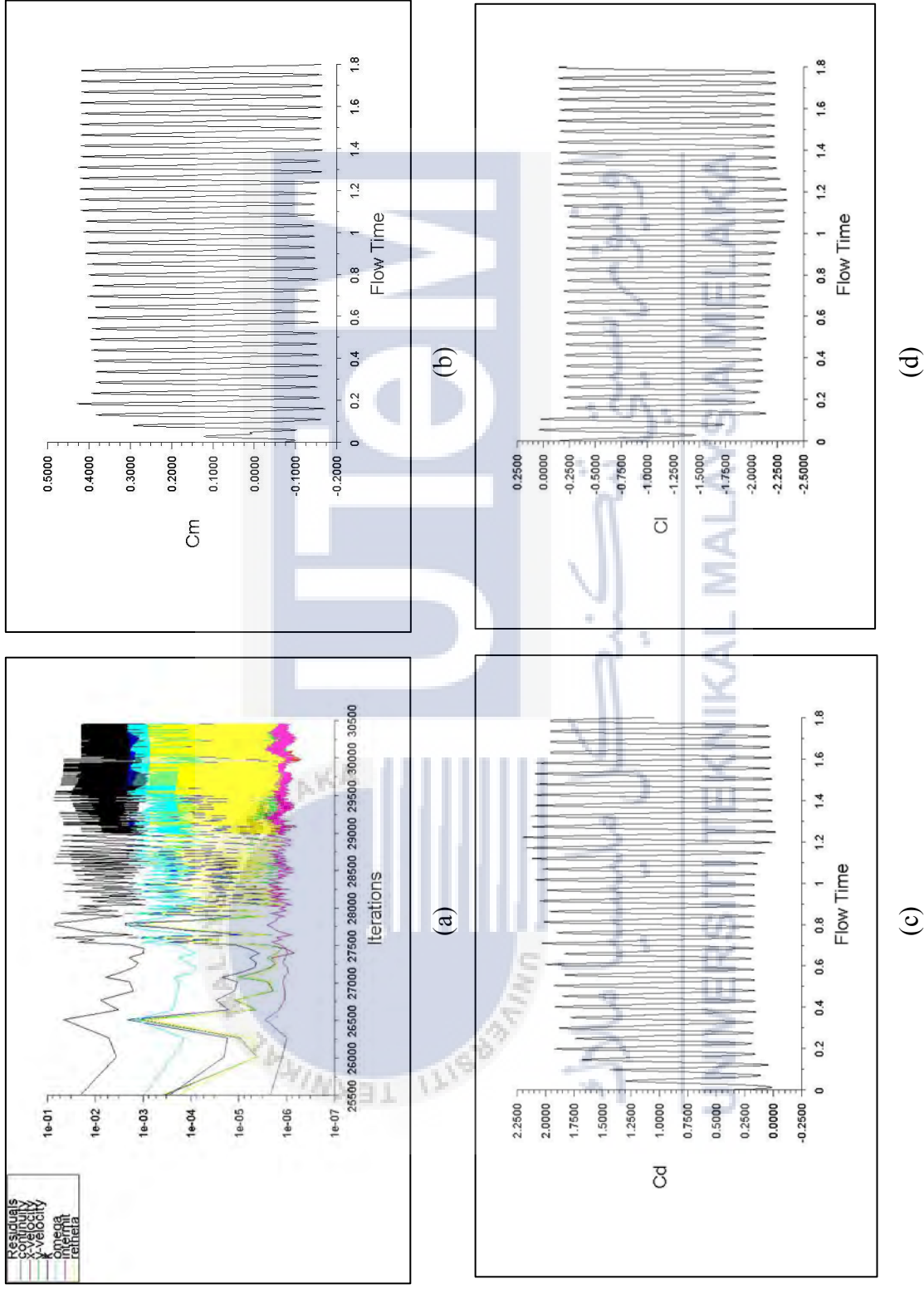


Figure 3.24 Monitors for Design 1 rotor at $V = 8.23$ m/s (a) scaled residual (b) moment coefficient (c) drag coefficient (d) lift coefficient

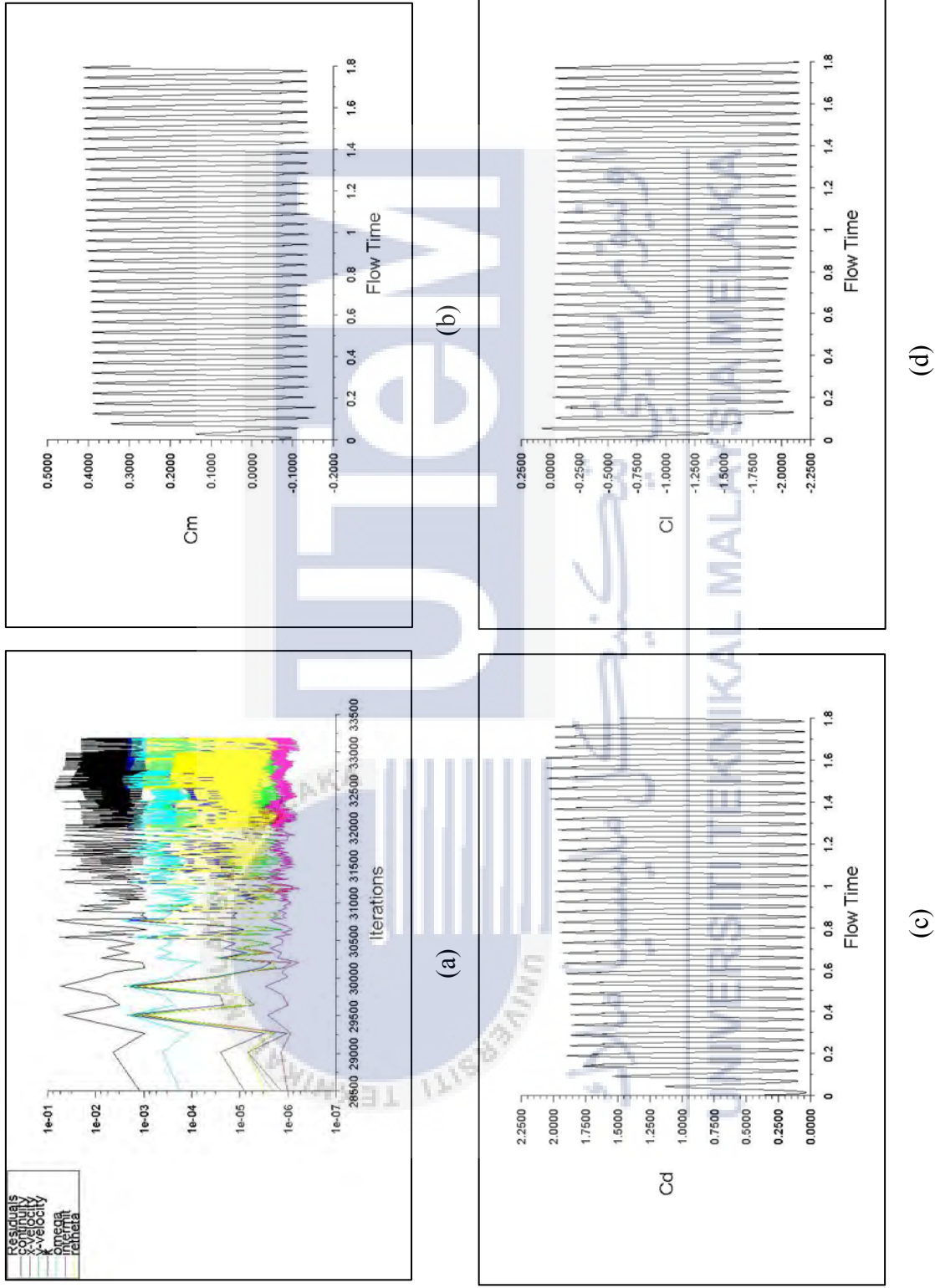


Figure 3.25 Monitors for Design 1 rotor at $V = 10.17$ m/s (a) scaled residual (b) moment coefficient (c) drag coefficient (d) lift coefficient

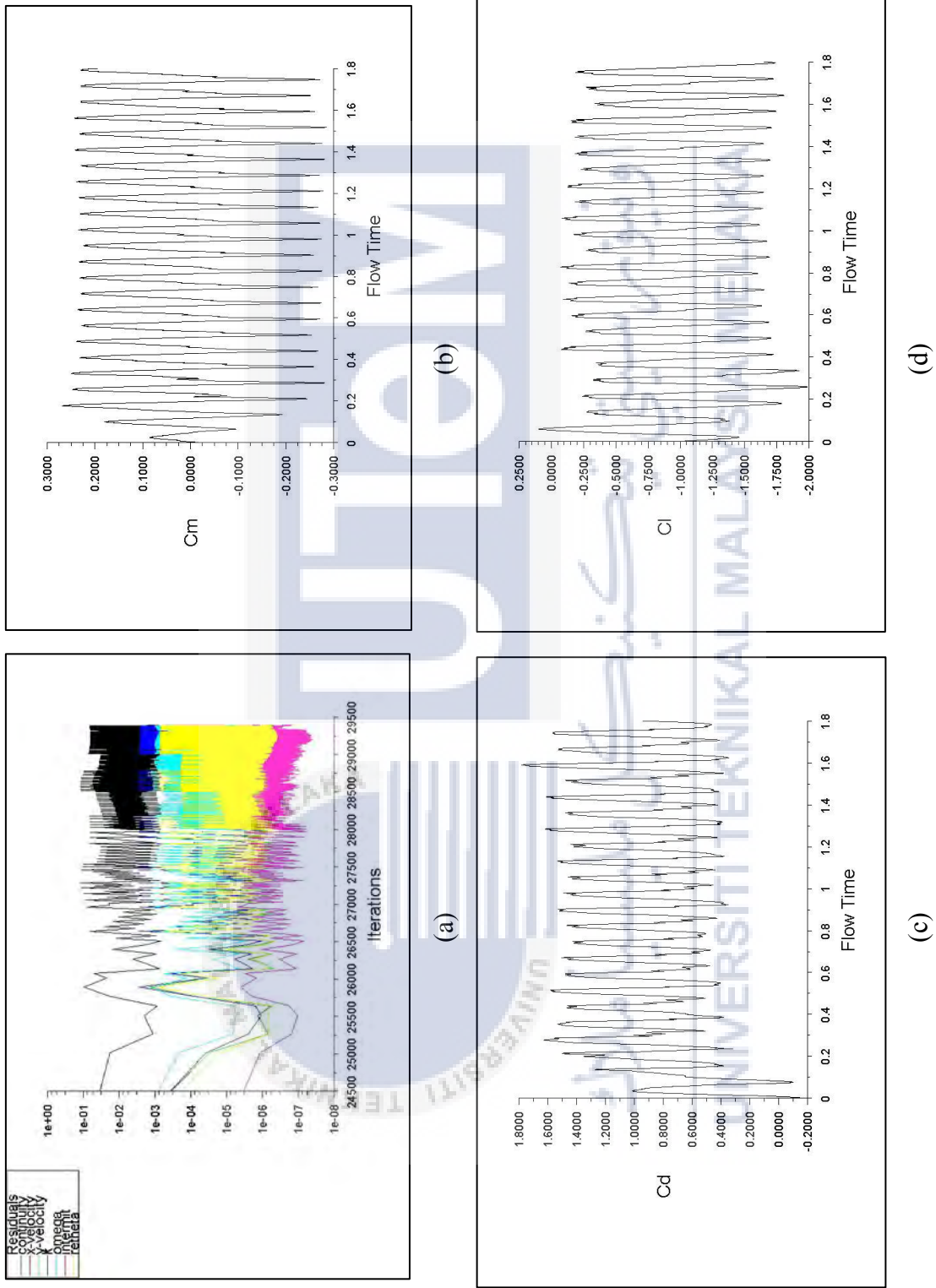


Figure 3.26 Monitors for Design 2 rotor at $V = 6.0$ m/s (a) scaled residual (b) moment coefficient (c) drag coefficient (d) lift coefficient

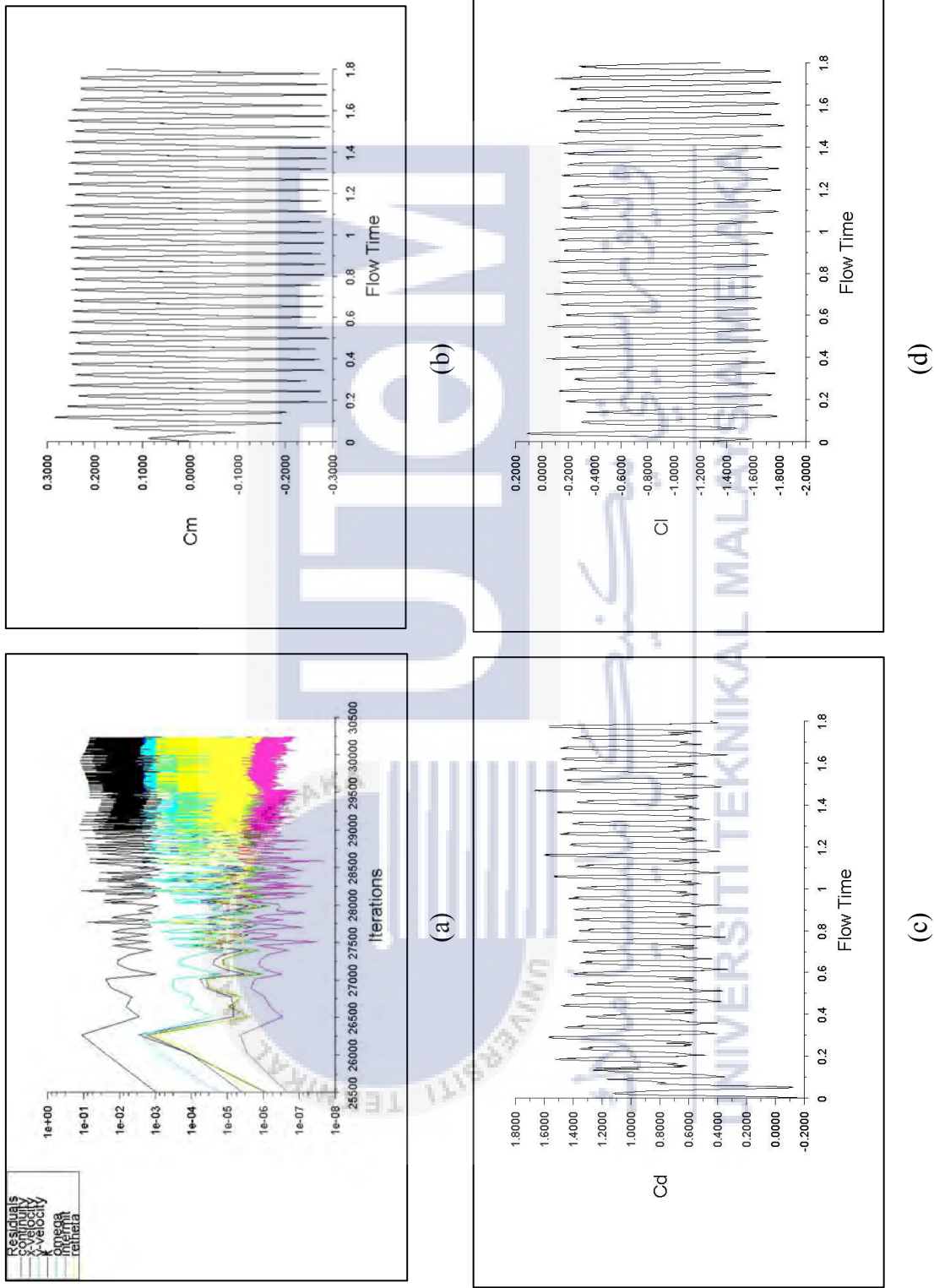


Figure 3.27 Monitors for Design 2 rotor at $V = 8.23$ m/s (a) scaled residual (b) moment coefficient (c) drag coefficient (d) lift coefficient

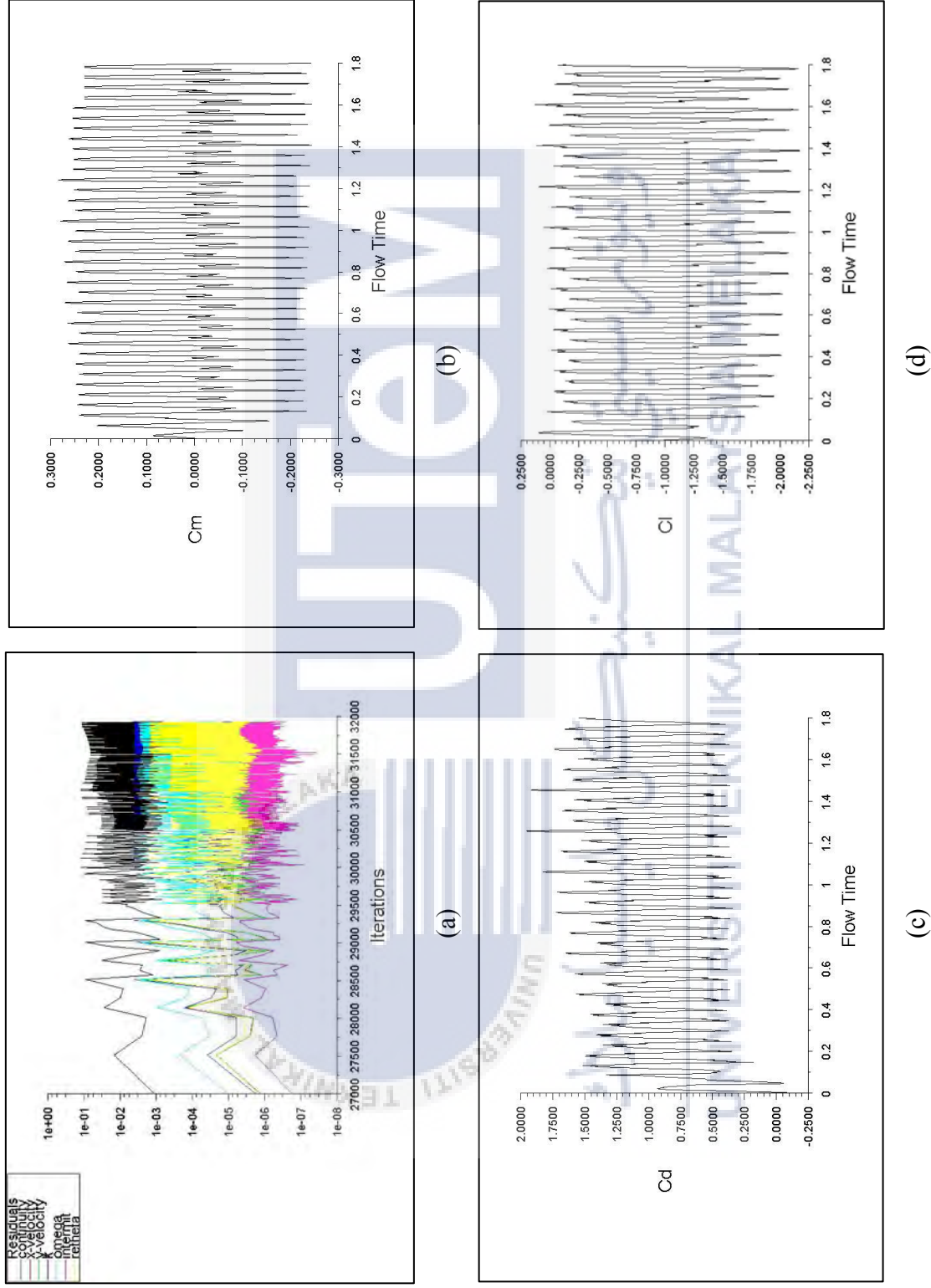


Figure 3.28 Monitors for Design 2 rotor at $V = 10.17$ m/s (a) scaled residual (b) moment coefficient (c) drag coefficient (d) lift coefficient

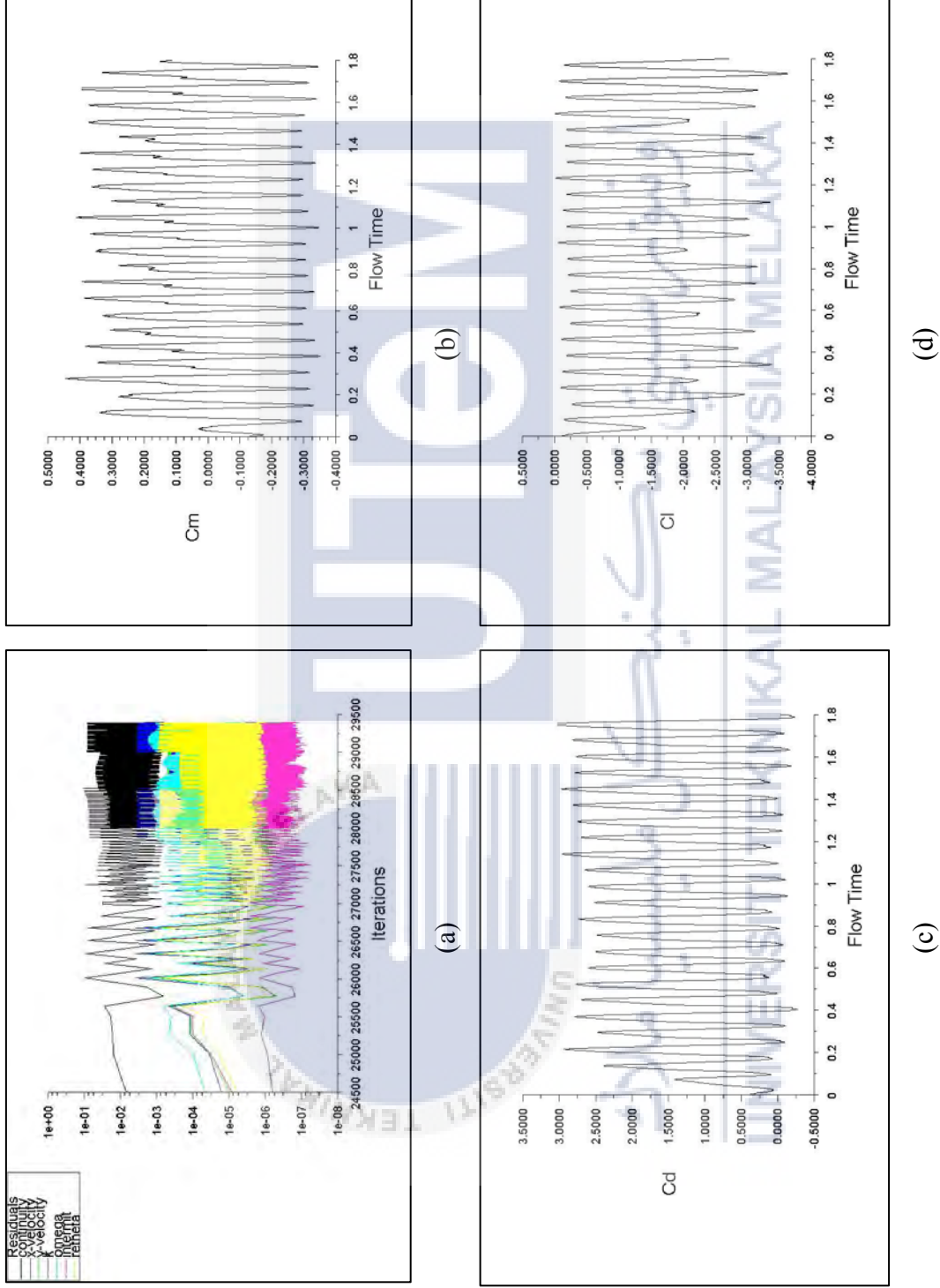


Figure 3.29 Monitors for Design 3 rotor at $V = 6.0$ m/s (a) scaled residual (b) moment coefficient (c) drag coefficient (d) lift coefficient

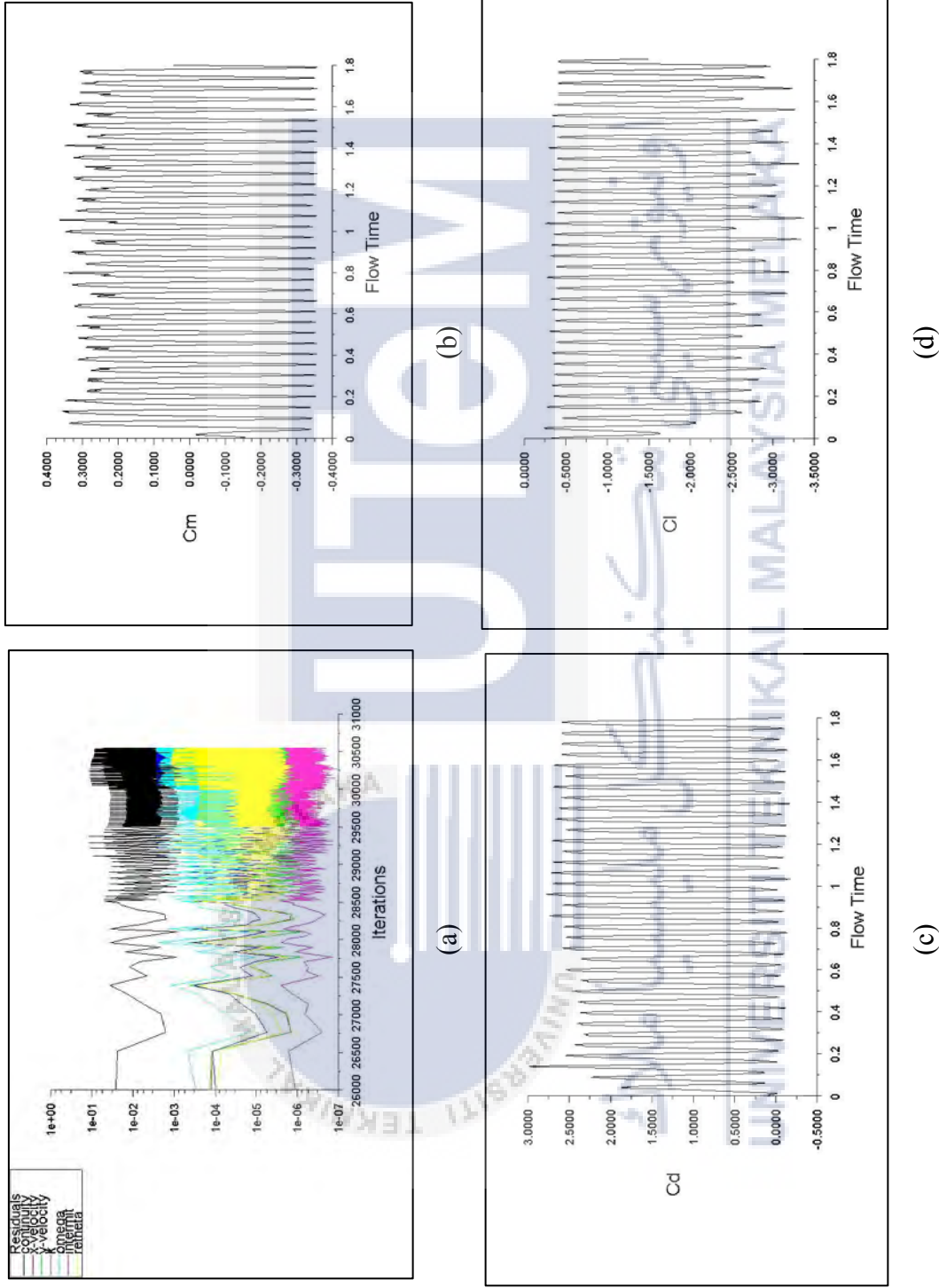


Figure 3.30 Monitors for Design 3 rotor at $V = 8.23$ m/s (a) scaled residual (b) moment coefficient (c) drag coefficient (d) lift coefficient

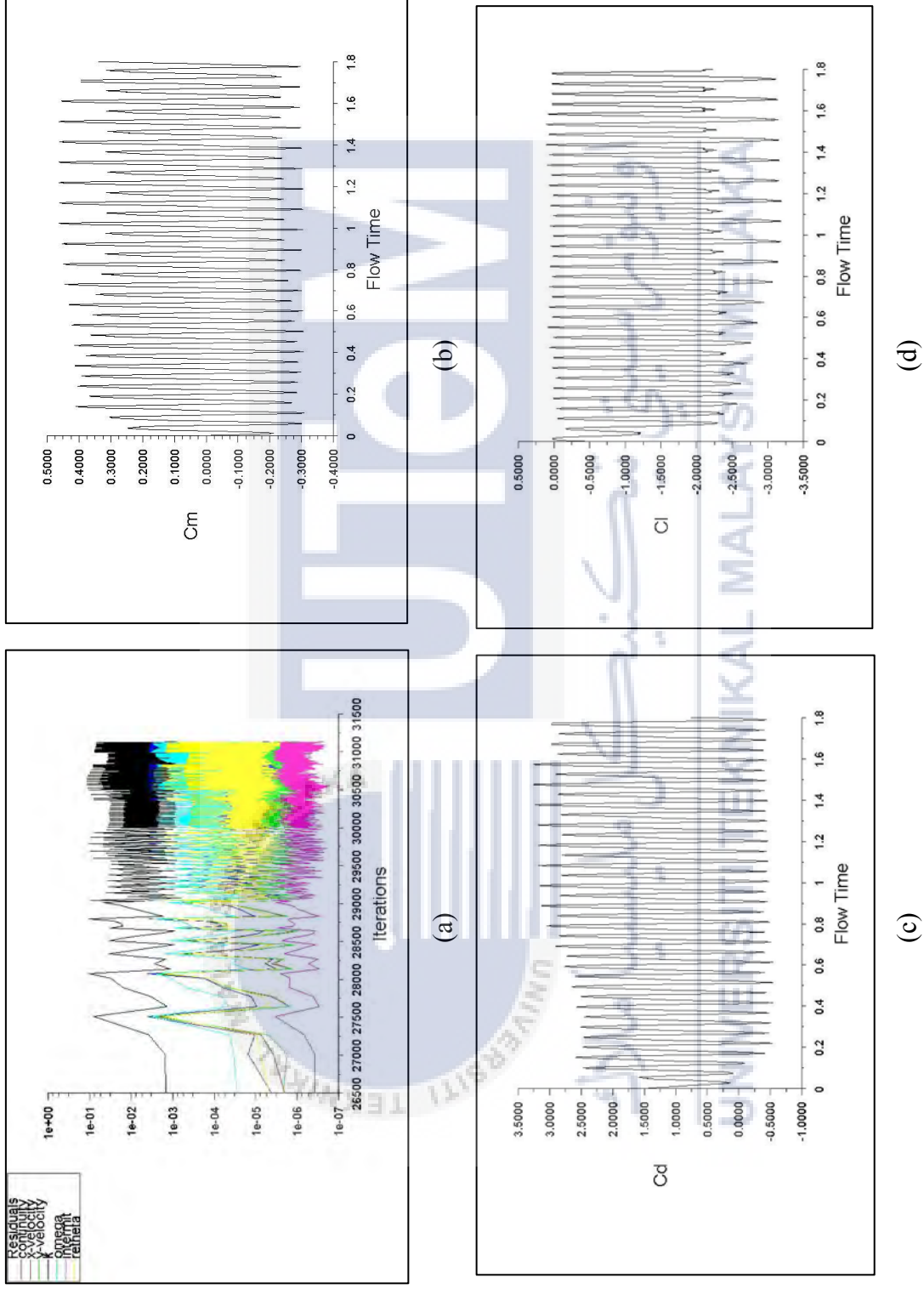


Figure 3.31 Monitors for Design 3 rotor at $V = 10.17$ m/s (a) scaled residual (b) moment coefficient (c) drag coefficient (d) lift coefficient

CHAPTER 4

RESULTS AND DISCUSSION

Performance of Split Savonius rotor depends on mechanical torque, angular velocity of the rotor, projected area of the rotor, air density and air velocity. In current study, the effect of mechanical torque towards rotor performance is focused on by varying the rotor designs. A validation study is performed by comparing torque values from CFD numerical approach with torque values from experimental approach by Saha et al. for three inlet velocities; 6.0, 8.23 and 10.17 ms^{-1} . Validated methods are used to perform comparative study between conventional rotor and new configurations. Three new configurations are made based on conventional Split Savonius rotor by keeping the aspect ratio, overlap ratio and projected area constant for all four configurations.

UNIVERSITI TEKNIKAL MALAYSIA MELAKA

4.1 VALIDATION STUDY

Validation study is performed by comparing torque obtained from CFD numerical approach to Saha et al. experimental approach to achieve a numerical platform for comparative study between conventional rotor and new configured rotor. Torque is calculated based on C_m generated from ANSYS Fluent by using equation 4.1. The values are compared to torque per height obtained by Saha et al. for inlet velocities of 6.0, 8.23 and 10.17 m/s. Percentage difference between both values are calculated by using equation 4.2. It is shown that torque obtained for inlet velocity 6.0 m/s is more similar to torque obtained by Saha et al. of the same inlet velocity with percentage difference of 35.16%. Percentage difference for torque values obtained for inlet velocity 8.23 m/s is the biggest among three which is 102.96%. However, according to percentage difference obtained

from Sonu Sharma et al. for validation study between CFX 3D numerical approach and Saha et al. experimental approach, the percentage difference is considerable (Sonu Sharma, 2016).

$$\text{Torque, } T = \frac{1}{2} \times C_m \times \rho \times V^2 \times A \times L \quad (4.1)$$

$$\text{Percentage difference} = \frac{|V_1 - V_2|}{\frac{(V_1 + V_2)}{2}} \times 100\% \quad (4.2)$$

Table 10 Percentage difference between torque CFD and torque U.K Saha et al.

Inlet Velocity (m/s)	C_m	Torque Conventional per height (N)	Torque Saha et al. per height (N)	Percentage difference (%)
6.0	0.246	0.0377	0.0538	35.19
8.23	0.233	0.0672	0.2098	102.96
10.17	0.248	0.1092	0.2295	71.0363

4.2 COMPARATIVE STUDY

The main objective of this study is to propose a new configured Split Savonius rotor which has higher torque compared to the conventional Split Savonius rotor. In order to achieve objective stated, a comparative study is conducted by using commercial CFD software, ANSYS Fluent. Three new configurations are created by keeping end plate diameter, rotor diameter, overlap and thickness of rotor the same to the conventional rotor for comparative study. All four rotors are simulated in the same condition by using air at 25°C as the working fluid. Split Savonius rotor consists of two blades fixed in S shape with overlap in between. Forces are generated on the rotor walls when kinetic energy of the working fluid acted on the walls. These forces generated torques, positive and negative. Positive torque is created if torque generated by advancing blade is higher than torque generated by returning blade. This torque is useful in increasing COP of the rotor. In current study, torque is calculated by considering C_m obtained by numerical analysis

approach. Figure 4.2 shows torque per height calculated for all rotors. It is clear that torque values for all designs increase with inlet velocity supporting the theoretical relationship. Result for the comparative study is documented as shown in Figure 4.1 and 4.2. Performance improvement of Split Savonius rotor is measured by comparing its COP. Thus, COP and the percentage change in COP for each rotor are calculated and documented in Figure 4.3 and Table 11 respectively. The result shows that performance improvement only occurs for Design 1 ranging from 0.78% to 1.33%. Other designs show negative values which indicate performance drop.

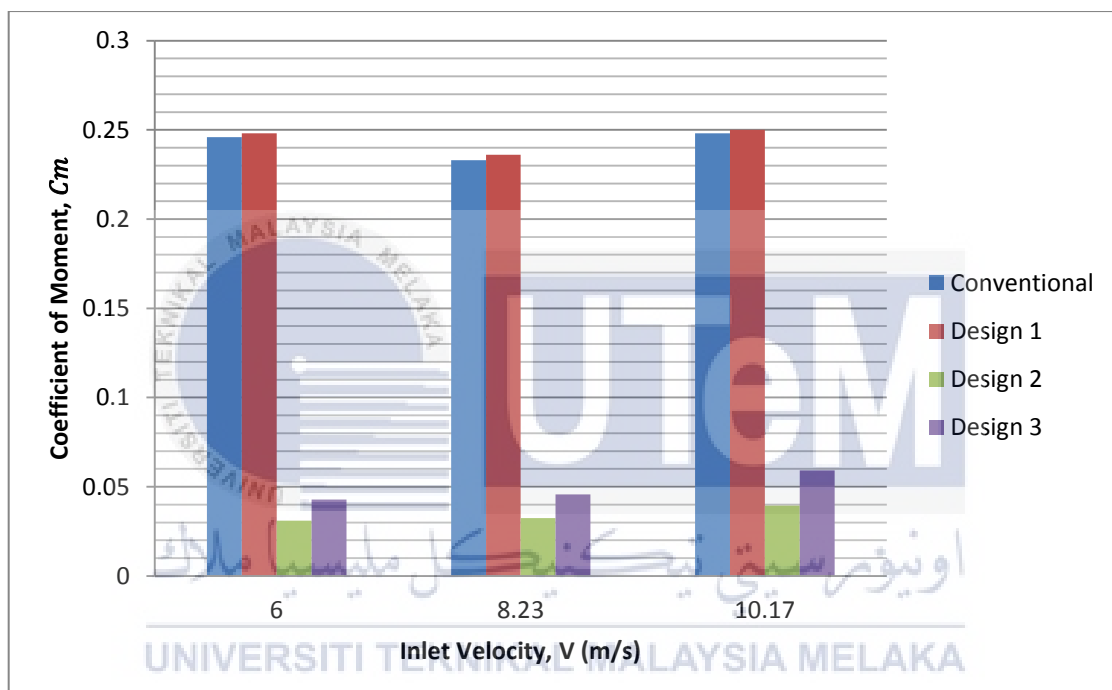


Figure 4.1 Coefficient of moment against inlet velocity for conventional rotor, design 1, design 2 and design 3

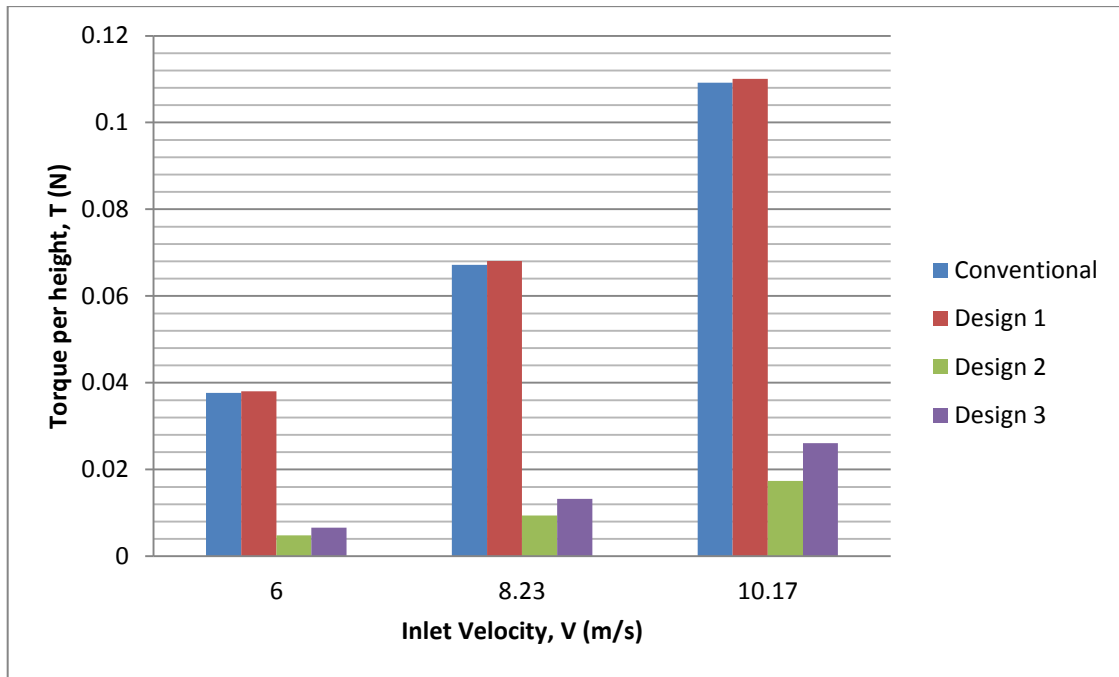


Figure 4.2 Torque per height against inlet velocity for conventional rotor, design 1, design 2 and design 3

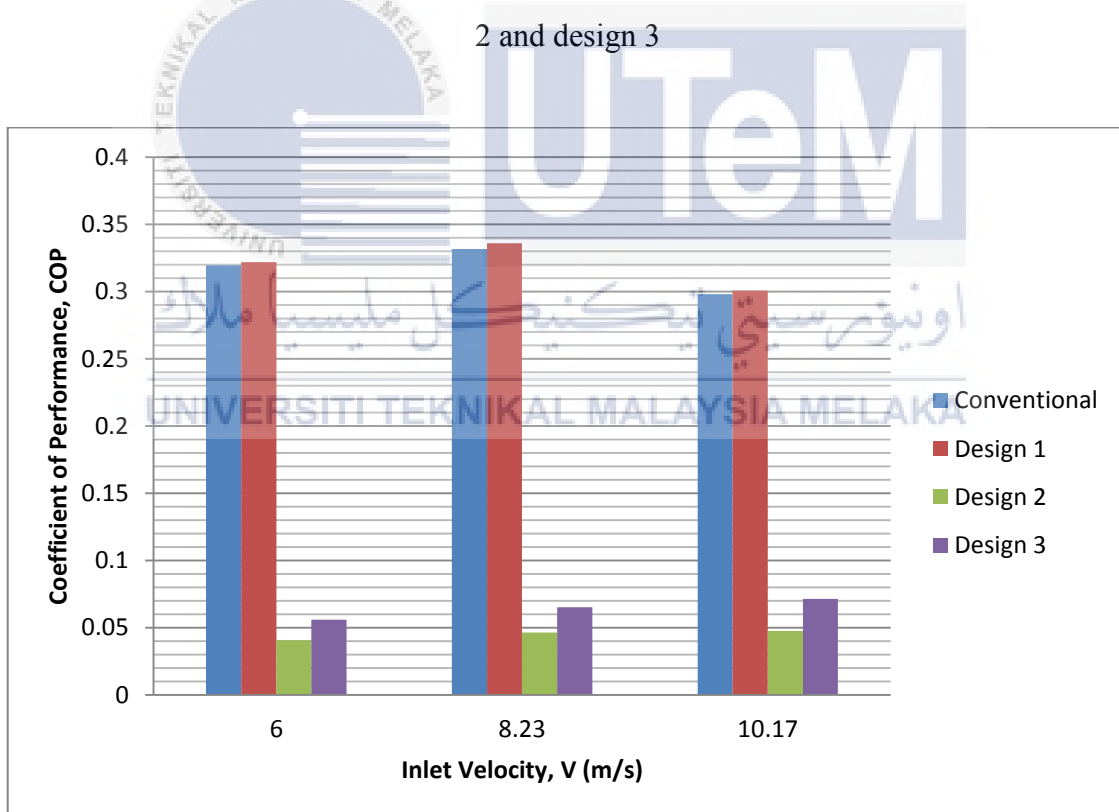


Figure 4.3 Coefficient of performance against inlet velocity for conventional rotor, design 1, design 2 and design 3

Table 11 Percentage change in COP between conventional rotor, design 1, design 2 and design 3

Inlet Velocity, V (m/s)	Percentage change in COP Design 1 (%)	Percentage change in COP Design 2 (%)	Percentage change in COP Design 3 (%)
6.0	0.78	-87.26	-82.50
8.23	1.33	-86.0	-80.36
10.17	0.84	-84.07	-76.08



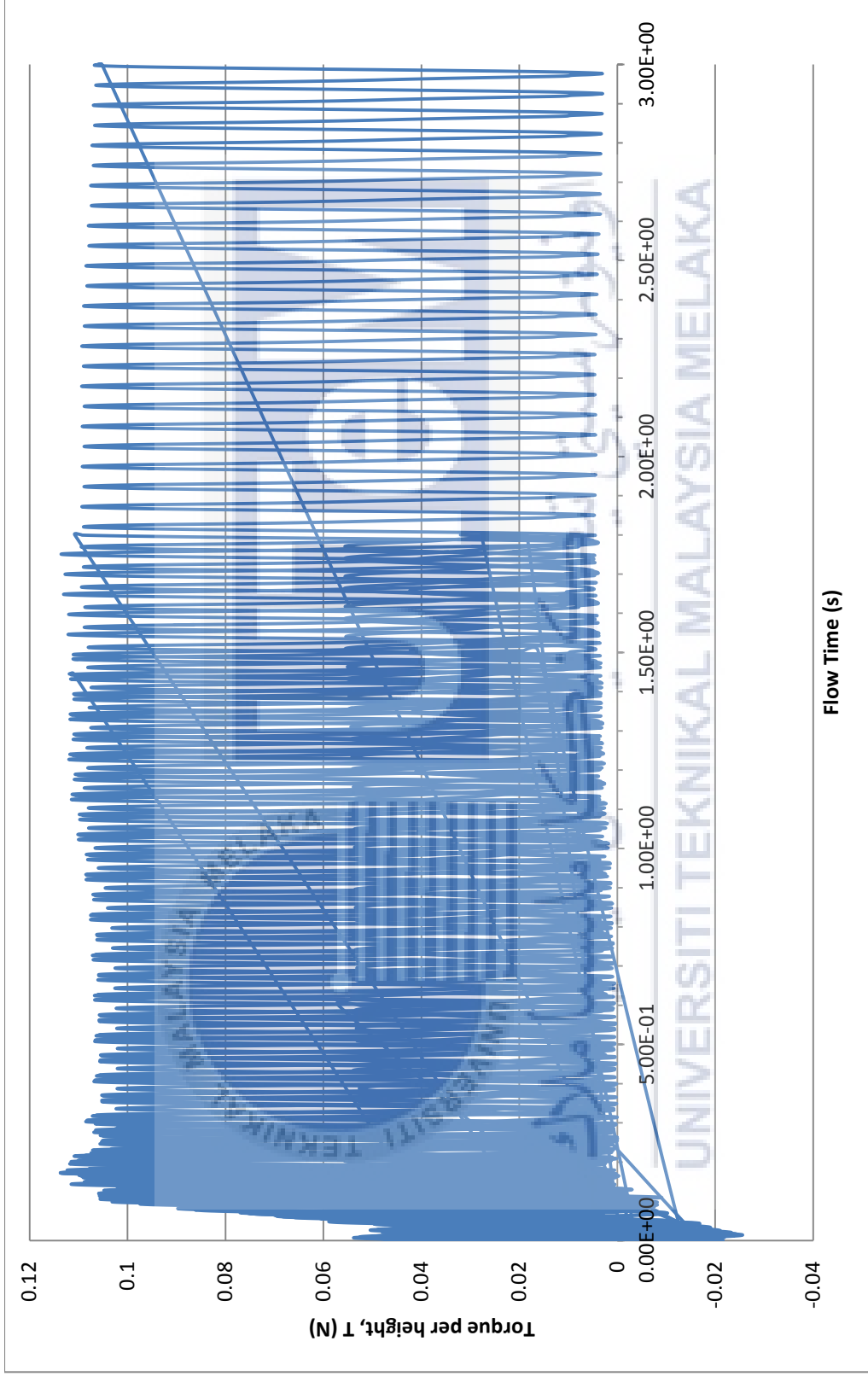


Figure 4.4 Variation of torque of conventional rotor with time value for $V = 6.0$ m/s

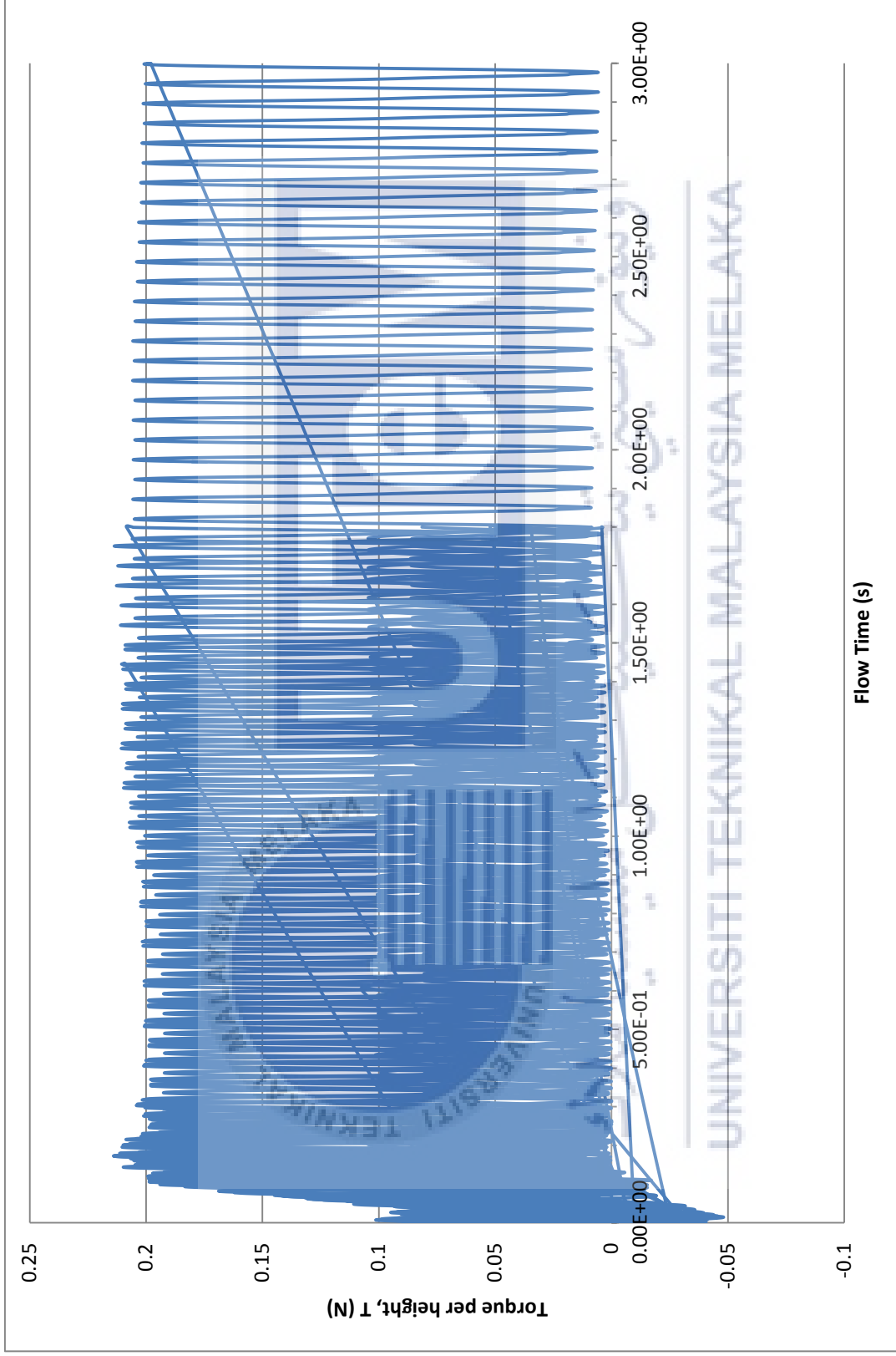


Figure 4.5 Variation of torque of conventional rotor with time value for $V = 8.23$ m/s

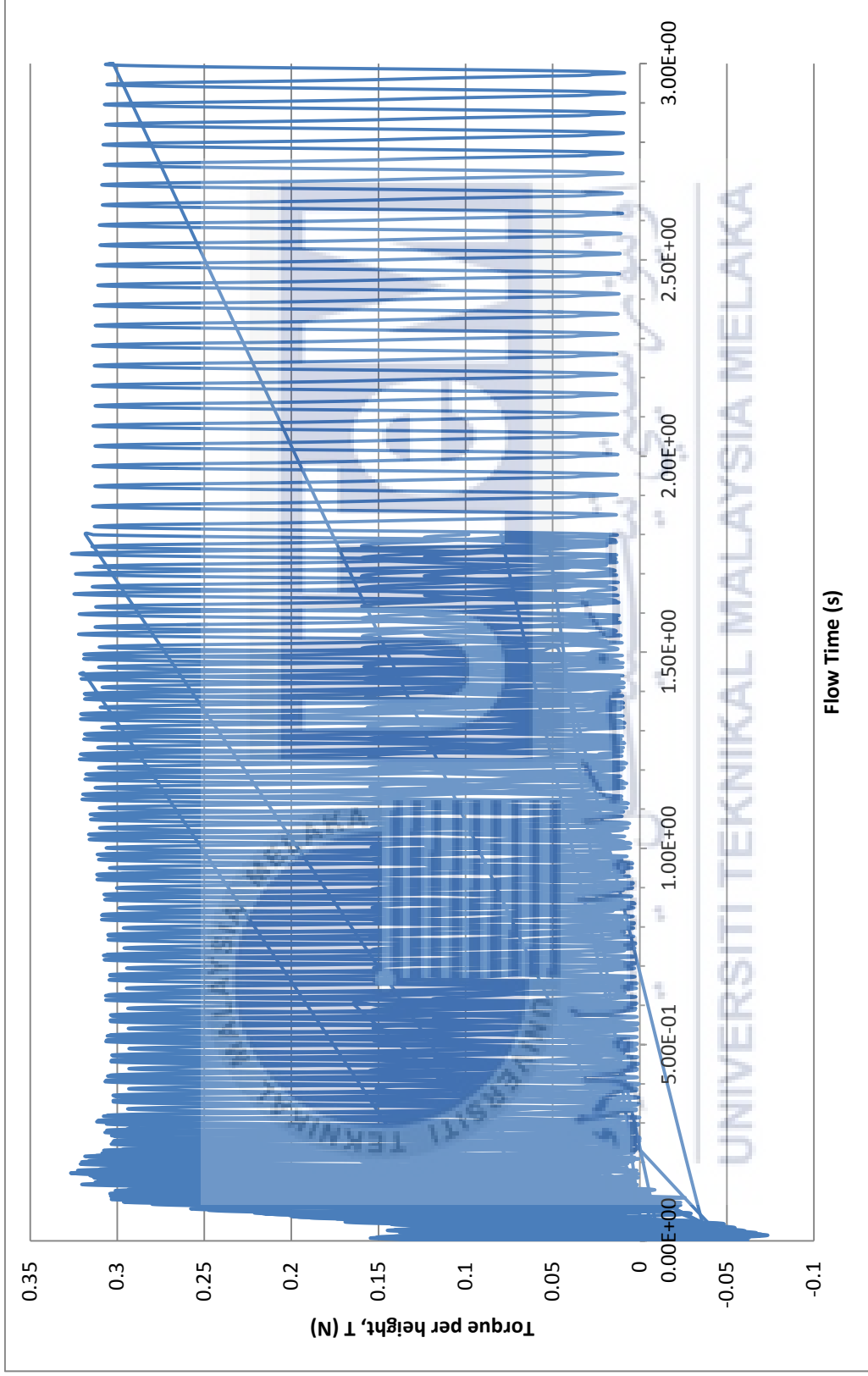


Figure 4.6 Variation of torque of conventional rotor with time value for $V = 10.17$ m/s

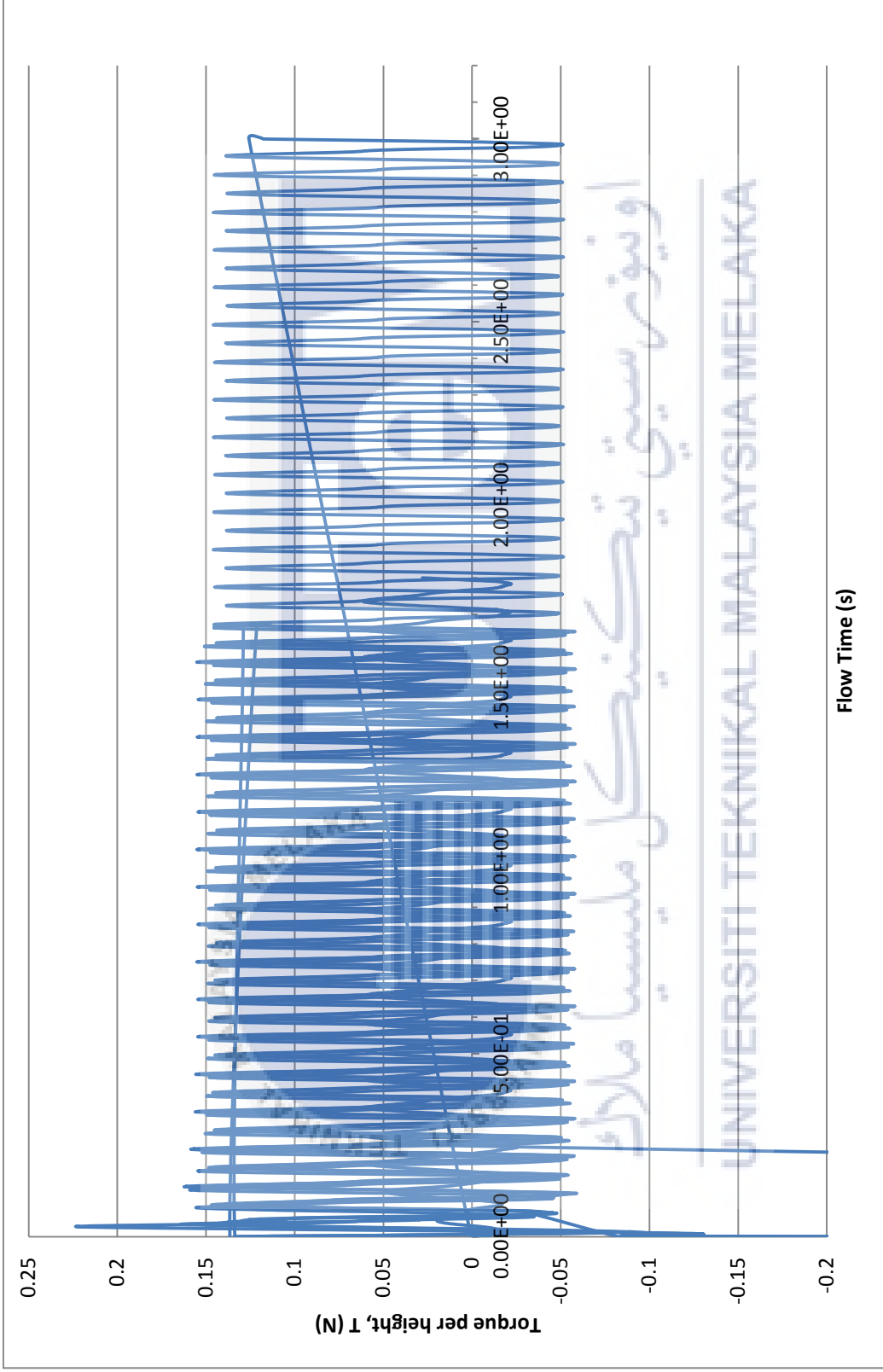


Figure 4.7 Variation of torque of Design 1 rotor with time value for $V = 6.0$ m/s

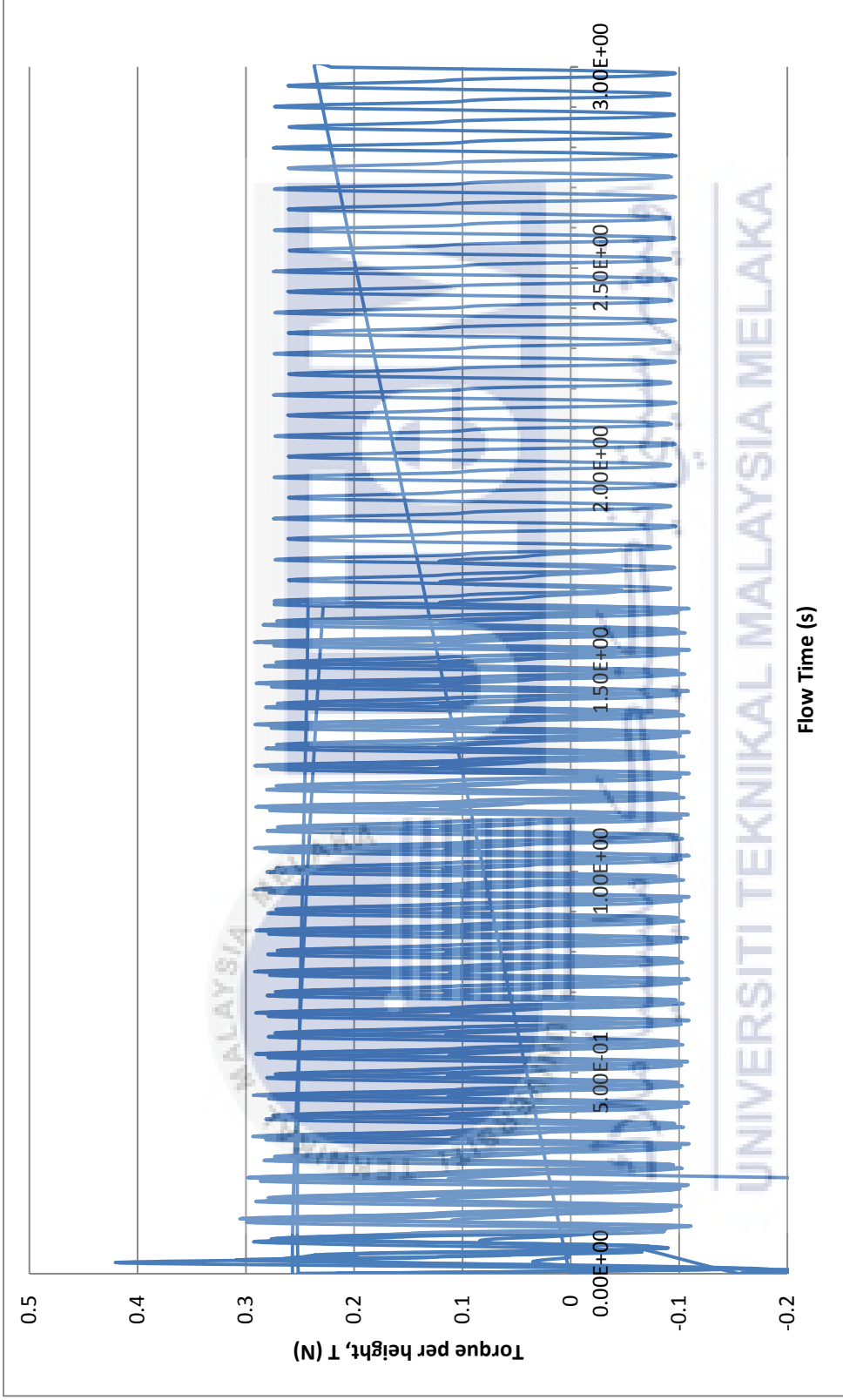


Figure 4.8 Variation of torque of Design 1 rotor with time value for $V = 8.23$ m/s

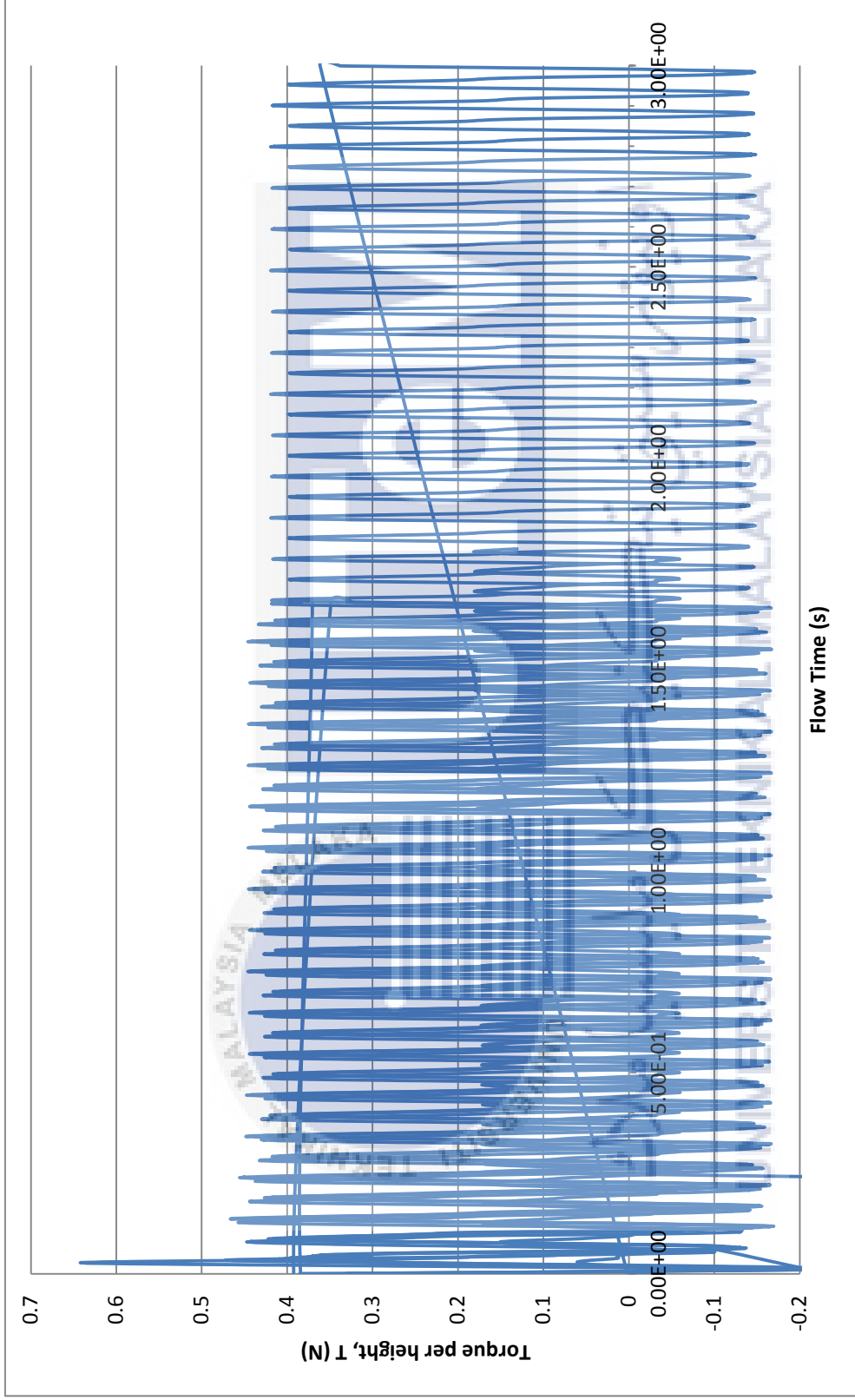


Figure 4.9 Variation of torque of Design 1 rotor with time value for $V = 10.17$ m/s

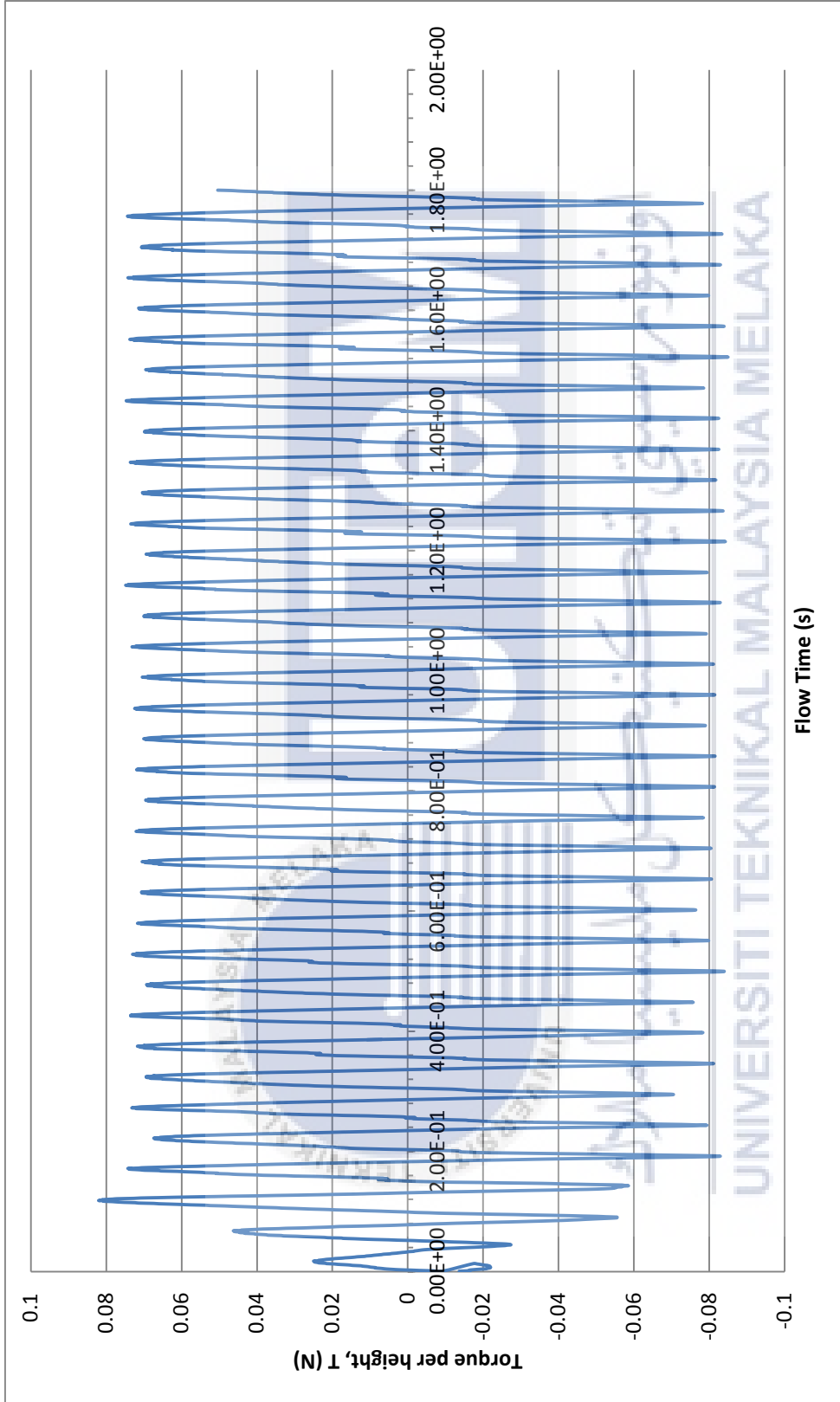


Figure 4.11 Variation of torque of Design 2 rotor with time value for $V = 8.23$ m/s

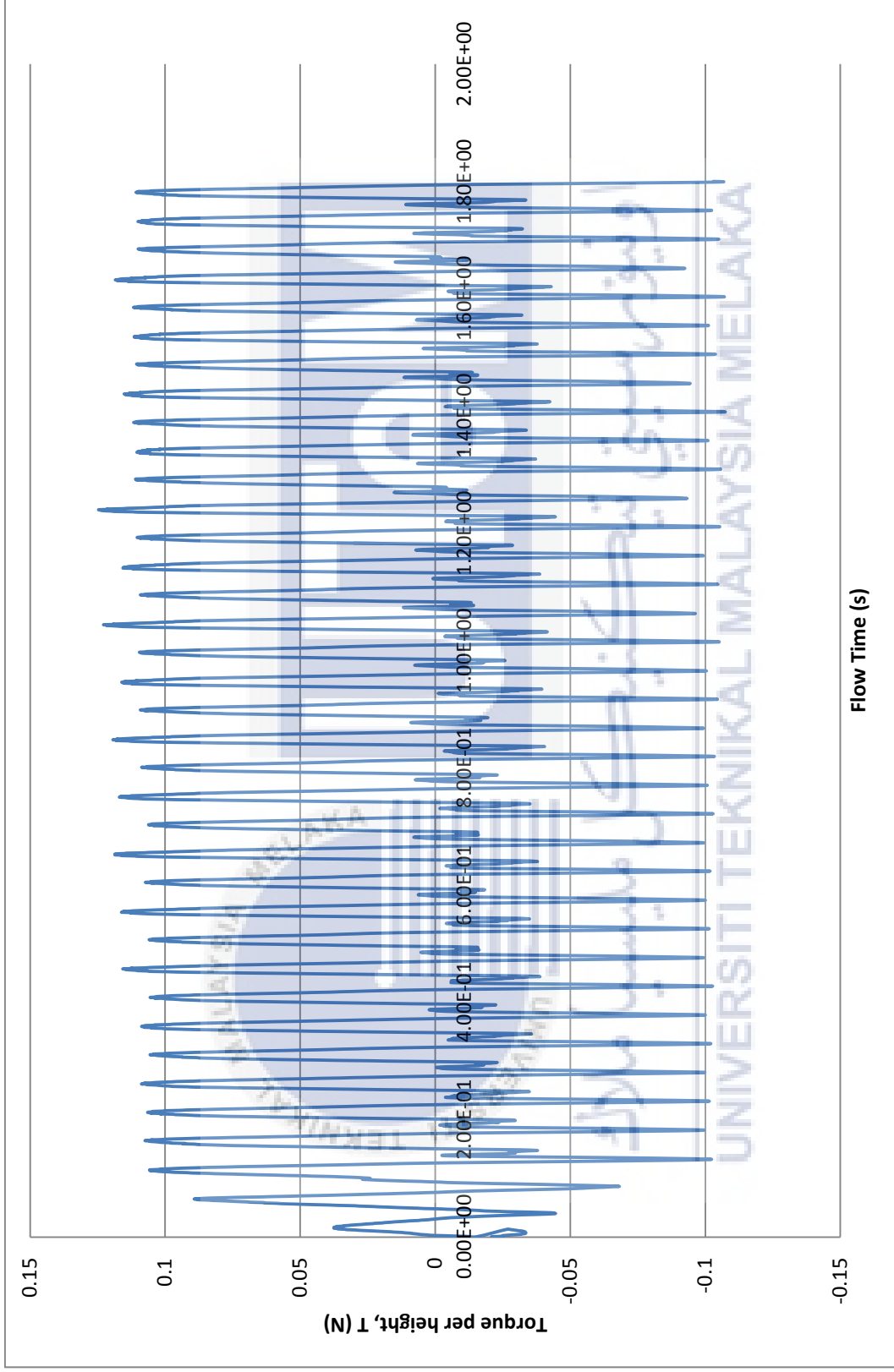


Figure 4.12 Variation of torque of Design 2 rotor with time value for $V = 10.17$ m/s

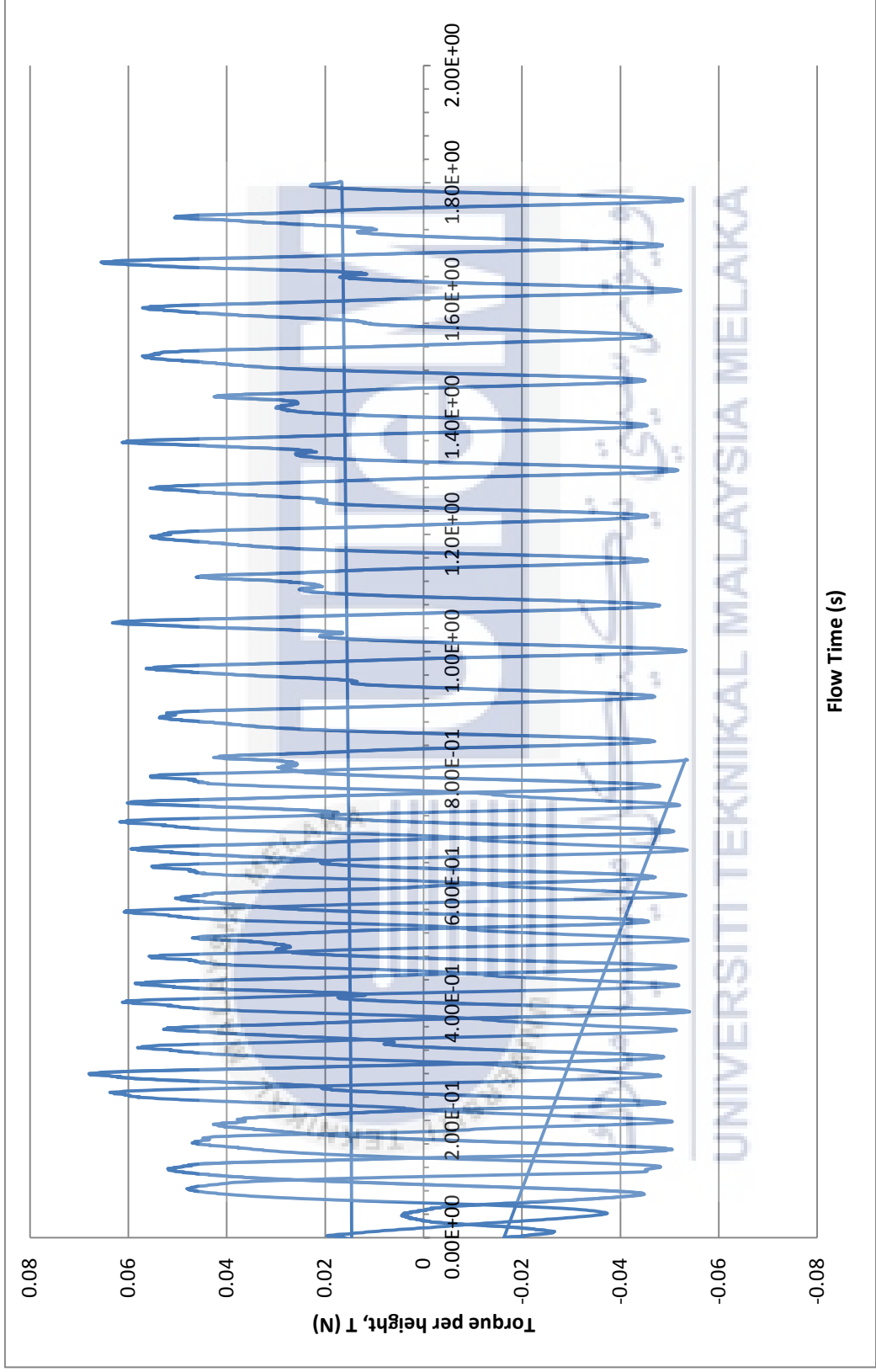


Figure 4.13 Variation of torque of Design 3 rotor with time value for $V = 6.0$ m/s

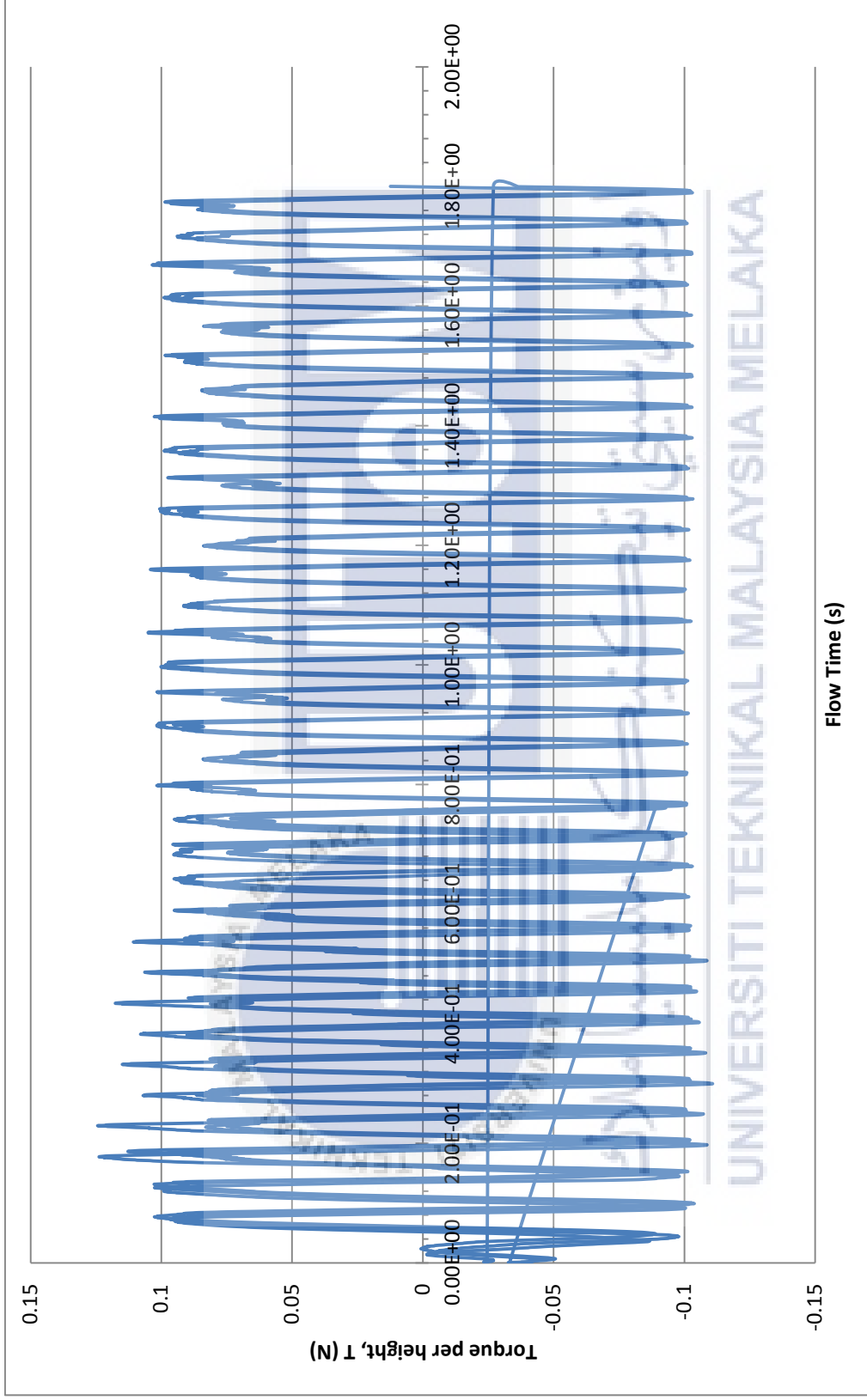


Figure 4.14 Variation of torque of Design 3 rotor with time value for $V = 8.23$ m/s

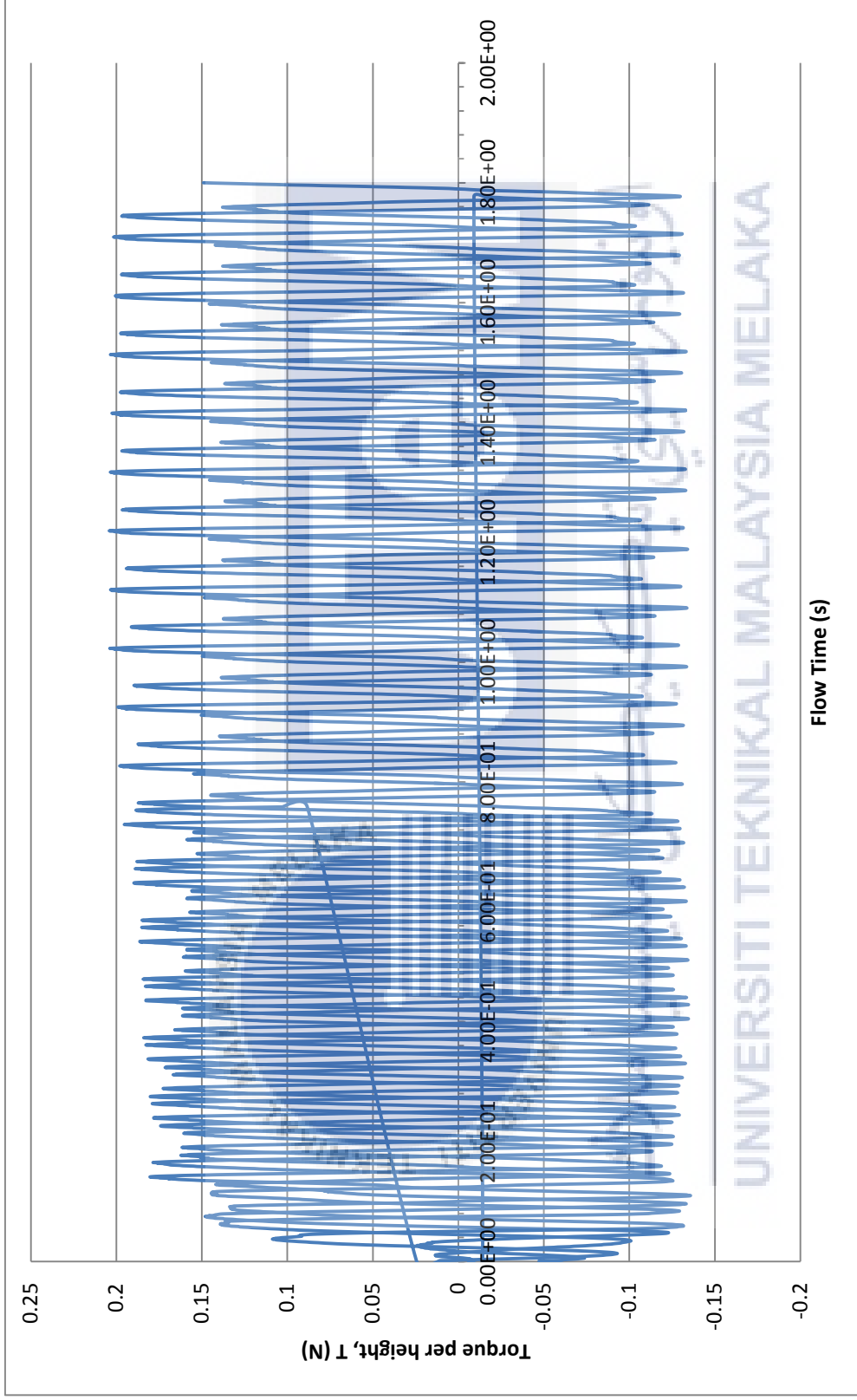


Figure 4.15 Variation of torque of Design 3 rotor with time value for $V = 10.17$ m/s

Figure 4.16 to Figure 4.18 show velocity distribution of all designs for inlet velocity 6.0, 8.23 and 10.17 m/s. Figure 4.19 to Figure 4.21 show pressure distribution of all designs for inlet velocity 6.0, 8.23 and 10.17 m/s of the same positions to velocity distribution.



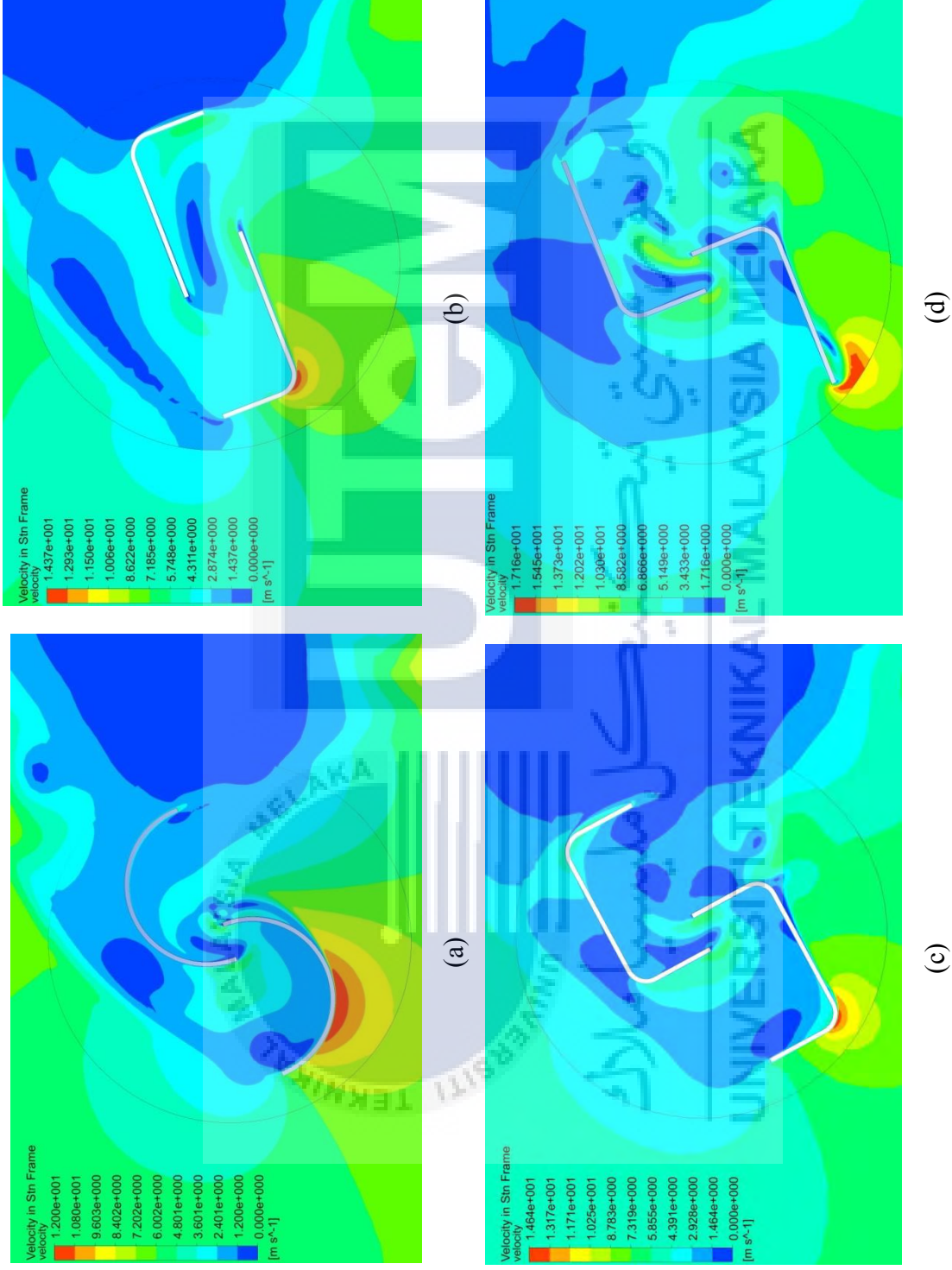


Figure 4.16 Velocity Distribution for $V = 6.0 \text{ m/s}$ (a) Conventional (b) Design 1 (c) Design 2 (d) Design 3

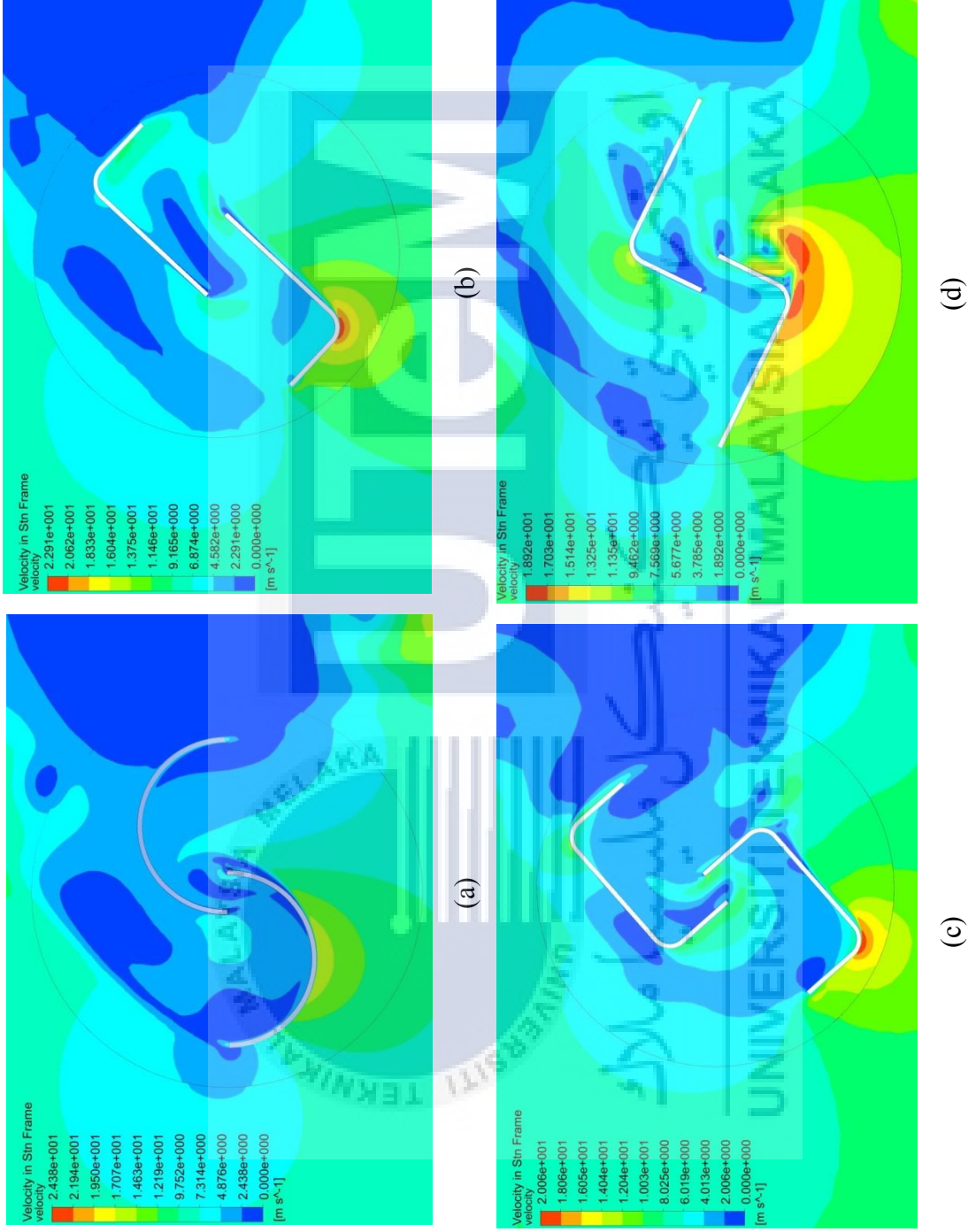


Figure 4.17 Velocity Distribution for $V = 8.23$ m/s (a) Conventional (b) Design 1 (c) Design 2 (d) Design 3

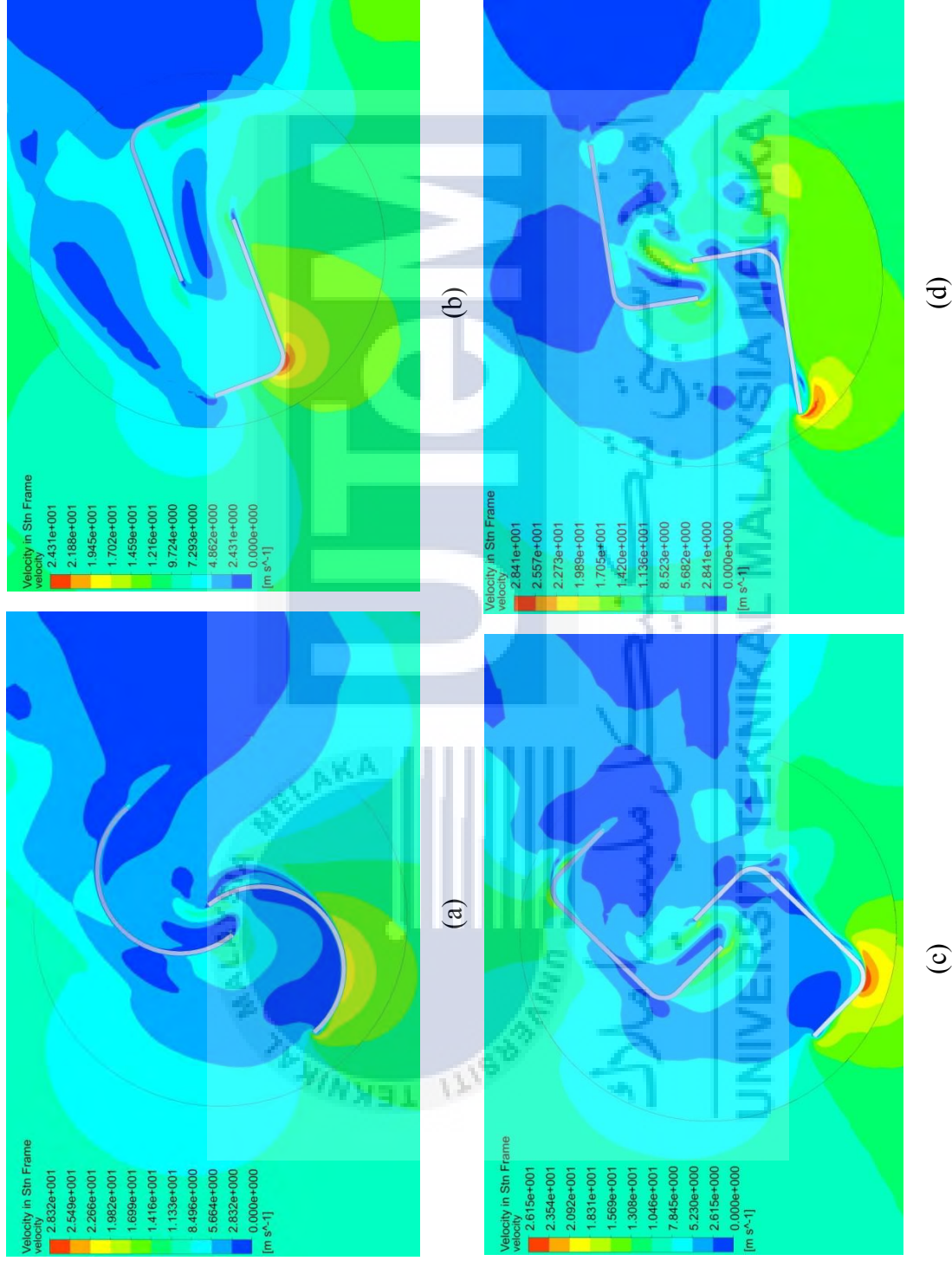


Figure 4.18 Velocity Distribution for $V = 10.17 \text{ m/s}$ (a) Conventional (b) Design 1 (c) Design 2 (d) Design 3

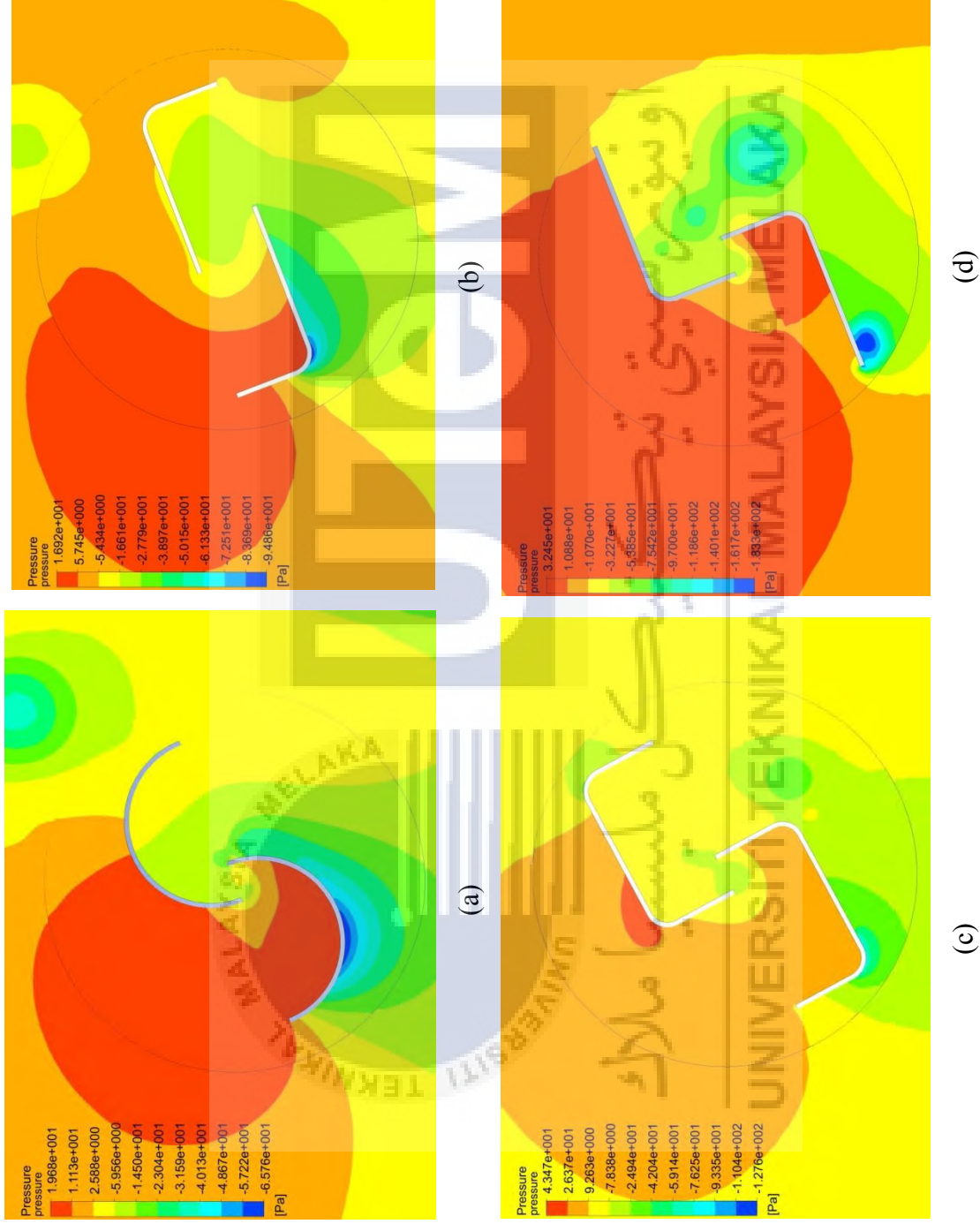


Figure 4.19 Pressure Distribution for $V = 6.0$ m/s (a) Conventional (b) Design 1 (c) Design 2 (d) Design 3

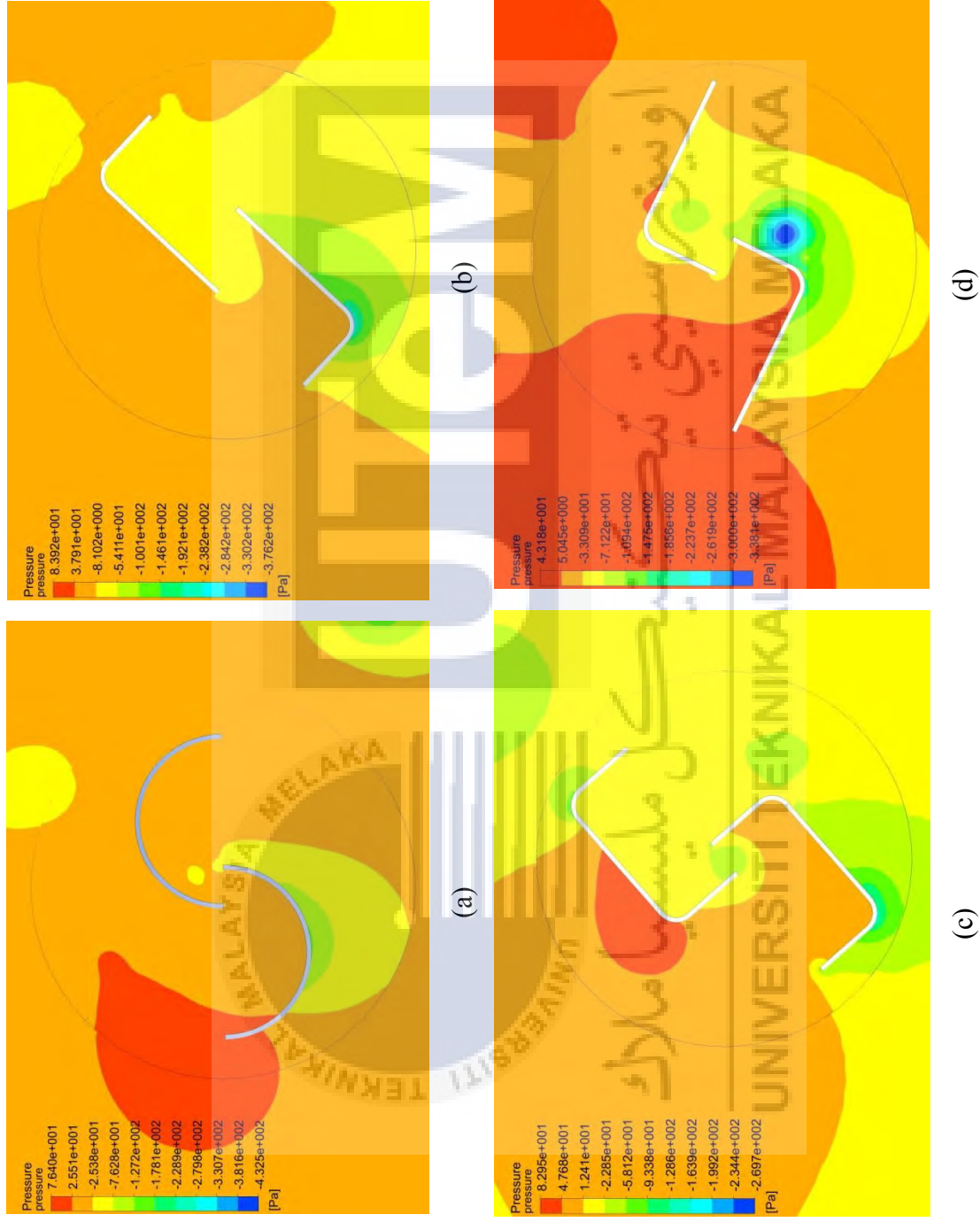


Figure 4.20 Pressure Distribution for $V = 8.23 \text{ m/s}$ (a) Conventional (b) Design 1 (c) Design 2 (d) Design 3

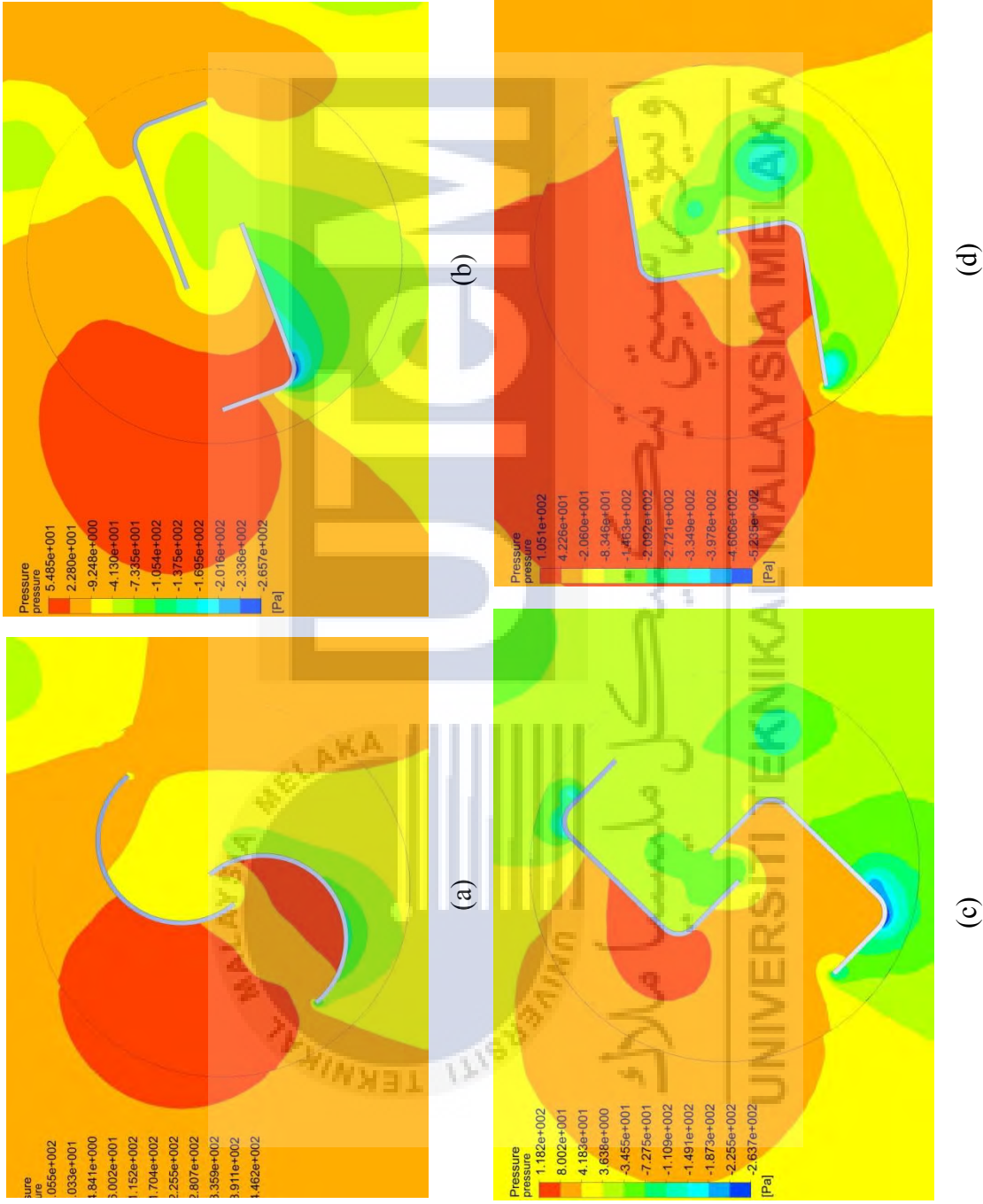


Figure 4.21 Pressure Distribution for $V = 10.17$ m/s (a) Conventional (b) Design 1 (c) Design 2 (d) Design 3

Velocity distributions in Figures 4.16(a), 4.17(a), and 4.18(a) show that conventional rotor regardless its inlet velocity developed maximum velocity behind returning blade especially when the returning blade is near velocity inlet for each inlet velocity. Maximum velocity increases as inlet velocity increases. Rotating motion of the rotor initiates alike motion in surrounding fluid which causes kinetic energy of the working fluid to act on both advancing and returning blades. However, high velocity behind the returning blade causes the area to have lower pressure as shown in pressure distribution of conventional rotor in Figure 4.19(a), 4.20(a), and 4.21(a). This phenomenon complies with Bernoulli's Principle which causes less resistance acting on the rotational motion of advancing blade.

Velocity distributions in Figures 4.16(b), 4.17(b), and 4.18(b) show that Design 1 rotor has similar pattern to conventional rotor. Maximum velocity for each inlet velocity is obtained behind returning blade and it gets higher as inlet velocity increases. Velocity distribution for Design 1 rotor shows that maximum velocity for this rotor occurred in smaller area compared to conventional rotor, thus, less low pressure area to help increase rotational motion of advancing blade as shown in Figure 4.19(b), 4.20(b), and 4.21(b). However, it is clear that Design 1 rotor receives higher velocity on advancing and returning blades' concave sides compared to conventional rotor. The exposed area of blades that received higher velocity is also larger due to its L-shape. These factors resulting in higher net positive torque generated by Design 1 rotor compared to conventional rotor.

Velocity distribution Figures 4.16(c), 4.17(c), and 4.18(c) show that Design 2 has similar pattern to conventional rotor where maximum velocity is developed behind returning blade regardless its inlet velocity. Generally, Design 2 rotor experienced lower velocity compared to conventional rotor at the same condition. It is observed that, Design 2 rotor has a larger exposed area towards kinetic energy of working fluid compared to conventional rotor due to its U shape. However, velocity acting on concave side of advancing and returning blades is considered low compared to conventional and Design 1 rotor. High velocity flow passed through the overlap without generating force against advancing blade. Therefore, the rotational motion of advancing blade is not as high as conventional and Design 1 rotors even low pressure area exists behind returning blade as shown in Figure 4.19(c), 4.20(c), and 4.2 (c) resulting in low net positive torque.

Velocity distribution in Figures 4.16(d), 4.17(d), and 4.18(d) for Design 3 rotor show that high velocity builds up along convex side of returning blade with the highest point near the tip or curve depending on rotor position against velocity inlet. High velocity causes the area to have lower pressure as shown in Figure 4.19(d), 4.20(d), and 4.21(d) which is useful to increase force acting on advancing blade. However, the rotational motion of this high velocity fluid does not end at advancing blade but near the overlap instead resulting in low force generated on advancing rotor which contributes to low net positive torque. Design 3 rotor has higher exposed area compared to conventional rotor but it is not capable of generating higher torque due to rapid deflection of high velocity rotating fluid towards returning blade.



CHAPTER 5

SUMMARY

A two dimensional numerical study to simulate the effect of rotor designs on performance is conducted by developing and validating methodology with experimental study by Saha et al. Three new configurations are created by using ANSYS DesignModeler. End plate diameter, overlap and aspect ratio are kept constant for all designs based on conventional rotor dimensions. Triangular meshing is created by using ANSYS Meshing to allow easier meshing of complex shape and prism mesh layers are formed around each blade to accurately obtain torque near blades' wall. ANSYS Fluent is used to perform 2D transient simulation by using SST turbulence model. Validation study achieved considerable percentage difference ranging from 35.19% to 102.96% between torque obtained from numerical approach and torque obtained from experimental approach performed by Saha et al. Comparative study between conventional rotor and three new configurations show positive improvement is achieved for Design 1 with increase in performance ranging from 0.78% to 1.33% for different inlet velocities. However, Design 2 and Design 3 show negative improvement compared to conventional rotor. L-shaped rotor developed higher force acting on advancing blade's wall by increasing fluid velocity against the wall. Low pressure on convex side of returning blade due to high fluid velocity reduces net negative torque acting on the returning blade. Present study proved that L-shaped rotor is able to generate higher net positive torque compared to conventional S-shaped rotor. Thus, it is proven to be more effective. In future, variation of other parameters based on L-shaped rotor can be analysed and compared to obtain optimized Split Savonius rotor. Performance improvement is achievable without increasing space requirement and complex modification.

REFERENCES

- (2010). In J. M. Yunus A. Cengel, *Fluid Mechanics: Fundamentals and Applications* (pp. 822-838). Singapore: McGraw Hill Higher Education.
- A. Reza Hassanzadeh, O. Y. (2013). Comparison of Conventional and Helical Savonius Marine Current Turbine Using Computational Fluid Dynamics. *World Applied Sciences Journal*, 8(28), 1113-1119.
- Abdul Qadir Versiani, S. C. (2015). Energy Optimization of Savonius Vertical Axis Wind Turbine. *Journal of Electronic Science and Technology*, 13(4), 379-383.
- Abdullah Al-Faruk, A. S. (2016). Geometrical Optimization of A Swirling Savonius Wind Turbine Using An Open Jet Wind Tunnel. *Alexandria Engineering Journal*(55), 2055-2064.
- Ali, M. H. (2013). Experimental Comparison Study for Savonius Wind Turbine of Two and Three Blades at Low Wind Speed. *International Journal of Modern Engineering Research*, 3(5), 2978-2986.
- B Wahyudi, S. S. (2013). A Simulation Study of Flow and Pressure Distribution Patterns in and around Tandem Blade rotor of Savonius (TBS) Hydrokinetic Turbine Model. *Journal of Clean Energy Technologies*, 1(4), 286-291.
- B. D. Altan, M. A. (2008). An Experimental Study on Improvement of A Savonius Rotor Performance with Curtaining. *Experimental Thermal and Fluid Sciences*(32), 1673-1678.
- Bagus Wahyudi, Sudjito Soeparmanb, H W M Hoeijmakersc. (2014). Optimization Design Of Savonius Diffuser Blade With Moving. *2nd International Conference on Sustainable Energy Engineering and Application, ICSEEA 2014*, 10.
- Barnard, M. (2014, April 7). *Cleantechnica*. Retrieved from Vertical Axis Wind Turbines: Great in 1890, Also Run in 2014: <http://cleantechnica.com/2014/04/07/vertical-axis-wind-turbines-great-1890-also-rans-2014/>
- Chung, T. (2002). *Computational Fluid Dynamics*. Cambridge: Cambridge University Press.

- Energy and Environment*. (2016, October 10). Retrieved from eniscuola.net:
http://www.eniscuola.net/wp-content/uploads/2013/11/migrazione/assets/6783/pdf_wind.pdf
- Frederikus Wenehenubuna, Andy Saputraa, Hadi Sutanto. (2014). An Experimental Study On The Performance Of Savonius Wind. *2nd International Conference on Sustainable Energy Engineering and Application, ICSEEA 2014*, 8.
- Global Wind Energy Council. (2016, October 11). *Global Status Overview: Wind Power Leads All New Power Generation, Big Markets Dominate in 2015*. Retrieved from Global Wind Energy Council: <http://www.gwec.net/global-figures/wind-energy-global-status/#>
- J., S. (2007). Prediction of The Power Ratio and Torque in Wind Turbine Savonius Rotors Using Artificial Neural Networks. *International Journal of Energy*, 1(2), 33-50.
- John Patrick Abraham, B. P. (2012). Summary of Savonius Wind Turbine Development and Future Application for Small-scale Power Generation. *Journal of Renewable and Sustainable Energy*(4), 4042703/1-4042703/21.
- Lawrence, S. R. (2016). Wind Energy. Boulder, Colorado, United States of America: Leeds School of Business, University of Colorado.
- McAdam, R. (2016). *Tidal Turbines*. Retrieved from Society of Oxford University Engineers (SOUE) News:
<http://www.soue.org.uk/souenews/issue7/tidalturbines.html>
- N.H. Mahmoud a, A.A. El-Haroun, E. Wahba a, M.H. Nasef. (2010). An Experimental Study On Improvement Of Savonius. *Alexandria Engineering Journal*, 7.
- Ozen Engineering. (2014, November 13). *Ozeninc*. Retrieved October 23, 2016, from www.ozeninc.com
- REUK.co.uk. (n.d.). *REUK.co.uk*. Retrieved from The Renewable Energy Website:
<http://www.reuk.co.uk/wordpress/wind/savonius-wind-turbines/>
- Sonu Sharma, R. K. (2016). Performance Improvement of Savonius Rotor Using Multiple Quarter Blades - A CFD Investigation. *Energy Conversion and Management*(127), 43-54.
- Sopian, P. D. (2016, October 11). Marine Energy and Wind Energy Conversion System. *Solar Energy Reseach Institute*. Malaysia: Universiti Kebangsaan Malaysia. Retrieved from Solar Energy Research Institute Universiti Kebangsaan Malaysia.

- Sukanta Roy, U. K. (2013). Computational Study to Assess The Influence of Overlap Ratio on Static Torque Characteristics of A Vertical Axis Wind Turbine. *Procedia Engineering*(51), 694-702.
- U.K Saha, S. T. (2008). Optimum Design Configuration of Savonius Rotor Through Wind Tunnel Experiments. *Journal of Wind Engineering and Industrial Aerodynamics*(96), 1359-1375.
- Vertical Axis Wind Turbines vs Horizontal Axis Wind Turbines*. (2009, November 10). Retrieved from Windpower: Engineering & Development: <http://www.windpowerengineering.com/construction/vertical-axis-wind-turbines-vs-horizontal-axis-wind-turbines/>
- Wenlong Tian, B. S. (2015). Computational Fluid Dynamics Prediction of a Modified Savonius Wind Turbine with Novel Blade Shapes. *Energies*, 14.
- Wind Energy Foundation. (2016, October 11). *History of Wind Energy*. Retrieved from Wind Energy Foundation: <http://windenergyfoundation.org/about-wind-energy/history/>

